# TOPOLOGICAL EXCITATIONS AND DISSIPATION IN SUPERCONDUCTORS AND SUPERFLUIDS HAVING MULTIPLY CONNECTED GEOMETRIES

BY

DAVID PEKKER

B.A., Rice University, 2002
B.S., Rice University, 2002

DISSERTATION

Submitted in partial fulfillment of the requirements
for the degree of Doctor of Philosophy in Physics
in the Graduate College of the
University of Illinois at Urbana-Champaign, 2007

Urbana, Illinois

# Abstract

Due to fluctuations, either thermal or quantum, the superflow through a sufficiently narrow channel will experience dissipation. The dissipation occurs via discrete topological excitations, called phase-slips, in which vortex lines cross the superconducting or superfluid channel. The interaction between these excitations in multiply connected geometries are studied in various settings. Rich consequences are found to occur, including the sensitivity of phase-slips to the supercurrent in the bulk superfluids connected to the thin channels, as well as avalanches of phase-slips.

*To my parents.*

# Acknowledgments

This thesis research is a product of collaboration with many people both at UIUC and other institutions. My greatest thanks goes to my adviser and teacher Prof. Paul M. Goldbart, who provided me with a constant stream of challenging, interesting, and important problems, an open atmosphere to work on them, but with sufficient guidance to avoid getting lost, and also thorough financial support. I feel that the guidance I have received from Prof. Goldbart really let me develop and grow intellectually. Within our group I have always felt a good balance between feeling challenged but also protected.

I would also like to acknowledge my former teachers who guided me through undergraduate research: Prof. Isaac Bersuker from The University of Texas at Austin and Prof. James F. Annett from The University of Bristol, UK. Prof. Bersuker was my first physics teacher; in his group I first encountered serious physics problems and learned about the ubiquitous concept of spontaneously symmetry breaking. Prof. Annett taught me about symmetry and superconductivity, the two concepts that form the basis of this thesis.

Special thanks goes to Prof. Alexey Bezryadin at the University of Illinois and his graduate students David S. Hopkins and Mitrabhanu Sahu and former postdoctoral researcher Prof. Andrey Rogachev, for collaborating so closely with us, for sharing their wonderful experiments on superconducting nanowires, patiently explaining their data, and listening to our suggestions. In addition I would like to acknowledge Prof. Richard Packard from University of California Berkeley and his graduate students Yuki Sato and Aditya Joshi for introducing us to the field of superfluidity and patiently explaining their beautiful experiments.

I would like to thank my group members, Swagatam Mukhopadhyay, Tzu-Chieh Wei, and Florin Bora together with Bryan Clark, Roman Barankov, Nayana Shah, Prof. Nandini Trivedi and Prof. Karin Dahmen for the wonderful camaraderie, collaboration, and interest in discussing physics at any time of the day and night. Many other people have contributed to my wonderful experience in graduate school, I would like to acknowledge Prof. Smitha Vishveshwara, Dr. Michael Hermele, Prof. Gil Refael, Prof. Michael Stone, and Prof. Phillip Phillips for teaching me so much, for sharing their ideas and the many inspiring discussions.

During my graduate career, here, at the University of Illinois at Urbana-Champaign, I have been supported in part by the Roy J. Carver fellowship and by the U.S. Department of Energy, Division of Material

Science under Award No. DEFG02-96ER45434, through the Fredrick Seitz Materials Research Laboratory at the University of Illinois at Urbana-Champaign. I also acknowledge the receipt of a Mavis Memorial Fund Scholarship (2005) and the John Bardeen Award for graduate research (2007).

I would like to thank my parents, my grandparents, sister, and my uncle for providing constant support, believing in me, and helping with some integrals and differential equations. My sister, Ira, also suggested the shading scheme in Fig. 1.3. Finally, I would like to thank my fiancée, Dr. Preeti Kaur, for inspiring me to work hard and to reach, successfully, beyond my abilities.

# Table of Contents

# List of Tables

# List of Figures

# List of Abbreviations

| | |
|---|---|
| GL | V. L. Ginzburg and L. D. Landau [1] |
| BCS | J. Bardeen, L. Cooper, R. Schriffer [2] |
| MQC | Macroscopic Quantum Coherence |
| ODLRO | Off Diagonal Long Range Order |
| IZ-AH | Y. M. Ivanchenko, L. A. Zil'berman [3, 4], V. Ambegaokar, and B. I. Halperin [5] |
| LAMH | J. S. Langer, V. Ambegaokar [6], D .E. McCumber, and B. I. Halperin [7] |
| CDW | Charge Density Wave |
| RFIM | Random Field Ising Model |
| SWA | System-Wide Avalanche |
| MSR | P. C. Martin, E. D. Siggia, and H. A. Rose [88] |

# Chapter 1

# Introduction to phase-slip processes

In 1911 in the laboratory of Heike Kamerlingh Onnes it was discovered that when mercury is cooled to a temperature below approximately 4.2 K its resistivity abruptly vanishes. The drop in the resistivity is associated with a discontinuity in the heat capacity, indicating the formation of a new state of matter – the superconducting state. In 1933 Walther Meissner and Robert Ochsenfeld [8] discovered that, in addition to losing electrical resistance, superconductors are also perfect diamagnets in that they completely expel magnetic fields, a property that has become known as the Meissner effect.

The first phenomenological model of superconductivity was proposed by Fritz and Heinz London [9]. They postulated that within a superconductor there are two types of electrons: normal and superconducting. The DC electrical properties would be determined by the superconducting electrons, which would have zero electrical resistance and also the following constitutive property:

$$\boldsymbol{A} = -\frac{4\pi}{c}\lambda^2 \boldsymbol{j}, \tag{1.1}$$

where $\boldsymbol{A}$ is the electromagnetic vector potential, $\boldsymbol{j}$ is the charge current density, and $\lambda \equiv \sqrt{m^* c^2/4\pi n_s e^2}$ sets the scale for the magnetic field penetration depth ($m^*$ is the mass of the carrier and $n_s$ is the number density of the superconducting carriers). Equation 1.1 relies on a special choice of gauge, called the London gauge, in which $\boldsymbol{A}$ at the edges of the superconducting sample is parallel to those edges. Further, Eq. 1.1, arises as the result of choosing a zero value for the integration constant in Newton's equation of motion for the electron, which corresponds to the absence of a magnetic field deep within the superconductor. An important consequence of this property is the perfect expulsion of magnetic fields from bulk superconductors, i.e. perfect diamagnetism.

In 1950 Vitaly Lazarevich Ginzburg and Lev Davidovich Landau (GL) proposed a more refined phenomenological model of superconductivity that better captured the quantum nature of the superconducting state [1]. Their model is a model of spontaneous symmetry breaking that occurs at the superconducting phase transition. The superconducting state is described by a complex scalar field $\psi$ that acquires a nonzero expectation value below the transition temperature $T_c$. The amplitude $|\psi|^2$ corresponds to the density of the superconducting carriers $n_s$. Later, Lev P. Gor'kov showed that $\psi$ corresponds to the wavefunction of the center-of-mass coordinate of the Cooper pairs in the superconducting condensate [10, 11]. The Ginzburg-Landau free energy functional is

$$F[\psi] = \int d^3r\, \alpha|\psi|^2 + \frac{\beta}{2}|\psi|^4 + \frac{\hbar^2}{2m}|\nabla\psi - i\frac{e^*}{\hbar c}A|^2 + \frac{H^2}{8\pi}, \tag{1.2}$$

where the first term is strongly temperature dependent near the superconducting transition, $\alpha \propto (T - T_c)$, changing sign as the temperature goes through $T_c$, resulting in the emergence of the superconducting condensate as the equilibrium state.

The microscopic character of the for superconducting state was discovered by John Bardeen, Leon Cooper, and Robert Schriffer (BCS) [2]. They showed that even a very small attractive potential between electrons can lead to the formation of a condensate of pairs. Following the discovery of the isotope effect [12, 13] (also independently suggested by Fröhlich [14]) BCS argued that the origin of this force (in classical superconductors) lies in the interaction between electrons and lattice deformations (phonons). Having identified the charge carrier in a superconductor as a pair of electrons, the phenomenological description of Ginzburg and Landau becomes transparent. As the charge carriers are not electrons, but pairs of electrons, it is clear from the BCS picture that $e^* = 2e$ and $m^* = 2m$. In fact, Gor'kov has shown that the GL theory is the low-energy description of the BCS theory [10, 11].

Closely related to the story of superconductivity is the story of superfluidity, which was playing out at roughly the same time. Before 1934, Kamerlingh Onnes' Laboratory in Lyden enjoyed a near monopoly on cryogenic research. There, it was discovered that in the vicinity of 2.17 K, the specific heat capacity of $^4$He liquid as a function of temperature diverged in the shape of the Greek letter $\lambda$. In 1934, Peter Leonidovich Kapitza was setting up the Mond Laboratory in Cambridge to study the properties of materials at low temperatures and high magnetic fields. In order to achieve the low temperatures required, he invented a new and highly efficient apparatus for the liquefaction of helium. This invention allowed for research involving large amounts of helium, which eventually made possible the discovery of superfluidity. However, in the same year Kapitza was detained in the USSR and forbidden from returning to his post in the UK. By 1937 it was known that the physical properties of liquid $^4$He became very unusual below 2.17 K, so much so that the liquid was named He-II, to distinguish it from the form of helium that exists above 2.17 K called He-I. In particular the thermal conductivity of He-II was found to be 10000 times large than that of He-I [15, 16, 17]. By 1938 Kapitza [18] working at the Institute for Physical Problems in Moscow and independently John

F. Allen and A. D. Misener [19] working at the Mond Laboratory in Cambridge discovered a most striking phenomenon: the new "form" of Helium seemed to have vanishingly small viscosity, and was thus able to flow through capillaries without resistance (or to leak out of a container that had the tiniest hole), a phenomenon that Kapitza called superfluidity. The investigation of the anomalously high thermal conductivity of He-II led to the discovery of the fountain effect [20]. The lack of viscosity in He-II was associated with the lack of resistance in superconductors, and thus was named superfluidity [21].

According to Pitaevskii, one of the first practical application of superfluidity arose in 1938, when Landau was arrested "as a result of an outrageous and false (but typical for those days) accusations of espionage and sabotage" [22]. Peter Kapitza, who at the time was the head of the Institute for Physical Problems in Moscow, used superfluidity as an excuse in his fight to save Landau. A year before Landau's arrest, Kapitza had arranged for Landau to move to Moscow, which undoubtedly delayed the arrest. On the day of the arrest, Kapitza wrote a letter to J. V. Stalin, the Secretary General of the Communist Party, on Landau's behalf. However, neither Kapitza's letter nor one from Niels Bohr had the desired effect. Next, Kapitza wrote a letter to V. M. Molotov, the second highest political figure after Stalin, demanding that he needed a good theorist like Landau to help him write a paper on the properties of superfluid Helium. This approach worked and Landau was released.

To explain the superfluid effect, Landau suggested the following phenomenological criterion [23]: excitations in a fluid may be generated only when the phase velocity of the excitation exceeds the flow velocity of the fluid. Therefore, Landau defined the critical velocity, $v_c$, as the phase velocity of the slowest excitation:

$$v_c = \min \frac{\epsilon(p)}{p}, \tag{1.3}$$

where $p$ is the momentum and $\epsilon(p)$ the energy of the excitation. If $v_c$ is nonzero then the fluid is a superfluid and exhibits dissipationless flow at velocities smaller than $v_c$. If $v_c$ is exceeded then elementary excitations start to be created by the flow, resulting in viscous drag on the fluid. Landau further developed the theory of two-fluid (quasi-)hydrodynamics describing the quantum superfluid component and the normal component and their interactions.

A useful description of superfluidity, which will be the basis for further calculations within this thesis, was proposed independently by Gross [24, 25] and Pitaevskii [26]. Consider the many-body Heisenberg equation of motion for the field operator $\Psi(r,t) = \sum_\alpha \psi_\alpha(r,t)a_\alpha$, where the $a_\alpha$'s are the annihilation operators for the single-particle wave functions $\psi_\alpha(r)$. This equation of motion reads

$$i\hbar\frac{\partial}{\partial t}\Psi(r,t) = [\Psi, H] \tag{1.4}$$

$$= \left[-\frac{\hbar^2\nabla_r^2}{2m} + V_{\text{ext}}(r) + \int dr'\, |\Psi(r',t)|^2 V(r-r')\right]\Psi(r,t), \tag{1.5}$$

where $V_{\text{ext}}(r)$ is the external or confining potential and $V(r-r')$ is the two-particle interaction potential. Replacing the field operator $\Psi$ by its expectation value $\Phi(r,t) = \langle\Psi(r,t)\rangle$ we obtain the mean-field equation known as the Gross-Pitaevskii equation:

$$i\hbar\frac{\partial}{\partial t}\Phi(r,t) = \left[-\frac{\hbar^2\nabla^2}{2m} + V_{\text{ext}}(r) + g|\Phi(r,t)|^2\right]\Phi(r,t), \tag{1.6}$$

where we have also replaced the two-particle potential by the point contact interaction $V(r'-r) = g\delta(r'-r)$. Here, $\Phi$ plays the role of an order parameter. Strictly speaking, the Gross-Pitaevskii description is only correct at zero temperature, when there are no excitations present, and even then it neglects correlation effects. In this thesis we concentrate only on the properties of the analogous static equation, where the left-hand-side is set to zero.

## 1.1 Phase coherence and topological excitations

The key feature of both superfluids and superconductors is their so-called macroscopic quantum coherence (MQC), which is a direct consequence of their off diagonal long range order (ODLRO). MQC implies that the amplitude and the phase of the order parameter $\psi(r)$ (i.e. the wavefunction of superfluid atoms for the case of superfluids, or the center-of-mass of the Cooper pairs for the case of superconductors) are both sufficiently stiff that the two-point correlator is always nonzero:

$$\langle\psi^\dagger(r)\psi(0)\rangle \neq 0, \tag{1.7}$$

and approaches some finite value $n_{\text{s}}$ as $r \to \infty$ called the condensate fraction [1]. Therefore, it is reasonable to ask how the order parameter changes as one follows a closed-loop? Assuming that we choose a loop where the amplitude of the order parameter is always non-zero, the single valuedness of the order parameter

---

[1] In two dimensions, for $T < T_{KTB}$, this correlator falls off algebraically with separation, resulting in superfluidity with no long range order.

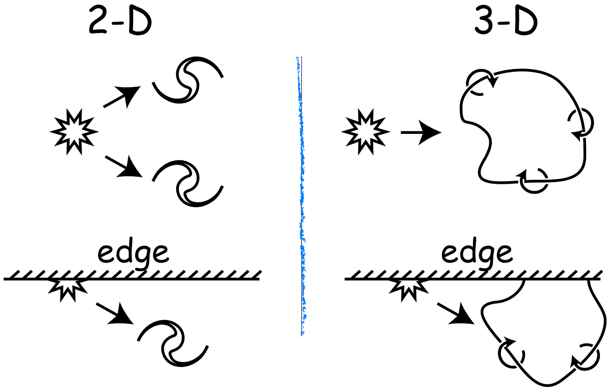

Figure 1.1: Schematic depiction of the formation of vortex pairs and vortex loops. The stars depict the fluctuation from which the vortices are born. Top row: formation of vortex pairs (left) and a vortex loop (right) in bulk superfluid. Bottom row: formation of a single vortex (left) and a vortex half-loop (right) at a superfluid edge.

implies that the phase gain around the loop is a multiple of $2\pi$:

$$\oint \nabla\phi \cdot dl = 2\pi n, \qquad\qquad n \in \mathbb{Z}. \tag{1.8}$$

In other words, as the order parameter is a complex scalar, the first homotopy group of the mapping between the space of nonzero order parameters and closed loops is $\mathbb{Z}$. Therefore, each closed loop encircles an integer number of quantized vortices that pass through it. Furthermore, in order to change the number of vortices within such a closed loop, somewhere along the loop the order-parameter must temporarily become zero.

These arguments imply that in two spatial dimensions, within the bulk superfluid or superconductor, vortices must be born in pairs with partners of opposite vorticity, which may later separate. For the case of three dimensions vortices must be born as vortex line that closes on itself, which may later expand in space. A vortex line is a line along which the amplitude of the order parameter is zero, and if we integrate the phase gain along a contour that winds around the vortex line exactly once the result is a multiple of $2\pi$ associated with the vorticity of the vortex line. The formation of vortex-anti-vortex pairs and closed vortex lines is illustrated in the top row of Fig. 1.1. The situation is different if the superfluid has a boundary. In two dimensions isolated vortices may be born directly on a boundary, while in three or more dimensions vortex lines in the shape of half-loops may spontaneously emerge, the vortex line being anchored to the boundary at both ends of the half-loop. The formation of isolated vortices and vortex half-loops is illustrated in the bottom row of Fig. 1.1.

Before proceeding to describe phase-slips, we make some remarks regarding the structure of vortices and vortex-lines. Within the context of this thesis, we shall confine ourselves to the structure and properties of vortices as obtained from the GL equation. We assume that the temperature is sufficiently below the transition temperature that order parameter fluctuations may be ignored. For the case of neutral superfluids, $\xi$ is the only length-scale, and it determines the size of the vortex core, i.e. the size of the region where the order parameter amplitude is suppressed. For the case of superconductors, there are two lengths-scales, $\xi$ and $\lambda$, which determine the vortex structure. If $\lambda < \xi$ then vortices are unstable. On the other hand if $\lambda > \xi$ then vortices are stable. For this case, $\xi$ again determines the size of the core, whereas $\lambda$ determines the size of the region of flux-penetration associated with the vortex.

## 1.2 Thermally activated phase-slips

We shall specialize to geometries having two bulk superfluids or superconductors connected by one or more weak links. The weak links that we shall consider are either small apertures in a thin membrane separating the two bulk superfluids or narrow superconducting bridges or wires connecting two large bulk superconductors.

We shall briefly discuss the properties of a single weak link and then move on to the main focus: devices that have multiple weak links. Consider a single weak-link device with a small current $I$ flowing through the weak link between the two bulks. Assign $\Phi^{\mathrm{L}}$ and $\Phi^{\mathrm{R}}$ to be the phases of the left and right bulk. We would like to describe the dynamics of the phase difference $\Delta\Phi = \Phi^{\mathrm{R}} - \Phi^{\mathrm{L}}$. The weak link is called weak because it allows for so-called phase-slip process. In a phase-slip process the order parameter amplitude is completely suppressed within the weak link, by either a thermal or a quantum fluctuation, and, therefore, $\Delta\Phi$ changes by a multiple of $2\pi$ after the process is complete.

We shall describe the weak links by length $d$, and radius $r_0$. Throughout this thesis, we focus on the case of devices much smaller than $\lambda$, and therefore we ignore the lengthscale associated with $\lambda$. Within this regime we may order the lengthscales in the following four ways:

1. $\xi \gtrsim d, 2r_0$ — The weak link functions as a Josephson junction.
2. $d \gg \xi \gtrsim 2r_0$ — The weak link functions as a one-dimensional superconducting wire.
3. $2r_0 \gg \xi \gtrsim d$ — The weak link functions as a wide Josephson junction.
4. $2r_0, d \gg \xi$ — The weak link functions as a wide wire.

In the first regime the size of the weak link (both $d$ and $r_0$) is smaller than $\xi$, therefore there cannot be any additional degrees of freedom associated with the weak link, except for the phase difference between the two bulk superfluids, $\Delta\Phi$. This situation exactly corresponds to that of a Josephson junction. Here, the GL equation within the weak link is dominated by the gradient term and there is only one stable solution for each value of $\Delta\Phi$. The thermodynamics of a Josephson junction shunted by a capacitor and a resistor

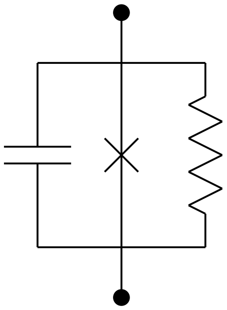

Figure 1.2: Circuit diagram of a resistively and capacitively shunted Josephson junction (represented by the cross).

in the configuration shown in Fig. 1.2 was first studied by Ivanchenko and Zil'berman [3, 4] and also by Ambegaokar and Halperin [5] (IZ-AH). Within the context of this thesis, the weak link acts as both the Josephson junction and the resistor, and there is no external shunt resistor. Within the IZ-AH approach, $\Delta\Phi$ is an extended variable, defined on the whole real line not just on the circle defined by the segment $(0, 2\pi]$. The reason for this is that although the configuration of the order parameter in the vicinity of the weak link returns to its initial state if $\Delta\Phi$ changes by $2\pi$, however, due to the bias current $I$, the battery must have done work on the weak link, so the system as a whole goes to a new state necessitating the use of the extended variable. We can see this by appealing to the Josephson relation $2eV = \hbar\partial_t\Delta\Phi$, which relates potential difference across a Josephson junction to the difference in the rate of the evaluation of the phases of the superconducting order parameters of the leads. The total work done by the battery on the weak link is thus

$$W = \int dt\, IV = \hbar I \Delta\Phi/2e. \tag{1.9}$$

The equation of motion for a shunted Josephson junction may be written as

$$C\partial_t^2\Delta\Phi = \frac{2e}{\hbar}(I - J\sin\Delta\Phi) - \frac{\partial_t\Delta\Phi}{R_N} + \eta(t), \tag{1.10}$$

where $\eta(t)$ is a term that describes thermal noise originating within the shunt resistor $R_N$ (the shunt may be either an external circuit element, or an intrinsic property of the weak link). This noise is assumed to be completely uncorrelated in time, and its strength is determined by the fluctuation dissipation theorem, via

$$\langle\eta(t)\eta(t')\rangle = 2k_BT\delta(t - t')/R_N. \tag{1.11}$$

The equation of motion is the same as that of a particle moving in a “tilted washboard” potential under the influence of random noise. The tilt of the washboard is determined by the strength of the bias current, and the size of the ridges is determined by the Josephson coupling. IZ-AH concentrate on the limit of small capacitance, where the term on the LHS of Eq. (1.10) may be set to zero. In this limit, the rate at which the particle progresses down the washboard can be obtained exactly (see Appendix B). On the other hand, we can also estimate this rate in the regime in which the barriers are much bigger than $k_B T$. Following AH, the sizes of the barriers are:

$$\Delta F_{\pm} = -\frac{\hbar J}{e k_B T}\left[\left(1-\frac{I^2}{J^2}\right)^{1/2} + \frac{I}{J}\sin^{-1}\frac{I}{J} \mp \frac{\pi}{2}\frac{I}{J}\right], \tag{1.12}$$

and the attempt rate corresponds to the rate of relaxation of small perturbations away from the bottom of one of the wells of the tilted washboard potential, $\Omega = 2eJR\left(1-\frac{I^2}{J^2}\right)^{1/2}/\hbar$. Therefore the average (over time) rate at which the phase advances is given by

$$\langle \partial_t \Delta\Phi \rangle = \Omega\left(e^{-\Delta F_{+}/k_B T} - e^{-\Delta F_{-}/k_B T}\right). \tag{1.13}$$

Each thermally-activated barrier crossing process is called a thermally-activated phase slip (TAPS). As an aside, it also makes sense to study the quantum dynamics of this model, which was worked out by Fisher and Zwerger [27], following the ideas of Caldeira and Leggett [28]. Within this thesis we focus on TAPS processes only, however, it would certainly be of interest to work out the case of QPS (quantum phase slip) processes for multiply connected devices.

In the second regime, the weak link is much longer than the coherence length but also narrower. Thus, there are many independent longitudinal degrees of freedom, roughly $d/\xi$, but no transverse ones. This situation corresponds to an effectively one-dimensional superconducting wire (or superfluid capillary). Phase slips in these systems were first discussed by Little [29], who proposed that in the course of a phase slip the amplitude of the order parameter within a region of length $\xi$ fluctuates to zero. When this occurs, the left and right portions of the wire are no longer phase-coherent, so when the fluctuation heals $\Delta\Phi$, as measured by looking at the phase gain going from left to right, can change by a multiple of $2\pi$. The barrier for such a fluctuation can be estimated to be:

$$\Delta F = \xi \pi r_0^2 \frac{H_c^2}{8\pi}, \tag{1.14}$$

where $\xi\pi r_0^2 = \xi\sigma$ corresponds to the volume of the wire in which the order parameter is suppressed ($\sigma$ being

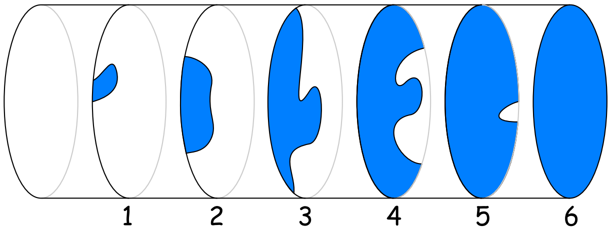

Figure 1.3: Schematic depiction of a half-loop vortex line crossing the aperture. The half-loop is nucleated in slice 1, the end points move around the aperture and rejoin in slice 6. Phase gain going from left to right reservoir differs by $2\pi$ depending on whether the trajectory goes through the blue or white region.

the cross-sectional area) and $H_c^2/8\pi$ is the condensation energy per unit volume. The rate of phase slips follows the Arrhenius law $\Gamma \sim \exp(-\Delta F/k_B T)$. Furthermore, due to the bias current $I$ flowing through the weak link, the barrier for phase slips that add or subtract $2\pi$ phase differences differ. Langer and Ambegaokar (LA) further extended Little's proposal by computing the free energy barrier for the one-dimensional GL model of the wire [6] (see Appendix C). McCumber compared the current- and voltage-biased cases [30]. Finally, McCumber and Halperin computed the pre-exponential factor to find the rate at which phase slips occur [7].

The third regime corresponds to the situation described by Anderson [31]. In this setting, there are many transverse degrees of freedom. Phase slippage occurs by the nucleation of a half-loop line vortex that sweeps across the aperture as indicated in Fig. 1.3. The computation of the barrier to phase-slippage in this regime is much more complicated, and is dependent on the properties of the walls of the aperture.

The fourth regime is similar to the third one, in that phase-slips occur via crossing of half-loop vortex lines. This regime will feature prominently in Chapter 3; however, we shall consider only a simple deterministic model of the superflow through such an aperture, in which a phase slip occurs once the supervelocity exceeds an aperture-dependent critical velocity.

## 1.3 Overview of the dissertation

The main goal of this thesis is to examine properties of the dynamics of multiply-connected superfluid and superconducting systems. The thesis is split into two main parts. In Chapter 2 we concentrate on a system studied experimentally by David S. Hopkins and Alexey Bezryadin. It is composed of two bulk superconductors connected by a parallel pair of superconducting wires. We have developed a detailed model of this system and computed the barriers (and, consequently, rates for phase slips) in the various wires and how these depend on currents and magnetic fields applied to the bulk superconductors. In Chapter 3, we describe our work inspired by the experiments of Yuki Sato, Aditya Joshi, and Richard Packard on the superflow of helium through an array of nanosized apertures in a thin membrane. We find that, due to the coupling between the superflows in the various apertures, this system can display a wide variety of dynamic processes.

# Chapter 2

# Superconducting two-nanowire devices

In this Chapter a theory describing the operation of a superconducting nanowire quantum interference device (NQUID) is presented. The device consists of a pair of thin-film superconducting leads connected by a pair of topologically parallel ultra-narrow superconducting wires. It exhibits intrinsic electrical resistance, due to thermally-activated dissipative fluctuations of the superconducting order parameter. Attention is given to the dependence of this resistance on the strength of an externally applied magnetic field aligned perpendicular to the leads, for lead dimensions such that there is essentially complete and uniform penetration of the leads by the magnetic field. This regime, in which at least one of the lead dimensions—length or width—lies between the superconducting coherence and penetration lengths, is referred to as the *mesoscopic* regime. The magnetic field causes a pronounced oscillation of the device resistance, with a period *not* dominated by the Aharonov-Bohm effect through the area enclosed by the wires and the film edges but, rather, in terms of the geometry of the leads, in contrast to the well-known Little-Parks resistance of thin-walled superconducting cylinders. A detailed theory, encompassing this phenomenology quantitatively, is developed through extensions, to the setting of parallel superconducting wires, of the Ivanchenko-Zil'berman-Ambegaokar-Halperin theory of intrinsic resistive fluctuations in a current-biased Josephson junctions and the Langer-Ambegaokar-McCumber-Halperin theory of intrinsic resistive fluctuations in superconducting wires. In particular, it is demonstrated that via the resistance of the NQUID, the wires act as a probe of spatial variations in the superconducting order parameter along the perimeter of each lead: in essence, a superconducting phase gradiometer.

This work was done in collaboration with D. S. Hopkins, A. Bezryadin, and P. M. Goldbart.

## 2.1 Introduction

The Little-Parks effect concerns the electrical resistance of a thin cylindrically-shaped superconducting film and, specifically, the dependence of this resistance on the magnetic flux threading the cylinder [32, 33, 34]. It is found that the resistance is a periodic function of the magnetic field, with period inversely proportional to the cross-sectional area of the cylinder. Similarly, in a DC SQUID, the critical value of the supercurrent is periodic in magnetic field, with period inversely proportional to the area enclosed by the SQUID ring [34].

In this Chapter, we consider a mesoscopic analog of a DC SQUID. The analog consists of a device composed of a thin superconducting film patterned into two mesoscopic leads that are connected by a pair of (topologically) parallel, short, weak, superconducting wires. Thus, we refer to the device as an NQUID (superconducting nanowire quantum interference device). The only restriction that we place on the wires of the device is that they be thin enough for the order parameter to be taken as constant over each cross-section of a wire, varying only along the wire length. In principle, this condition of one-dimensionality is satisfied if the wire is much thinner than the superconducting coherence length $\xi$. In practice, it is approximately satisfied provided the wire diameter $d$ is smaller than $4.4\,\xi$ [35]. For thicker wires, vortices can exist inside the wires, and such wires may not be assumed to be one dimensional.

By the term *mesoscopic* we are characterizing phenomena that occur on length-scales larger than the superconducting coherence length $\xi$ but smaller than the electromagnetic penetration depth $\lambda_\perp$ associated with magnetic fields applied perpendicular to the superconducting film. We shall call a lead mesoscopic if at least one of its two long dimensions is in the mesoscopic regime; the other dimension may be either mesoscopic or macroscopic. Thus, a weak magnetic field applied perpendicular to a mesoscopic lead will penetrate the lead without appreciable attenuation and without driving the lead from the homogeneous superconducting state to the Abrikosov vortex state. This is similar to the regime of operation of superconducting wire networks; see e.g., Ref. [36, 37]. The nanowires connecting the two leads are taken to be topologically parallel (i.e. parallel in the sense of electrical circuitry): these nanowires and edges of the leads define a closed geometrical contour, which will be referred to as the *Aharonov-Bohm (AB) contour*. In our approach, the nanowires are considered to be links sufficiently weak that any effects of the nanowires on the superconductivity in the leads can be safely ignored.

The theory presented here has been developed to explain experiments conducted on DNA-templated NQUIDs [38]. These experiments measure the electrical resistivity of a pair of superconducting nanowires suspended between long superconducting strips (see Fig. 2.1). In them, a current source is used to pass DC current from a contact on the far end of the left lead to one on the far end of the right lead. The voltage between the contacts is measured (and the resistance is hence determined) as a function of the magnetic field applied perpendicular to the plane of the strips.

In the light of the foregoing remarks, the multiple-connectedness of the device suggests that one should anticipate oscillations with magnetic field, e.g., in the device resistance. Oscillations are indeed observed. But they are distinct from the resistance oscillations observed by Little and Parks and from the critical

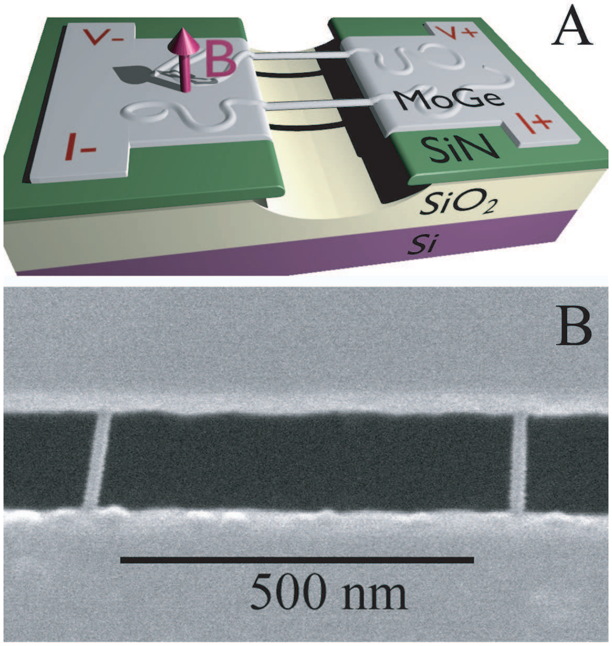

Figure 2.1: (A) Schematic depiction of the superconducting phase gradiometer. A current $I$ is passed through the bridges in the presence of a perpendicular magnetic field of strength $B$ and the voltage $V$ is measured. (B) SEM micrograph of two metal coated DNA molecules, sample 219-4.

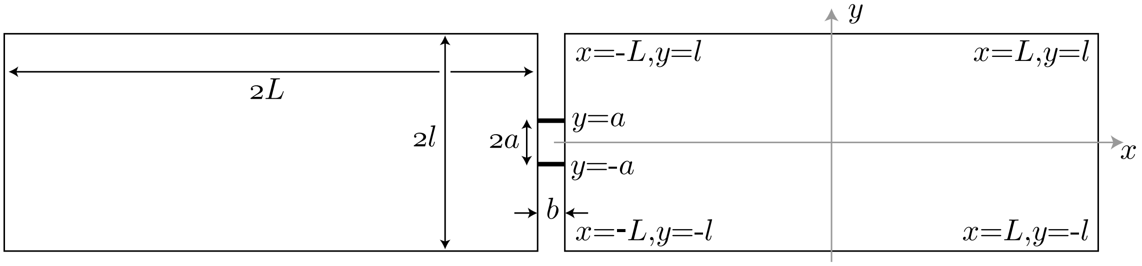

Figure 2.2: Geometry of the two-wire device, showing the dimensions. The coordinate system used for the right lead (with the origin in the center of the lead) is also shown. The coordinates of the four corners of the right lead, as well as the coordinates of the points at which the two wires are connected to the right lead, are indicated. As shown, we always assume that the wires are attached near the center of the short edges of the leads.

current oscillations observed in SQUID rings. What distinguishes the resistance oscillations reported in Ref. [38] from those found, e.g., by Little and Parks? First, the most notable aspect of these oscillations is the value of their period. In the Little-Parks type of experiment, the period is given by $\Phi_0/2ab$, where $\Phi_0(\equiv hc/2e)$ is the superconducting flux quantum, $2a$ is the bridge separation, and $b$ is the bridge length, i.e., the superconducting flux quantum divided by the area of the AB contour (see Fig. 2.2). In a high-magnetic-field regime, such periodic behavior is indeed observed experimentally, with the length of the period somewhat shorter but of the same order of magnitude as in the AB effect [38]. However, in a low-magnetic-field regime, the observed period is appreciably smaller (in fact by almost two orders of magnitude for our device geometry). Second, because the resistance is caused by thermal phase fluctuations (i.e. phase slips) in very narrow wires, the oscillations are observable over a wide range of temperatures ($\sim 1\,\mathrm{K}$). Third, the Little-Parks resistance is wholly ascribed to a rigid shift of the $R(T)$ curve with magnetic field, as $T_{\mathrm{c}}$ oscillates. In contrast, in our system we observe a periodic broadening of the transition (instead of the Little-Parks—type rigid shift) with magnetic field. Our theory explains quantitatively this broadening via the modulation of the barrier heights for phase slips of the superconducting order parameter in the nanowires.

In the experiment, the sample is cooled in zero magnetic field, and the field is then slowly increased while the resistance is measured. At a sample-dependent field ($\sim 5\,\mathrm{mT}$) the behavior switches sharply from a low-field to a high-field regime. If the high-field regime is not reached before the magnetic field is swept back, the low-field resistance curve is reproduced. However, once the high-field regime has been reached, the sweeping back of the field reveals phase shifts and hysteresis in the $R(B)$ curve. The experiments [38] mainly address rectangular leads that have one mesoscopic and one macroscopic dimension. Therefore, we shall concentrate on such strip geometries. We shall, however, also discuss how to extend our approach to generic (mesoscopic) lead shapes. We note in passing that efficient numerical methods, such as the boundary element method (BEM) [39], are available for solving the corresponding Laplace problems.

This chapter is arranged as follows. In Section 2.2 we construct a basic picture for the period of the magnetoresistance oscillations of the two-wire device, which shows how the mesoscopic size of the leads accounts for the anomalously short magnetoresistance period in the low-field regime. In Section 2.3 we concentrate on the properties of mesoscopic leads with regard to their response to an applied magnetic field, and in Section 2.4 we extend the LAMH model to take into account the inter-wire coupling through the leads. Analytical expressions are derived for the short- and long-wire limits, whilst a numerical procedure is described for the general case. The predictions of the model are compared with data from our experiment in Section 2.5, and we give some concluding remarks in Section 2.8. Certain technical components are relegated to the appendix, as is the analysis of example multiwire devices.

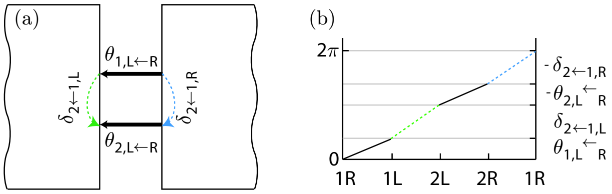

Figure 2.3: Phase accumulations around the gradiometer: (a) Close-up of the two nanowires and the leads. The top (bottom) thick arrow represents the integration contour for determining the phase accumulation $\theta_{1,L\leftarrow R}$ ($\theta_{2,L\leftarrow R}$) in the first (second) wire. The dotted arrow in the left (right) lead indicates a possible choice of integration contour for determining the phase accumulation $\delta_{2\leftarrow 1,L}$ ($\delta_{2\leftarrow 1,R}$). These contours may be deformed without affecting the values of the various phase accumulations, as long as no vortices are crossed. (b) Sketch of the corresponding superconducting phase at different points along the AB contour when one vortex is located inside the contour.

## 2.2 Origin of magnetoresistance oscillations

Before presenting a detailed development of the theory, we give an intuitive argument to account for the anomalously-short period of the magnetoresistance in the low-magnetic-field regime, mentioned above.

### 2.2.1 Device geometry

The geometry of the devices studied experimentally is shown in Fig. 2.2. Five devices were successfully fabricated and measured. The dimensions of these devices are listed in Table 2.1, along with the short magnetoresistance oscillation period. The perpendicular penetration depth $\lambda_\perp$ for the films used to make the leads is roughly $70\,\mu$m, and coherence length $\xi$ is roughly 5 nm.

### 2.2.2 Parametric control of the state of the wires by the leads

The essential ingredients in our model are (i) leads, in which the applied magnetic field induces supercurrents and hence gradients in the phase of the order parameter, and (ii) the two wires, whose behavior is controlled parametrically by the leads through the boundary conditions imposed by the leads on the phase of the order parameters in the wires. For now, we assume that the wires have sufficiently small cross-sections that the currents through them do not feed back on the order parameter in the leads. (In Section 2.3.4 we shall discuss when this assumption may be relaxed without altering the oscillation period.) The dissipation results from thermally activated phase slips, which cause the superconducting order parameter to explore a discrete family of local minima of the free energy. (We assume that the barriers separating these minima are sufficiently high to make them well-defined states.) These minima (and the saddle-point configurations connecting them) may be indexed by the net (i.e. forward minus reverse) number of phase slips that have occurred in each wire ($n_1$ and $n_2$, relative to some reference state). More usefully, they can be indexed by

$n_s = \min(n_1, n_2)$ (i.e. the net number of phase slips that have occurred in both wires) and $n_v = n_1 - n_2$ (i.e. the number of vortices enclosed by the AB contour, which is formed by the wires and the edges of the leads). We note that two configurations with identical $n_v$ but distinct $n_s$ and $n'_s$ have identical order parameters, but differ in energy by

$$\int IV\,dt = \frac{\hbar}{2e}\int I\dot{\Theta}\,dt = \frac{h}{2e}\,I\,(n'_s - n_s), \tag{2.1}$$

due to the work done by the current source supplying the current $I$, in which $V$ is the inter-lead voltage, $\Theta$ is the inter-lead phase difference as measured between the two points half-way between the wires, and the Josephson relation $\dot{\Theta} = 2eV/\hbar$ has been invoked. In our model, we assume that the leads are completely rigid. Therefore the rate of phase change, and thus the voltage, is identical at all points inside one lead. For sufficiently short wires, $n_v$ has a unique value, as there are no stable states with any other number of vortices.

Due to the screening currents in the left lead, induced by the applied magnetic field $B$ (and independent of the wires), there is a field-dependent phase $\delta_{2\leftarrow 1,L}(B) = \int_1^2 d\vec{r}\cdot\vec{\nabla}\varphi(B)$ (computed below) accumulated in passing from the point at which wire 1 (the top wire) contacts the left (L) lead to the point at which wire 2 (the bottom wire) contacts the left lead (see Fig. 2.3). Similarly, the field creates a phase accumulation $\delta_{2\leftarrow 1,R}(B)$ between the contact points in the right (R) lead. As the leads are taken to be geometrically identical, the phase accumulations in them differ in sign only: $\delta_{2\leftarrow 1,L}(B) = -\delta_{2\leftarrow 1,R}(B)$. We introduce $\delta(B) = \delta_{2\leftarrow 1,L}(B)$. In determining the local free-energy minima of the wires, we solve the Ginzburg-Landau equation for the wires for each vortex number $n_v$, imposing the single-valuedness condition on the order parameter,

$$\theta_{1,L\leftarrow R} - \theta_{2,L\leftarrow R} + 2\delta(B) = 2\pi n_v. \tag{2.2}$$

This condition will be referred to as the *phase constraint*. Here, $\theta_{1,L\leftarrow R} = \int_R^L d\vec{r}\cdot\vec{\nabla}\varphi(B)$ is the phase accumulated along wire 1 in passing from the right to the left lead; $\theta_{2,L\leftarrow R}$ is similarly defined for wire 2.

Absent any constraints, the lowest energy configuration of the nanowires is the one with no current through the wires. Here, we adopt the gauge in which $\boldsymbol{A} = By\boldsymbol{e}_x$ for the electromagnetic vector potential, where the coordinates are as shown in Fig. 2.2. The Ginzburg-Landau expression for the current density in a superconductor is

$$\boldsymbol{J} \propto \left(\boldsymbol{\nabla}\varphi(\boldsymbol{r}) - \frac{2e}{\hbar}\boldsymbol{A}(\boldsymbol{r})\right). \tag{2.3}$$

For our choice of gauge, the vector potential is always parallel to the nanowires, and therefore the lowest energy state of the nanowires corresponds to a phase accumulation given by the flux through the AB contour, $\theta_{1,L\leftarrow R} = -\theta_{2,L\leftarrow R} = 2\pi Bab/\Phi_0$. As we shall show shortly, for our device geometry (i.e. when the wires are sufficiently short, i.e., $b \ll l$), this phase accumulation may be safely ignored, compared to the phase accumulation $\delta(B)$ associated with screening currents induced in the leads. As the nanowires are assumed to be weak compared to the leads, to satisfy the phase constraint (2.2), the phase accumulations in the nanowires will typically deviate from their optimal value, generating a circulating current around the AB contour. As a consequence of LAMH theory, this circulating current results in a decrease of the barrier heights for phase slips, and hence an increase in resistance. The period of the observed oscillations is derived from the fact that whenever the magnetic field satisfies the relation

$$2\pi m = 2\pi \frac{2abB}{\Phi_0} + 2\delta(B) \tag{2.4}$$

[where $m$ is an integer and the factor of 2 accompanying $\delta(B)$ reflects the presence of two leads], there is no circulating current in the lowest in energy state, resulting in minimal resistance. Furthermore, the family of free energy-minima of the two-wire system (all of which, in thermal equilibrium, are statistically populated according to their energies) is identical to the $B = 0$ case. The mapping between configurations at zero and nonzero $B$ fields is established by a shift of the index $n_v \to n_v - m$. Therefore, as the sets of physical states of the wires are identical whenever the periodicity condition (2.4) is satisfied, at such values of $B$ the resistance returns to its $B = 0$ value.

### 2.2.3 Simple estimate of the oscillation period

In this subsection, we will give a "back of the envelope" estimate for the phase gain $\delta(B)$ in a lead by considering the current and phase profiles in one such lead. According to the Ginzburg-Landau theory, in a mesoscopic superconductor, subjected to a weak magnetic field, the current density is given by Eq. (2.3). Now consider an isolated strip-shaped lead used in the device. Far from either of the short edges of this lead, $\boldsymbol{A} = By\boldsymbol{e}_x$ is a London gauge [9, 34], i.e., along all surfaces of the superconductor $\boldsymbol{A}$ is parallel to them; $\boldsymbol{A} \to 0$ in the center of the superconductor; and $\boldsymbol{\nabla} \cdot \boldsymbol{A} = 0$. In this special case, the London relation [1] states that the supercurrent density is proportional to the vector potential in the London gauge. Using this relation, we find that the supercurrent density is $\boldsymbol{J} \propto -(2e/\hbar)\,\boldsymbol{A} = -(2e/\hbar)\,By\boldsymbol{e}_x$, i.e., there is a

---

[1] Consider the case in which $\boldsymbol{A}$ is a London gauge everywhere (with our choice of gauge, $\boldsymbol{A} = By\boldsymbol{e}_x$, this is the case for an infinitely long strip). By using the requirement that $\boldsymbol{\nabla} \cdot \boldsymbol{A} = 0$, together with Eq. (2.13b), we see that $\phi$ satisfies the Laplace equation. We further insist that no current flows out of the superconductor, i.e., along all surfaces the supercurrent density, Eq. (2.12), is always parallel to the surface. Together with the requirement that along all surfaces $\boldsymbol{A}$ is parallel to them, this implies the boundary condition that $\boldsymbol{n} \cdot \boldsymbol{\nabla}\phi = 0$. Next, it can be shown that this boundary condition implies that $\phi$ must be a constant function of position in order to satisfy the Laplace equation, and therefore Eq. (2.12) simplifies to read $\boldsymbol{J} = -(c/8\pi\lambda_{\text{eff}}^2)\boldsymbol{A}$, which is known as the London relation.

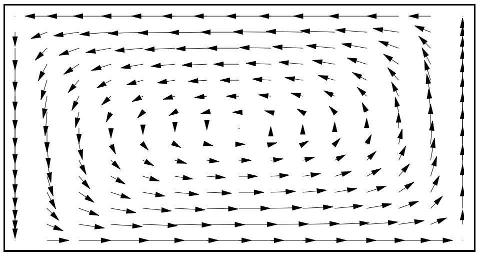

Figure 2.4: Current profile in a long superconducting strip, calculated for a finite-length strip by summing the series for $\boldsymbol{\nabla}\phi - \frac{2\pi}{\Phi_0}\boldsymbol{A}$ [from Eq. (2.15)] numerically. Note that there is no vortex in the center of the lead.

supercurrent density of magnitude $\propto (2e/\hbar)\,Bl$ flowing to the left at the top (long) edge of the strip and to the right at the bottom (long) edge. At the two short ends of the strip, the two supercurrents must be connected, so there is a supercurrent density of magnitude $\sim (2e/\hbar)Bl$ flowing down the left (short) edge of the strip and up the right (short) edge (see Fig. 2.4). Near the short ends of the strips, our choice of gauge no longer satisfies the criteria for being a London gauge, and therefore $\boldsymbol{\nabla}\phi$ may be nonzero. As, in our choice of gauge, $\boldsymbol{A}$ points in the $\boldsymbol{e}_x$ direction, the supercurrent on the ends of the strip along $\boldsymbol{e}_y$ must come from the $\nabla_y\phi$ term. Near the center of the short edge $\nabla_y\phi = -2\pi c_1 l/\Phi_0 B$. The phase difference between the points $(-L,-a)$ and $(-L,a)$ is therefore given by

$$\delta(B) = \int_{-a}^{a} \nabla_y\phi\,dy = -\frac{2\pi c_1}{\Phi_0}B\,2al, \tag{2.5}$$

where we have substituted $2\pi/\Phi_0$ for $2e/\hbar$ and $c_1(a/l)$ is a function of order unity, which accounts for how the current flows around the corners. As we shall show, $c_1$ depends only weakly on $a/l$, and is constant in the limit $a \ll l$.

Finally, we obtain the magnetoresistance period by substituting Eq. (2.5) into Eq. (2.4):

$$\Delta B = \left[\left(\frac{\Phi_0}{c_1\,4al}\right)^{-1} + \left(\frac{\Phi_0}{2ab}\right)^{-1}\right]^{-1}. \tag{2.6}$$

Thus, we see that for certain geometries the period is largely determined not by the flux threading through the geometric area $2ab$ but by the response of the leads and the corresponding effective area $4al$, provided the nanowires are sufficiently short (i.e. $b \ll l$), justifying our assumption of ignoring the phase gradient induced in the nanowires by the magnetic field.

In fact, we can also make a prediction for the periodicity of the magnetoresistance at high magnetic fields, i.e., when vortices have penetrated the leads (see Section 2.3.1). To do this, we should replace $l$ in Eq. (2.6) by the characteristic inter-vortex spacing $r$. Note that if $r$ is comparable to $b$, we can no longer ignore the flux through the AB contour. Furthermore, if $r \ll b$ then the flux through the AB contour determines periodicity and one recovers the usual Aharonov-Bohm type of phenomenology.

## 2.3 Mesoscale superconducting leads

In this section and the following one we shall develop a detailed model of the leads and nanowires that constitute the mesoscopic device.

### 2.3.1 Vortex-free and vorticial regimes

Two distinct regimes of magnetic field are expected, depending on whether or not there are trapped (i.e. locally stable) vortices inside the leads. As described by Likharev [40, 41, 42], a vortex inside a superconducting strip-shaped lead is subject to two forces. First, due to the the currents induced by the magnetic field there is a Magnus force pushing it towards the middle of the strip. Second, there is a force due to image vortices (which are required to enforce the boundary condition that no current flows out of the strip and into the vacuum) pulling the vortex towards the edge. When the two forces balance at the edge of the strip, there is no energy barrier preventing vortex penetration and vortices enter. Likharev has estimated of the corresponding critical magnetic field to be

$$H_{\mathrm{s}} \approx \frac{\Phi_0}{\pi d} \frac{1}{\xi a(1)}, \tag{2.7}$$

where $d(\equiv 2l)$ is the width of the strip and $a(1) \sim 1$ for strips that are much narrower than the penetration depth (i.e. for $d \ll \lambda$).

Likharev has also shown that, once inside a strip, vortices remain stable inside it down to a much lower magnetic field $H_{c1}$, given by

$$H_{\mathrm{c}1} = \frac{\Phi_0}{\pi d} \frac{2}{d} \ln\left(\frac{d}{4\xi}\right). \tag{2.8}$$

At fields above $H_{\mathrm{c}1}$ the potential energy of a vortex inside the strip is lower than for one outside (i.e. for a virtual vortex [2]). Therefore, for magnetic fields in the range $H_{\mathrm{c}1} < H < H_{\mathrm{s}}$ vortices would remain trapped inside the strip, but only if at some previous time the field were larger than $H_{\mathrm{s}}$. This indicates that hysteresis with respect to magnetic field variations should be observed, once $H$ exceeds $H_{\mathrm{s}}$ and vortices become trapped in the leads.

---

[2] Here and elsewhere, we speak of vortices and antivortices entering or leaving the leads or the loop made by the wires. Of course, outside the superconducting regions there can be no vortices or antivortices. Nevertheless, we use this language to connote the temporary reduction of the amplitude of the superconducting order parameter during a dissipative fluctuation, and its global consequences for the phase of the order parameter.

In real samples, in addition to the effects analyzed by Likharev, there are also likely to be locations (e.g. structural defects) that can pin vortices, even for fields smaller than $H_{c1}$, so the reproducibility of the resistance *vs.* field curve is not generally expected once $H_\mathrm{s}$ has been surpassed.

As magnetic field at which vortices first enter the leads is sensitive to the properties of their edges, we expect only rough agreement with Likharev's theory. For sample 219-4, using Likharev's formula, we estimate $H_\mathrm{s} = 11\,\mathrm{mT}$ (with $\xi = 5\,\mathrm{nm}$). The change in regime from fast to slow oscillations is found to occur at 3.1 mT for that sample [38]. It is possible to determine the critical magnetic fields $H_\mathrm{s}$ and $H_\mathrm{c1}$ by the direct imaging of vortices. Although we do not know of such a direct measurement of $H_\mathrm{s}$, $H_\mathrm{c1}$ was determined by field cooling niobium strips, and found to agree in magnitude to Likharev's estimate [43].

### 2.3.2 Phase variation along the edge of the lead

In the previous section it was shown that the periodicity of the magnetoresistance is due to the phase accumulations associated with the currents along the edges of the leads between the nanowires. Thus, we should make a precise calculation of the dependence of these currents on the magnetic field, and this we now do.

#### Ginzburg-Landau theory

To compute $\delta(B)$, we start with the Ginzburg-Landau equation for a thin film as our description of the mesoscopic superconducting leads:

$$\alpha\psi + \beta|\psi|^2\psi + \frac{1}{2m^*}\left(\frac{\hbar}{i}\boldsymbol{\nabla} - \frac{e^*}{c}\boldsymbol{A}\right)^2\psi = 0. \tag{2.9}$$

Here, $\psi$ is the Ginzburg-Landau order parameter, $e^*$ $(= 2e)$ is the charge of a Cooper pair and $m^*$ is its mass, and $\alpha$ and $\beta$ may be expressed in terms of the coherence length $\xi$ and critical field $H_\mathrm{c}$ via $\alpha = -\hbar^2/2m^*\xi^2$ and $\beta = 4\pi\alpha^2/H_\mathrm{c}^2$.

The assumptions that the magnetic field is sufficiently weak and that the lead is a narrow strip (compared with the magnetic penetration depth) allow us to take the *amplitude* of the order parameter in the leads to have the value appropriate to an infinite thin film in the absence of the field. By expressing the order parameter in terms of the (constant) amplitude $\psi_0$ and the (position-dependent) phase $\phi(\boldsymbol{r})$, i.e.,

$$\psi(\boldsymbol{r}) = \psi_0\, e^{i\phi(\boldsymbol{r})}, \tag{2.10}$$

the Ginzburg-Landau formula for the current density,

$$\boldsymbol{J} = \frac{e^*\hbar}{2m^*i}\big(\psi^*\boldsymbol{\nabla}\psi - \psi\boldsymbol{\nabla}\psi^*\big) - \frac{{e^*}^2}{m^*c}\psi^*\psi\boldsymbol{A}(\boldsymbol{r}), \tag{2.11}$$

becomes

$$\boldsymbol{J} = \frac{e^*}{m^*}\psi_0^2\big(\hbar\boldsymbol{\nabla}\phi(\boldsymbol{r}) - \frac{e^*}{c}\boldsymbol{A}(\boldsymbol{r})\big), \tag{2.12}$$

and [after dividing by $e^{i\phi(\boldsymbol{r})}$] the real and imaginary parts of the Ginzburg-Landau equation become

$$0 = \left[\alpha\,\psi_0 + \beta\,\psi_0^3 + \frac{1}{2m^*}\psi_0\left|\hbar\boldsymbol{\nabla}\phi(\boldsymbol{r}) - \frac{e^*}{c}\boldsymbol{A}(\boldsymbol{r})\right|^2\right], \tag{2.13a}$$

$$0 = \frac{\hbar^2}{2m^*i}\,\psi_0\left(\nabla^2\phi(\boldsymbol{r}) - \frac{e^*}{\hbar c}\boldsymbol{\nabla}\cdot\boldsymbol{A}(\boldsymbol{r})\right). \tag{2.13b}$$

As long as any spatial inhomogeneity in the gauge-covariant derivative of the phase is weak on the length-scale of the coherence length $\big[$ i.e. $\xi\big|\boldsymbol{\nabla}\phi(\boldsymbol{r}) - \frac{e^*}{\hbar c}\boldsymbol{A}(\boldsymbol{r})\big| \ll 1$ $\big]$, the third term in Eq. (2.13a) is much smaller than the first two and may be ignored, fixing the amplitude of the order parameter at its field-free infinite thin film value, *viz.*, $\bar{\psi_0} \equiv \sqrt{-\alpha/\beta}$. To compute $\phi(\boldsymbol{r})$ we need to solve the imaginary part of the Ginzburg-Landau equation.

### Formulation as a Laplace problem

We continue to work in the approximation that the amplitude of the order parameter is fixed at $\bar{\psi_0}$. Starting from Eq. (2.13b), we see that for our choice of gauge, $\boldsymbol{A} = By\boldsymbol{e}_x$, the phase of the order parameter satisfies the Laplace equation, $\nabla^2\phi = 0$. We also enforce the boundary condition that no current flows out of the superconductor on boundary surface $\Sigma$, whose normal is $\mathbf{n}$:

$$\boldsymbol{n}\cdot\boldsymbol{j}\big|_{\Sigma} = 0, \tag{2.14a}$$

$$\boldsymbol{j} \propto \Big(\boldsymbol{\nabla}\phi - \frac{2\pi}{\Phi_0}\boldsymbol{A}\Big). \tag{2.14b}$$

### Solving the Laplace problem for the strip geometry

To solidify the intuition gained via the physical arguments given in Section 2.2, we now determine the phase profile for an isolated superconducting strip in a magnetic field. This will allow us to determine the constant $c_1$ in Eq. (2.6), and hence obtain a precise formula for the magnetoresistance period. To this end, we solve Laplace's equation for $\phi$ subject to the boundary conditions (2.14). We specialize to the case of a rectangular

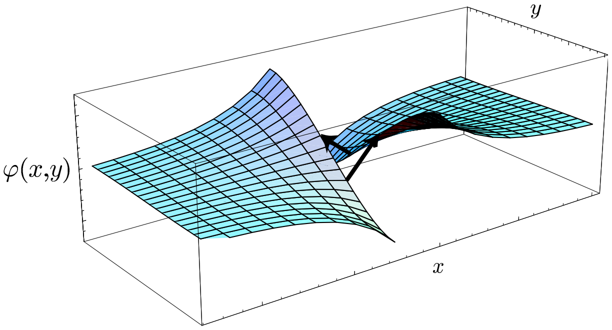

Figure 2.5: Phase profile in the leads in the vicinity of the trench, generated by numerically summing the series for $\phi$ for a finite-length strip. Arrows indicate phases connected by nanowires.

strip [3].

In terms of the coordinates defined in Fig. 2.2, we expand $\phi(x, y)$ as the superposition

$$\phi(x,y) = \Theta_{\mathrm{L/R}} + \sum_k \left(A_k\, e^{-kx} + B_k\, e^{kx}\right)\sin(ky), \tag{2.15}$$

which automatically satisfies Laplace's equation, although the boundary conditions remain to be satisfied. $\Theta_{\mathrm{L(R)}}$ is the phase at the the point in the left (right) lead located half-way between the wires. In other words $\Theta_L = \phi(-L - b, 0)$ and $\Theta_R = \phi(-L, 0)$ in the coordinate system indicated in Fig. 2.2. $\Theta_{\mathrm{L/R}}$ are not determined by the Laplace equation and boundary conditions, but will be determined later by the state of the nanowires.

We continue working in the gauge $\boldsymbol{A} = By\,\boldsymbol{e}_x$. The boundary conditions across the edges at $y = \pm l$ (i.e. the long edges) are $\partial_y\phi(x, y = \pm l) = 0$. These conditions are satisfied by enforcing $k_n = \pi(n + \frac{1}{2})/l$, where $n = 0, 1, 2, \ldots$. The boundary conditions across the edges at $x = \pm L$ (i.e. the short edges) are $\partial_x\phi(x = \pm L, y) = hy$ (where $h \equiv 2\pi B/\Phi_0$). This leads to the coefficients in Eq. (2.15) taking the values

$$B_k = -A_k = \frac{h}{k_n^3 l}\frac{(-1)^n}{\cosh(k_n L)} \qquad\qquad (n = 0, 1, \ldots), \tag{2.16}$$

and hence to the solution

$$\phi(x,y) = \sum_{n=0}^{\infty} \frac{(-1)^n\, 2h}{k_n^3 l\cosh(k_n L)}\, \sin(k_n y)\, \sinh(k_n x). \tag{2.17}$$

Figure 2.5 shows the phase profiles in the leads, in the region close to the trench that separates the leads.

---

[3] This specialization is not necessary, but it is convenient and adequately illustrative

### 2.3.3 Period of magnetoresistance for leads having a rectangular strip geometry

Using the result for the phase that we have just established, we see that the phase profile on the short edge of the strip at $x = -L$ is given by

$$\phi(-L, y) = -\frac{2hl^2}{\pi^2} \sum_{n=0}^{\infty} \frac{(-1)^n}{(n+\frac{1}{2})^3} \sin \frac{\pi \left(n + \frac{1}{2}\right) y}{l}, \tag{2.18}$$

where we have taken the limit $L \to \infty$. We would like to evaluate this sum at the points $(x, y) = (-L, \pm a)$. This can be done numerically. For nanowires that are close to each other (i.e. for $a \ll l$), an approximate value can be found analytically by expanding in a power series in $a$ around $y = 0$:

$$\begin{aligned} \phi(-L, a) = \phi(-L, 0) + a \; \frac{\partial}{\partial y}\phi(-L, y)\bigg|_{y=0} \\ + \frac{a^2}{2} \; \frac{\partial^2}{\partial y^2}\phi(-L, y)\bigg|_{y=0} + O(a^3). \end{aligned} \tag{2.19}$$

The first and third terms are evidently zero, as $\phi$ is an odd function of $y$. The second term can be evaluated by changing the order of summation and differentiation. (Higher-order terms are harder to evaluate, as the changing of the order of summation and differentiation does not work for them.) Thus, to leading order in $a$ we have

$$\phi(-L, a) \approx -\frac{8G}{\pi^2} hla, \tag{2.20}$$

where $G \equiv \sum_{n=0}^{\infty} \frac{(-1)^n}{(2n+1)^2} \approx 0.916$ is the Catalan number (see Ref. [44]). This linear approximation is plotted, together with the actual phase profile obtained by the numerical evaluation of Eq. (2.18), in Fig. 2.6. Hence, the value of $c_1$ in Eq. (2.5) becomes $c_1 = 8G/\pi^2 \approx 0.74$, and Eq. (2.6) becomes

$$B = \frac{\Phi_0}{2\pi} h = \frac{\pi^2}{8G} \frac{\Phi_0}{4al}. \tag{2.21}$$

To obtain this result we used the relation $\delta(B)/2 = \phi(-L, a)$.

### 2.3.4 Bridge-lead coupling

In order to simplify our analysis we have assumed that the nanowires do not exert any influence on the order parameter in the leads. We examine the justification for this assumption in the setting of the experiment

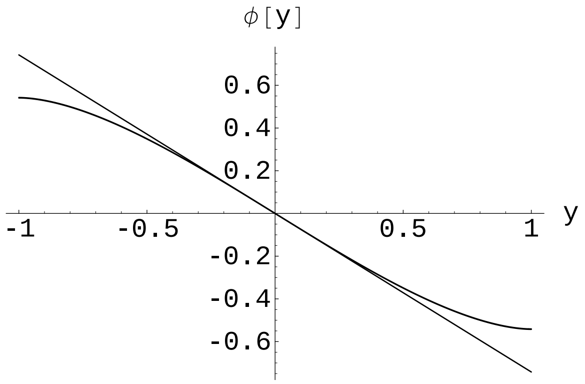

Figure 2.6: Phase profile on the $x = -L$ (i.e. short) edge of the strip. Numerical summation [Eq. (2.18) with 100 terms] for $L = 2$ and $L = \infty$ ($l = 1$) as well as the linear form from Eq. (2.20). Note that the linear fit is good near the origin (e.g. for $a \lesssim 0.25l$), and the curves for $L = 2$ and $L = \infty$ coincide.

that we are attempting to describe [38].

The assumption will be valid if the bending of the phase of the order parameter, in order to accommodate any circulating current around the AB contour, occurs largely in the nanowires. As the phase of the order parameter in the leads satisfies the Laplace equation, which is linear, we can superpose the circulating-current solution with the previously-obtained magnetic-field-induced solution. The boundary conditions on the right lead for the circulating-current solution are $\boldsymbol{n} \cdot \boldsymbol{\nabla}\phi = 0$ everywhere, except at the two points where the nanowires are attached to the lead [i.e. at $(x, y) = (L, \pm a)$]. Treating the nanowires as point current sources, the boundary condition on the short edge of the right lead is $\partial_x \phi = I(\Phi_0/H_c^2 s\xi)(\delta(y+a) - \delta(y-a))$, where $I$ is the current circulating in the loop, and $H_c$, $s$, $\xi$ are the film critical field, thickness, and coherence length. By using the same expansion as before, Eq. (2.15), we obtain the coefficients of the Fourier-series in the long strip limit:

$$A_k = I(\Phi_0/H_c^2 s\xi)\frac{2\sin(ka)}{kl\exp(kl)}. \tag{2.22}$$

Having the coefficients of the Fourier series, we can find the phase difference in the right lead between the two points at which the nanowires connect to the right lead, induced in this lead by the current circulating in the loop:

$$\delta_{cc} = 2I(\Phi_0/H_c^2 s\xi)\sum_{n=0}^{k=1/w}\frac{\sin^2(ka)}{kl} \sim \ln(2l/\pi w). \tag{2.23}$$

Here, we have introduced a large wave-vector $k$ cut-off at the inverse of the width $w$ of the wire. On the other hand, the current flowing through the wire is

$$\frac{\xi H_{\mathrm{c}}^2}{\Phi_0} ws \frac{\Delta\theta}{b}, \tag{2.24}$$

where $\xi$, $H_{\mathrm{c}}$, and $s$ are the wire coherence length, critical field, and height (recall that $b$ is the wire length). To support a circulating current that corresponds to a phase accumulation of $\Delta\theta$ along one of the wires, the phase difference between the two nanowires in the lead must be on the order of

$$\delta_{cc} = \Delta\theta \frac{w}{b} \frac{\left(H_{\mathrm{c}}^2 s\xi\right)_{\mathrm{wire}}}{\left(H_{\mathrm{c}}^2 s\xi\right)_{\mathrm{film}}} \ln\left(\frac{2l}{\pi w}\right). \tag{2.25}$$

For our experiments [38], we estimate that the ratio of $\delta_{cc}$ to $\Delta\theta$ is always less than 20%, validating the assumption of weak coupling.

### 2.3.5 Strong nanowires

We remark that the assumption of weak nanowires *is not obligatory* for the computation the magnetoresistance *period*. Dropping this assumption would leave the period of the magnetoresistance oscillations unchanged.

To see this, consider $\phi_{11}$, i.e., the phase profile in the leads that corresponds to the lowest energy solution of the Ginzburg-Landau equation at field corresponding to the first resistance minimum [i.e. at B being the first non-zero solution of Eq. (2.4)]. For this case, and for short wires, the phase gain along the wires is negligible, whereas the phase gain in the leads is $2\pi$, even for wires with large critical current. Excited states, with vortices threading the AB contour, can be constructed by the linear superposition of $\phi_{11}$ with $\phi_{0n_v}$, where $\phi_{0n_v}$ is the phase profile with $n_v$ vortices at no applied magnetic field.

This construction requires that the nanowires are narrow, but works independently of whether nanowires are strong or weak, in the limit that $H \ll H_{\mathrm{c}}$. The energy of the lowest energy state always reaches its minimum when the applied magnetic field is such that there is no phase gain (i.e. no current) in the nanowires. By the above construction, it is clear that the resistance of the device at this field is the same as at zero field, and therefore the minimum possible.

Therefore, our calculation of the period is valid, independent of whether the nanowires are weak or strong. However, the assumption of weak nanowires is necessary for the computation of magnetoresistance amplitude, which we present in the following section.

## 2.4 Parallel superconducting nanowires and intrinsic resistance

In this section we consider the intrinsic resistance of the device. We assume that this resistance is due to thermally activated phase slips (TAPS) of the order parameter, and that these occur within the nanowires. Equivalently, these processes may be thought of as thermally activated vortex flow across the nanowires. Specifically, we shall derive analytical results for the asymptotic cases of nanowires that are either short or long, compared to coherence length, i.e. Josephson junctions [3, 4, 5] or Langer-Ambegaokar-McCumber-Halperin (LAMH) wires [6, 7]; see also Ref. [29]. We have not been able to find a closed-form expression for the intrinsic resistance in the intermediate-length regime, so we shall consider that case numerically.

There are two (limiting) kinds of experiments that may be performed: fixed total current and fixed voltage. In the first kind, a specified current is driven through the device and the time-averaged voltage is measured. Here, this voltage is proportional to the net number of phase slips (in the forward direction) per unit time, which depends on the height of the free-energy barriers for phase slips. Why do we expect minima in the resistance at magnetic fields corresponding to $2\delta = 2m\pi$ and maxima at $2\delta = (2m+1)\pi$ for $m$ integral, at least at vanishingly small total current through both wires? For $2\delta = 2m\pi$ the nanowires are unfrustrated, in the sense that there is no current through either wire in the lowest local minimum of the free energy. On the other hand, for $2\delta = (2m+1)\pi$ the nanowires are maximally frustrated: there is a nonzero circulating current around the AB contour. Quite generally, the heights of the free-energy barriers protecting locally stable states decrease with increasing current through a wire, and thus the frustrated situation is more susceptible to dissipative fluctuations, and hence shows higher resistance. Note, however, that due to the inter-bridge coupling caused by the phase constraint, the resistance of the full device is more subtle than the mere addition of the resistances of two independent, parallel nanowires, both carrying the requisite circulating current.

In the second kind of experiment, a fixed voltage is applied across the device and the total current is measured. In this situation, the inter-lead voltage is fixed, and therefore the phase drop along each wire is a fixed function of time. Hence, there is no inter-bridge coupling in the fixed voltage regime. Therefore, the resistance of the device would not exhibit magnetic field dependence. If the voltage is fixed far away from the wires, but not in the immediate vicinity of the wires, so that the phase drop along each wire is not rigidly fixed, then some of the magnetic field dependence of the resistance would be restored. In our experiments on two-wire devices, we believe that the situation lies closer to the fixed current limit than to the fixed voltage limit, and therefore we shall restrict our attention to the former limit.

In the fixed-current regime, the relevant independent thermodynamic variable for the device is the total current through the pair of wires, i.e., $I \equiv I_1 + I_2$. Therefore, the appropriate free energy to use, in obtaining the barrier heights for phase slips, is the Gibbs free energy $G(I)$, as discussed by McCumber [30], rather than the Helmholtz free energy $F(\Theta)$ [4]. In the Helmholtz free energy the independent variable can be taken to be $\Theta \equiv \Theta_{\mathrm{L}} - \Theta_{\mathrm{R}}$, i.e., the phase difference across the center of the "trench," defined modulo $2\pi$. $G(I)$ is obtained from $F(\Theta)$ via the appropriate Legendre transformation:

$$G(I) = F(\Theta) - \frac{\hbar}{2e} I \Theta, \tag{2.26}$$

where the second term represents the work done on the system by the external current source. $F(\Theta)$ is the sum of the Helmholtz free energies for the individual nanowires:

$$F(\Theta) = F_1(\theta_1) + F_2(\theta_2), \tag{2.27}$$

where $F_{1(2)}(\theta_{1(2)})$ is the Ginzburg-Landau free energy for first (second) wire and a simplified notation has been used $\theta_1 \equiv \theta_{1,L\leftarrow R}$ and $\theta_2 \equiv \theta_{2,L\leftarrow R}$. $\theta_1$ and $\theta_2$ are related to each other and to $\Theta$ through the phase constraint Eq. (2.2).

### 2.4.1 Short nanowires: Josephson junction limit

If the nanowires are sufficiently short, they may be treated as Josephson junctions. Unlike the case of long nanowires, described in the following subsection, in this Josephson regime there is no metastability, i.e., the free energy of each junction is a single-valued function of the phase difference, modulo $2\pi$, across it. The phase constraint then implies that there is a rigid difference between the phases across the two junctions. As a consequence, $n_v$ can be set to zero. The Gibbs free energy in such a configuration is then

$$G(I) = -\frac{\hbar}{2e}\Big(I_{\mathrm{c}1}\cos(\theta_1) + I_{\mathrm{c}2}\cos(\theta_2) + I\Theta\Big), \tag{2.28}$$

where $I_{\mathrm{c}1}$ and $I_{\mathrm{c}2}$ are the critical currents for the junctions. In thermodynamic equilibrium, the Gibbs free energy must be minimized, so the dependent variable $\Theta$ must be chosen such that $\partial G(I)/\partial\Theta = 0$.

Using $\theta_1 = \Theta + \delta$ and $\theta_2 = \Theta - \delta$, $G(I)$ may be rewritten in the form

$$\tilde{G}(I) = -\frac{\hbar}{2e}\Big(\sqrt{(I_{\mathrm{c}1}+I_{\mathrm{c}2})^2\cos^2\delta + (I_{\mathrm{c}1}-I_{\mathrm{c}2})^2\sin^2\delta}\cdot\cos(\vartheta) + I\,\vartheta_1\Big), \tag{2.29}$$

where we have shifted the free energy by an additive constant $\left(\frac{\hbar}{2e}\right) I \tan^{-1}\left[\left(\frac{I_{\mathrm{c}1}-I_{\mathrm{c}2}}{I_{\mathrm{c}2}+I_{\mathrm{c}1}}\right)\tan\delta\right]$, and $\vartheta \equiv$

---

[4] Recall that the Helmholtz free energy is obtained by minimizing the Ginzburg-Landau free energy functional with respect to the order parameter function $\psi(\boldsymbol{r})$, subject to the phase accumulation constraint $\int_{\mathrm{L}}^{\mathrm{R}} d\boldsymbol{r}\cdot\boldsymbol{\nabla}\phi = \theta$.

$\Theta + \tan^{-1}\left[\left(\frac{I_{c1}-I_{c2}}{I_{c2}+I_{c1}}\right)\tan\delta\right]$. In this model, the option for having $I_{c1} \neq I_{c2}$ is kept open. Equation (2.29) shows that, up to an additive constant, the free energy of the two-junction device is identical to that of an effective single-junction device with an effective $I_c$, which is given by

$$I_c = \sqrt{(I_{c1} + I_{c2})^2 \cos^2\delta + (I_{c1} - I_{c2})^2 \sin^2\delta}. \tag{2.30}$$

Thus, we may determine the resistance of the two-junction device by applying the well-known results for a single junction, established by Ivanchenko and Zil'berman [3, 4] and by Ambegaokar and Halperin [5]:

$$R = R_n \frac{2(1-x^2)^{1/2}}{x} \exp\left(-\gamma(\sqrt{1-x^2} + x\sin^{-1}x)\right) \sinh(\pi\gamma x/2), \tag{2.31a}$$

$$x \equiv I/I_c, \qquad\qquad \gamma \equiv \hbar I_c/e k_B T, \tag{2.31b}$$

where $R_n$ is the normal-state resistance of the two-junction device. This formula for $R$ holds when the free-energy barrier is much larger than $k_B T$, so that the barriers for phase slips are high. References [3, 4, 5] provide details on how to calculate the resistance in the general case of an over damped junction, which includes that of shallow barriers (also, see appendix B for a listing of useful results). Figure 2.7 shows the fits to the resistance, computed using Eqs. (2.30, 2.31), as a function of temperature, magnetic field, and total current for sample 219-4. Observe that both the field- and the temperature-dependence are in good agreement with experimental data. In Section 2.5.2 we make more precise contact between theory and experiment, and explain how the data have been fitted. We also note that, as it should, our Josephson junction model exactly coincides with our extension of the LAMH model in the limit of very short wires and for temperatures for which the barrier-crossing approximation is valid.

### 2.4.2 Longer nanowires: LAMH regime

In this section we describe an extension of the LAMH model of resistive fluctuations in a single narrow wire [6, 7], which we shall use to make a quantitative estimate of the voltage across the two-wire device at a fixed total current. In this regime the nanowires are sufficiently long that they behave as LAMH wires. We shall only dwell on two-wire systems, but we note in passing that the model can straightforwardly be extended to more complicated sets of lead interconnections, including periodic, grating-like arrays (see Appendix 2.6).

As the sample is not simply connected, i.e., there is a hole inside the AB contour, it is possible that there are multiple metastable states that can support the total current. These states differ by the number

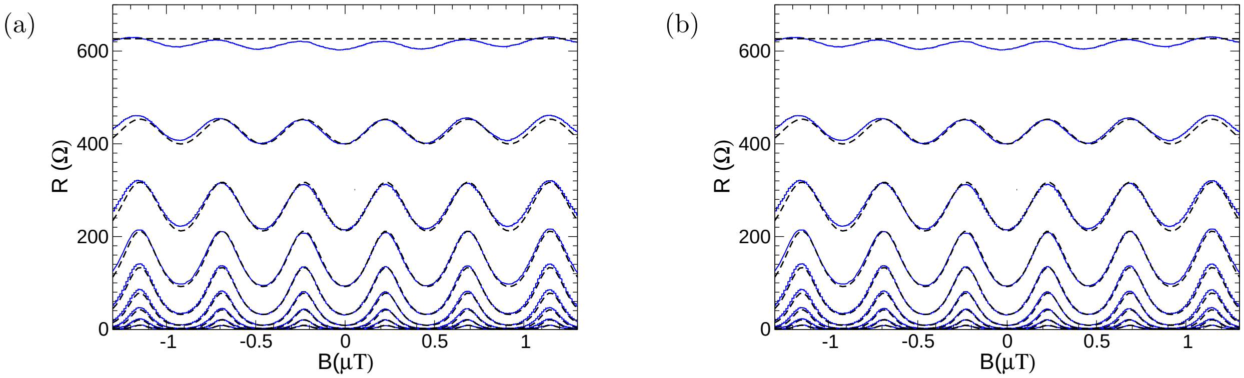

Figure 2.7: Sample 219-4: Experimental data (solid lines) and theoretical fits using the Josephson junction model (dashed lines). (a): Resistance *vs.* temperature curves. (1) Zero magnetic field and low total current. (2) Magnetic field set to maximize the resistance and low total current. (3) Zero magnetic field and 70 nA total current. (b): Resistance as a function of magnetic field at various temperatures from 1.2 to 2.0 K in 0.1 K increments. The fitting parameters used were $J_{c1} = 639\,\text{nA}$, $J_{c2} = 330\,\text{nA}$, $T_{c1} = 2.98\,\text{K}$, and $T_{c2} = 2.00\,\text{K}$, with corresponding coherence lengths $\xi_1(0) = 23\,\text{nm}$ and $\xi_2(0) = 30\,\text{nm}$. Only one set of fitting parameters [derived from curves (1) and (2)] was used to produce all the theoretical curves.

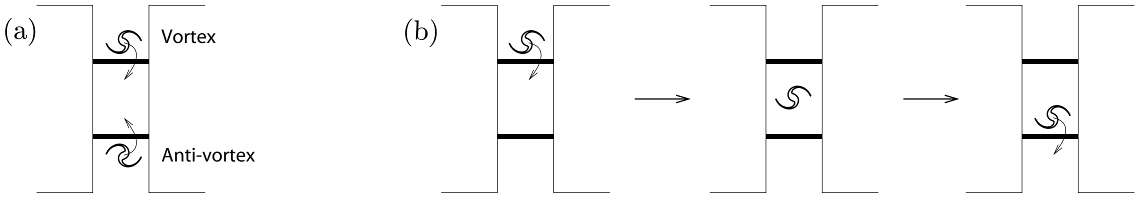

Figure 2.8: Thermally activated phase slip processes under consideration. (a) Parallel phase slips. (b) Sequential phase slips.

of times the phase winds along paths around the AB contour. The winding number $n_v$ changes whenever a vortex (or an anti-vortex) passes across one of the wires.

In the present theory, we include two kinds of processes that lead to the generation of a voltage difference between the the leads; see Fig. 2.8. In the first kind of process (Fig. 2.8a), two phase slips occur simultaneously: a vortex passes across the top wire and, concurrently, an anti-vortex passes across the bottom wire (in the opposite direction), so that the winding number remains unchanged. In the second kind of process (Fig. 2.8b), the phase slips occur sequentially: a vortex (or anti-vortex) enters the AB contour by passing across the top (or bottom) wire, stays inside the contour for some time-interval, and then leaves the AB contour through the bottom (or top) wire 2.

Our goal is to extend LAMH theory to take into account the influence of the wires on each other. In Appendix C, we review some necessary ingredients associated with the LAMH theory of a single wire. As the wires used in the experiments are relatively short (i.e. 10 to 20 zero-temperature coherence lengths in length), we also take care to correctly treat the wires as being of finite length.

Recall that we are considering experiments performed at a fixed total current, and accordingly, in all configurations of the order parameter this current must be shared between the top and bottom wires. We shall refer to this sharing,

$$I = I_1 + I_2, \tag{2.32}$$

as the *total current constraint*. Let us begin by considering a phase-slip event in a device with an isolated wire. While the order parameter in that wire pinches down, the end-to-end phase accumulation must adjust to maintain the prescribed value of the current through the wire. Now consider the two-wire device, and consider a phase slip event in one of the wires. As in the single-wire case, the phase accumulation will adjust, but in so doing it will alter the current flowing through other wire. Thus, in the saddle-point configuration of the two-wire system the current splitting will differ from that in the locally stable initial (and final) state.

Taking into account the two kinds of phase-slip processes, and imposing the appropriate constraints (i.e. the total current constraint and the phase constraint), we construct the possible metastable and saddle-point configurations of the order parameter in the two-wire system. Finally, we compute the relevant rates of thermally activated transitions between these metastable states, construct a Markov chain [45], and determine the steady-state populations of these states. Thus, we are able to evaluate the time-average of the voltage generated between the leads at fixed current due to these various dissipative fluctuations. We mention that we have not allowed for wires of distinct length or constitution (so that the Ginzburg-Landau parameters describing them are taken to be identical). This is done solely to simplify the analysis; extensions to more general cases would be straightforward but tedious.

### Parallel pair of nanowires

The total Gibbs free energy for the two-wire system is given by

$$G(I) = F_1(\theta_1) + F_2(\theta_2) - 4\mathcal{E}\Theta \cdot (J_1 + J_2). \tag{2.33}$$

Here, we have followed MH by rewriting the current-phase term in terms of dimensionless currents in wires $i = 1, 2$, i.e., $J_i$ defined via $I_i = 8\pi c J_i \mathcal{E}/\Phi_0$. Moreover, $\mathcal{E} \equiv \frac{H_c^2 \xi \sigma}{8\pi}$ is the condensate energy density per unit length of wire, and $F_i(\theta_i)$ is the Helmholtz free energy for a single wire along which there is a total phase accumulation of $\theta_i$. The precise form of $F_i(\theta_i)$ depends on whether the wire is in a metastable or saddle-point state.

We are concerned with making stationary the total Gibbs free energy at specified total current $I$, subject to the phase constraint, Eq. (2.2). This can be accomplished by making stationary the Helmholtz free energy on each wire, subject to both the total current constraint and the phase constraint, but allowing $\theta_1$ and $\theta_2$

to vary so as to satisfy these constraints—in effect, adopting the total current $I$ as the independent variable. The stationary points of the Helmholtz free energy for a single wire are reviewed in Appendix C as implicit functions of $\theta_i$, i.e., the end-to-end phase accumulation along the wire. The explicit variable used there is $J_i$, which is related to $\theta_i$ via Eq. (C.21).

### Analytical treatment in the limit of long nanowires

In the long-wire limit, we can compute the resistance analytically by making use of the single-wire free energy and end-to-end phase accumulation derived by Langer and Ambegaokar [6] (and extended by McCumber [30] for the case of the constant-current ensemble). Throughout the present subsection we shall be making an expansion in powers of $1/b$, where $b$ is the length of the wire measured in units of the coherence length, keeping terms only to first order in $1/b$. Thus, one arrives at formulæ for the end-to-end phase accumulations and Helmholtz free energies for single-wire metastable (m) and saddle-point (sp) states [30]:

$$\theta_{\mathrm{m}}(\kappa) = \kappa b, \tag{2.34a}$$

$$\theta_{\mathrm{sp}}(\kappa) = \kappa b + 2\tan^{-1}\left(\frac{1-3\kappa^2}{2\kappa^2}\right)^{1/2}, \tag{2.34b}$$

$$F_{\mathrm{m}}(\kappa) = -\mathcal{E}\left(b(1-\kappa^2)^2\right), \tag{2.34c}$$

$$F_{\mathrm{sp}}(\kappa) = -\mathcal{E}\left(b(1-\kappa^2)^2 - \frac{8\sqrt{2}}{3}\sqrt{1-3\kappa^2}\right), \tag{2.34d}$$

where $\kappa$ is defined via $J_i = \kappa_i(1-\kappa_i^2)$. In the small-current limit, one can make the further simplification that $J_i \approx \kappa_i$; henceforth we shall keep terms only up to first order in $\kappa$. To this order, the phase difference along a wire in a saddle-point state becomes

$$\theta_{\mathrm{sp}} = \kappa b + \pi - 2\sqrt{2}\kappa. \tag{2.35}$$

Next, we make use of these single-wire LAMH results to find the metastable and saddle-point states of the two-wire system, and use them to compute the corresponding barrier heights and, hence, transition rates. At low temperatures, it is reasonable to expect that only the lowest few metastable states will be appreciably occupied. These metastable states, as well as the saddle-point states between them, correspond to pairs, $\kappa_1$ and $\kappa_2$, one for each wire, that satisfy the total current constraint as well as the phase constraint:

$$\kappa_1 + \kappa_2 = J, \tag{2.36}$$

$$\theta_1(\kappa_1) - \theta_2(\kappa_2) = 2\pi n_v + 2\delta, \tag{2.37}$$

where we need to substitute the appropriate $\theta_{\mathrm{m/sp}}(\kappa_i)$ from Eqs. (2.34a, 2.35) for $\theta_i(\kappa_i)$.

In the absence of a magnetic field (i.e. $\delta = 0$), the lowest energy state is the one with no circulating current, and the current split evenly between the two wires. This corresponds to the solution of Eqs. (2.36, 2.37) with $n = 0$, together with the substitution (2.34a) for $\theta_i(\kappa_i)$ for both wires (i.e. $\theta_1 = \kappa_1 b$ and $\theta_2 = \kappa_2 b$). Thus we arrive at the solution:

$$\kappa_1 = J/2, \qquad \theta_1 = bJ/2, \tag{2.38a}$$

$$\kappa_2 = J/2, \qquad \theta_2 = bJ/2. \tag{2.38b}$$

If we ignore the lowest (excited) metastable states then only a parallel phase-slip process is allowed. The saddle point for a parallel phase slip corresponds to a solution of Eqs. (2.36, 2.37) with $n = 0$ and the substitution (2.35) for $\theta_i(\kappa_i)$ for both wires:

$$\kappa_1 = J/2, \qquad \theta_1 = bJ/2 + \pi - 2\sqrt{2}J/2, \tag{2.39a}$$

$$\kappa_2 = J/2, \qquad \theta_2 = bJ/2 + \pi - 2\sqrt{2}J/2. \tag{2.39b}$$

The change in the phase difference across the center of the trench, $\Delta\Theta \equiv [\Theta_{\mathrm{sp}} - \Theta_{\mathrm{m}}]$, is $\pi - 2\sqrt{2}\kappa$ for a forward phase slip, and $-\pi - 2\sqrt{2}\kappa$ for a reverse phase slip. The Gibbs free-energy barrier for the two kinds of phase slips, computed by subtracting the Gibbs free energy for the ground state from that of the saddle-point state, is

$$\Delta G = \mathcal{E}\left(\frac{16\sqrt{2}}{3} \pm 4J\pi\right). \tag{2.40}$$

The former free-energy is obtained by substituting Eq. (2.34c) into Eq. (2.33) for both wires; the latter one is obtained by substituting Eq. (2.34d) into Eq. (2.33) for both wires. We note that the Gibbs free-energy barrier heights for parallel phase slips (in both the forward and reverse directions) are just double those of the LAMH result for a single wire. From the barrier heights, we can work out the generated voltage by appealing to the Josephson relation, $V = (\hbar/2e)\dot{\Theta}$, and to the fact that each phase slip corresponds to the addition (or subtraction) of $2\pi$ to the phase. Hence, we arrive at the current-voltage relation associated with

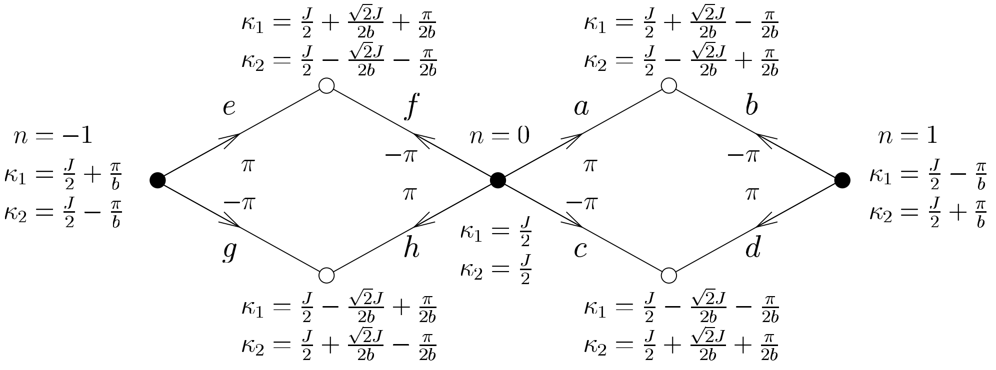

| edge | $\Delta\Theta$ | $\Delta F/\mathcal{E}$ | $\Delta G/\mathcal{E}$ | phase |
|---|---|---|---|---|
| $a$ | $-\frac{\sqrt{2}J}{2} + \frac{\pi}{2}$ | $\frac{8\sqrt{2}}{3} + \frac{\pi^2}{b}$ | $\frac{8\sqrt{2}}{3} + \frac{\pi^2}{b} - \frac{4\pi J}{2}$ | $\pi$ |
| $b$ | $-\frac{\sqrt{2}J}{2} - \frac{\pi}{2}$ | $\frac{8\sqrt{2}}{3}$ | $\frac{8\sqrt{2}}{3} + \frac{4\pi J}{2}$ | $-\pi$ |
| $c$ | $-\frac{\sqrt{2}J}{2} - \frac{\pi}{2}$ | $\frac{8\sqrt{2}}{3} + \frac{\pi^2}{b}$ | $\frac{8\sqrt{2}}{3} + \frac{\pi^2}{b} + \frac{4\pi J}{2}$ | $-\pi$ |
| $d$ | $-\frac{\sqrt{2}J}{2} + \frac{\pi}{2}$ | $\frac{8\sqrt{2}}{3}$ | $\frac{8\sqrt{2}}{3} - \frac{4\pi J}{2}$ | $\pi$ |
| $e$ | $-\frac{\sqrt{2}J}{2} + \frac{\pi}{2}$ | $\frac{8\sqrt{2}}{3}$ | $\frac{8\sqrt{2}}{3} - \frac{4\pi J}{2}$ | $\pi$ |
| $f$ | $-\frac{\sqrt{2}J}{2} - \frac{\pi}{2}$ | $\frac{8\sqrt{2}}{3} + \frac{\pi^2}{b}$ | $\frac{8\sqrt{2}}{3} + \frac{\pi^2}{b} + \frac{4\pi J}{2}$ | $-\pi$ |
| $g$ | $-\frac{\sqrt{2}J}{2} - \frac{\pi}{2}$ | $\frac{8\sqrt{2}}{3}$ | $\frac{8\sqrt{2}}{3} + \frac{4\pi J}{2}$ | $-\pi$ |
| $h$ | $-\frac{\sqrt{2}J}{2} + \frac{\pi}{2}$ | $\frac{8\sqrt{2}}{3} + \frac{\pi^2}{b}$ | $\frac{8\sqrt{2}}{3} + \frac{\pi^2}{b} - \frac{4\pi J}{2}$ | $\pi$ |

Figure 2.9: Diagram representing the ground state (central filled circle), the two lowest-energy metastable states (left and right filled circles), and the saddle-point states connecting them (open circles) for the case of magnetoresistance minimum (i.e. $\delta = 0, \pi, \ldots$). The saddle-point states at the top of the graph correspond to phase slips in the top wire (i.e. wire 1); those at the bottom correspond to the bottom wire (i.e. wire 2). (Saddle-point states for parallel phase slips are not shown.) For each state $\kappa_1$ and $\kappa_2$ are listed. For each barrier (represented by an edge and labeled by $a$ through $h$), the table at the right lists the gain in phase across the trench, the gain in Helmholtz free energy, the barrier height (i.e. the gain in Gibbs free energy), and the amount of phase that would effectively be generated at the end of the phase slip event (i.e. upon completion of a closed loop, the amount of phase generated is the sum of the effective phases).

parallel phase slips at $\delta = 0$:

$$V_{\delta=0\,,\ \mathrm{par}} = \frac{\hbar}{e}\,\Omega\, e^{-\beta\mathcal{E}\frac{16\sqrt{2}}{3}} \sinh\left(I/I_0\right), \tag{2.41}$$

where the prefactor $\Omega$ may be computed using time-dependent Ginzburg-Landau theory or extracted from experiment, and $I_0 = 4e/\beta h$.

If we take into account the two lowest excited states, which we ignored earlier, then voltage can also be generated via sequential phase slips (in addition to the parallel ones, treated above). To tackle this case, we construct a diagram in which the vertices represent the metastable and saddle-point solutions of Eqs. (2.36, 2.37), and the edges represent the corresponding free energy barriers; see Fig. 2.9. Pairs of metastable-state vertices are connected via two saddle-point-state vertices, corresponding to a phase slip on either the top or the bottom wire. To go from one metastable state to another, the system must follow the edge out of the starting metastable state leading to the desired saddle-point state. We assume that, once the saddle-point state is reached, the top of the barrier has been passed and the order parameter relaxes to the target metastable state. (To make the graph more legible, we have omitted drawing the edge that corresponds to this relaxation process.) To find the Gibbs free-energy difference between a metastable state and a saddle-point state, we need to know the phase difference across the center of the trench. To resolve the ambiguity of $2\pi$ in the definition of $\Theta$, the phase difference can be found by following the wire with no phase slip. To further improve the legibility of Fig. 2.9, the free-energy barriers are listed in a separate table to the right. Note, that a phase slip on just one of the wires, being only half of the complete process, can be regarded to a gain in phase of $\pm\pi$ for the purposes of calculating voltage, as indicated in both the graph and the table.

Once the table of barrier heights has been computed, we can construct a Markov chain on a directed graph, where the metastable states are the vertices—in effect, an explicit version of our diagram. In general, each pair of neighboring metastable states, $s_n$ and $s_{n+1}$, are connected by four directed edges:

$$s_n \xrightarrow[\text{top}]{} s_{n+1} \qquad\qquad s_n \xrightarrow[\text{bottom}]{} s_{n+1} \tag{2.42a}$$

$$s_n \xleftarrow[\text{top}]{} s_{n+1} \qquad\qquad s_n \xleftarrow[\text{bottom}]{} s_{n+1} \tag{2.42b}$$

where the probability to pass along a particular edge is given by $P(\cdot) = \exp -\beta\Delta G_{(\cdot)}$, in which $\Delta G_{(\cdot)}$ may be read off from the table in Fig. 2.9.

We denote the occupation probability of the $n^{\text{th}}$ metastable state by $o_n$, where $n$ corresponds to the $n$ in the phase constraint (2.2). $o_n$ may be computed in the standard way, by diagonalizing the matrix representing the Markov chain [45]. Each move in the Markov chain can be associated with a gain in phase across the device of $\pm\pi$, as specified in Fig. 2.9. Thus, we may compute the rate of phase-gain, and hence the voltage:

$$V = \frac{\Omega\hbar}{4e}\sum_{\langle nm\rangle}\frac{o_n}{g_{n,m}}\big(P(s_n \xrightarrow[\text{top}]{} s_m) - P(s_n \xrightarrow[\text{bot}]{} s_m)\big), \tag{2.43}$$

where the rate prefactor $\Omega$ is to be determined, $\langle nm\rangle$ indicates that the sum runs over neighboring states only, and $g_{n,m}$ keeps track of the sign of the phase-gain for reverse phase-slips:

$$g_{n,m} = \begin{cases} 1, & \text{if } m > n, \\ -1, & \text{if } m < n. \end{cases} \tag{2.44}$$

For the case $\delta = 0$, and keeping the bottom three states only, the voltage generated via sequential phase

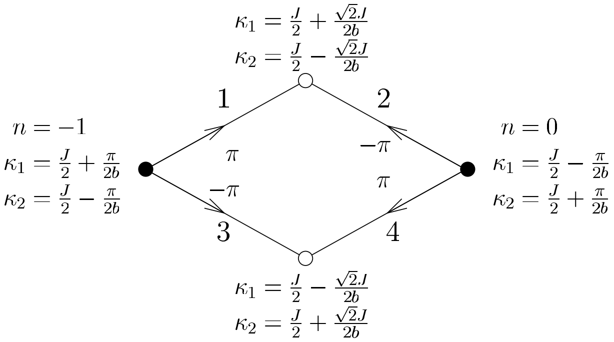

| edge | $\Delta\Theta$ | $\Delta F/\mathcal{E}$ | $\Delta G/\mathcal{E}$ | phase |
|---|---|---|---|---|
| 1 | $-\frac{\sqrt{2}J}{2} + \frac{\pi}{2}$ | $\frac{8\sqrt{2}}{3} - \frac{\pi^2}{b}$ | $\frac{8\sqrt{2}}{3} - \frac{\pi^2}{b} - \frac{4\pi J}{2}$ | $\pi$ |
| 2 | $-\frac{\sqrt{2}J}{2} - \frac{\pi}{2}$ | $\frac{8\sqrt{2}}{3} - \frac{\pi^2}{b}$ | $\frac{8\sqrt{2}}{3} - \frac{\pi^2}{b} + \frac{4\pi J}{2}$ | $-\pi$ |
| 3 | $-\frac{\sqrt{2}J}{2} - \frac{\pi}{2}$ | $\frac{8\sqrt{2}}{3} - \frac{\pi^2}{b}$ | $\frac{8\sqrt{2}}{3} - \frac{\pi^2}{b} + \frac{4\pi J}{2}$ | $-\pi$ |
| 4 | $-\frac{\sqrt{2}J}{2} + \frac{\pi}{2}$ | $\frac{8\sqrt{2}}{3} - \frac{\pi^2}{b}$ | $\frac{8\sqrt{2}}{3} - \frac{\pi^2}{b} - \frac{4\pi J}{2}$ | $\pi$ |

Figure 2.10: Diagram and corresponding Table for the case of magnetoresistance maxima (i.e. $\delta = \pi/2, 3\pi/2, \ldots$). See the caption to Fig. 2.9 for explanation of the diagram.

slips turns out to be

$$V_{\delta=0\,,\text{ seq}} = \frac{2\hbar}{e}\,\Omega\, e^{-\beta\mathcal{E}\left(\frac{8\sqrt{2}}{3}+\frac{\pi^2}{b}\right)} \sinh(I/2I_0). \tag{2.45}$$

Having dealt with the case of $\delta = 0$ (and hence obtained the value of the resistance at magnetic fields corresponding to resistance minima), we now turn to the case of $\delta = \pi/2$, i.e., resistance maxima.

In this half-flux quantum situation, there are two degenerate lowest-energy states, with opposite circulating currents. These states are connected by saddle-point states in which a phase-slip is occurring on either the top or bottom wire. The diagram of the degenerate ground states and the saddle-point states connecting them is shown in Fig. 2.10. By comparing the diagram with the associated Table, it is easy to see that the free-energy barriers are biased by the current, making clockwise traversals of Fig. 2.10 more probable than counter-clockwise traversals. As there are only two metastable states being considered, and as they are degenerate, it is unnecessary to go through the Markov chain calculation; clearly, the two states each have a population of 1/2. The voltage being generated by the sequential phase-slip is then given by

$$V_{\delta=\pi/2,\text{ seq}} = \frac{\hbar}{2e}\,\Omega\, e^{-\beta\mathcal{E}\left(\frac{8\sqrt{2}}{3}-\frac{\pi^2}{b}\right)} \sinh(I/2I_0). \tag{2.46}$$

$V_{\delta=\pi/2,\text{ seq}}$ is larger than the sum of $V_{\delta=0,\text{ seq}}$ and $V_{\delta=0,\text{ par}}$, so, as expected, the resistance is highest at magnetic fields corresponding to $\delta = \pi/2$. For very long wires, the perturbation of one wire when a phase slip occurs in the other is very small, and therefore we expect that the dependence of resistance on magnetic field will decrease with wire length. Indeed, for very long wires, the difference in barrier heights to sequential phase slips between the $\delta = 0$ and $\delta = \pi/2$ cases disappears (i.e. Eq. (2.45) and Eq. (2.46) agree when $b \gg 1$).

### Numerical treatment for intermediate-length nanowires

Instead of using the long-wire approximation, Eqs. (2.34a-2.34d), we can use the exact functions for the end-to-end phase accumulation along a wire $\theta(J(\kappa))$, and the Helmholtz free energy $F_{\mathrm{m/sp}}(J(\kappa))$. By dropping the long-wire approximation, as the temperature approaches $T_{\mathrm{c}}$ and the coherence length decreases the picture correctly passes to the Josephson limit. In this approach, the total current and the phase constraints must be solved numerically, as $\theta(J(\kappa))$ is a relatively complicated function. Figure 2.12 provides an illustration of how, for a single wire, the function $J(\theta)$ depends on its length. We shall, however, continue to use the barrier-crossing approximation. Because the barriers get shallower near $T_{\mathrm{c}}$, our results will become unreliable (and, indeed, incorrect) there.

The form of the order parameter that satisfies the Ginzburg-Landau equation inside the wire is expressed in Eqs. (C.20b, C.6). Therefore, to construct the functions $\theta(J)$ and $F_{\mathrm{m/sp}}(J)$ [i.e. Eqs. (C.21, C.22)], we need to find $u_0(J)$, i.e., the squared amplitude of the order parameter in the middle of the wire. Hence, we need to ascertain suitable boundary conditions obeyed by the order parameter at the ends of the wire. For thin wires, a reasonable hypothesis is that the amplitude of the order parameter at the ends of the wire matches the amplitude in the leads:

$$f(z = \pm b/2)^2 = \frac{H^2_{\mathrm{c\ film}}(T)\, \xi^2_{\mathrm{film}}(T)}{H^2_{\mathrm{c\ wire}}(T)\, \xi^2_{\mathrm{wire}}(T)}. \tag{2.47}$$

For wires made out of superconducting material the same as (or weaker than) the leads, this ratio is always larger than unity [5] .

Once we have computed the functions $\theta(J)$ and $F_{\mathrm{m/sp}}(J)$ for both saddle-point and metastable states on a single wire, we can use the phase and total current constraints to build the saddle-point and metastable states for the two-wire device. We proceed as before, by constructing a Markov chain for the state of the device, except that now we include in the graph all metastable states of the device. By diagonalizing the Markov chain, we find the populations of the various metastable states and, hence, the rate of gain of $\Theta$.

---

[5] In finding $u_0$ there is a minor numerical difficulty. As the amplitude of the order parameter is expressed via the JacobiSn function, and JacobiSn$[z\sqrt{u_2/2}, u_1/u_2]$ is a doubly periodic function in the first variable, it is not obvious whether $\pm(b/2)\sqrt{u_2/2}$ lies in the first period, as can be seen from Fig. 2.11. As the trajectory must be simply periodic, $z\sqrt{u_2/2}$ must intersect either a zero or a pole in the first unit quarter cell of the JacobiSn function. Now, we are only interested in trajectories that escape to $f \to \infty$ [as $f(\pm b/2)$ is assumed to be greater than or equal to unity], so a pole must be intersected. (However, being outside the first period is unphysical, as it means that somewhere along the wire $f = \infty$.) There are exactly two poles in the first unit quarter cell. They are located at $2v_1 + v_2$ and $v_2$, where $v_1 \equiv \mathrm{K}(u_1/u_2)$ and $v_2 \equiv i\mathrm{K}(1 - u_1/u_2)$, in which $\mathrm{K}(\cdot)$ is the complete elliptic integral. So, instead of checking whether $\pm(b/2)\sqrt{u_2/2}$ is outside the unit quarter cell, we can just determine which pole $z\sqrt{u_2/2}$ intersects and then see if $\pm(b/2)\sqrt{u_2/2}$ lies beyond that pole or not.

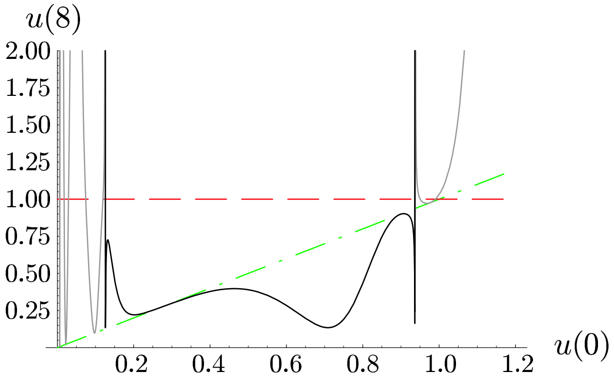

Figure 2.11: Squared amplitude $u(b/2)$ of the order parameter at the end of a wire, as a function of its value $u_0 = u(0)$ at the mid-point of the of the wire, computed using the JacobiSN function [see Eq. (C.20b)], for the case $b = 16$. The black line corresponds to trajectories that do not go through a pole; the gray line corresponds to trajectories that do pass through at least one pole. The intersection of the dashed and black lines represents those trajectories that satisfy the boundary condition $u(\pm b/2) = 1$. (The intersection of the dashed-dotted and black lines represent trajectories that start and stop at the same point, i.e., $u(b/2) = u_0$).

We plot the typical magnetoresistance curves for various temperatures, obtained numerically, as well as $dV/dI$ *vs.* $T$ for various magnetic fields and total currents. Notice that the resistance at $\delta = 0$ and large total currents can exceed that at $\delta = \pi/2$ with low total-current.

## 2.5 Connections with experiment

In this section a connection is made between our calculations and our experiments [38]. First, the predicted period of the magnetoresistance oscillations is compared to the experimentally obtained one. Then, the experimentally-obtained resistance vs. temperature curves are fitted using our extension of the IZ-AH Josephson junction model (for shorter wires) and our extension of the LAMH wire model (for longer wires).

### 2.5.1 Device fabrication

Four different devices were successfully fabricated and measured. The devices were fabricated by suspending DNA molecules across a trench and then sputter coating them with the superconducting alloy of MoGe. The leads were formed in the same sputter-coating step, ensuring seamless contact between leads and the wires. Next, the leads were truncated lithographically to the desired width. In the case of device 930-1, after being measured once, its leads were further narrowed using focused ion beam milling, and the device was remeasured. For further details of the experimental procedure see Ref. [38].

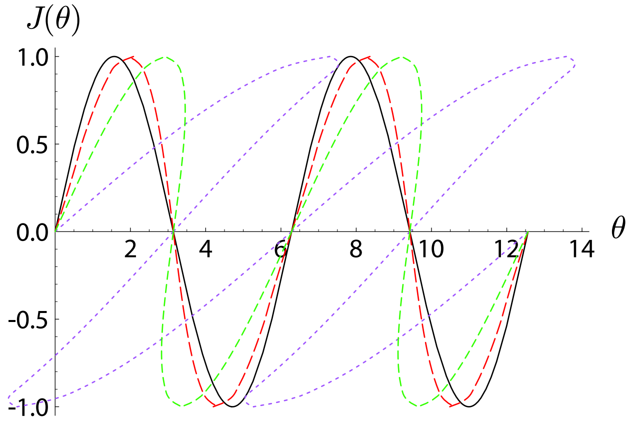

Figure 2.12: Current (in units of the critical current) vs. end-to-end phase accumulation for superconducting wires of various lengths: $0\xi$ (solid line), $1.88\xi$, $5.96\xi$, $14.4\xi$ (dotted line). The transition from LAMH to Josephson junction behavior is evident from the loss of multivaluedness of the current, as the wire length is reduced.

### 2.5.2 Comparison between theory and experiment

**Oscillation period**

The magnetoresistance periods obtained for four different samples are summarized in Table 2.1. The corresponding theoretical periods were calculated using Eq. (2.6), based on the geometry of the samples which was obtained via scanning electron microscopy. To test the theoretical model, the leads of one sample, sample 930-1, were narrowed using a focused ion beam mill, and the magnetoresistance of the sample was remeasured. The theoretically predicted periods all coincide quite well with the measured values, except for sample 219-4, which was found to have a "+" shaped notch in one of the leads (which was not accounted for in calculating the period). The notch effectively makes that lead significantly narrower, thus increasing the magnetoresistance period, and this qualitatively accounts for the discrepancy.

For all samples, when the leads are driven into the vortex state, the magnetoresistance period becomes much longer, approaching the Aharonov-Bohm value for high fields. This is consistent with the theoretical prediction that the period is then given by Eq. (2.6), but with $l$ replaced by the field-dependent inter-vortex spacing $r$.

**Oscillation amplitude**

We have made qualitative and quantitative estimates of the resistance of two-bridge devices in several limiting cases. For devices containing extremely short wires [$b \approx \xi(T)$], such as sample 219-4, the superconducting wires cannot support multiple metastable states, and thus they operate essentially in the Josephson junction

| Sample | $b$ (nm) | $2a$ (nm) | $2l$ (nm) | Theoretical period ($\mu$T) | Measured period ($\mu$T) | error |
|---|---|---|---|---|---|---|
| 205-4 | 121 | 266 | 11267 | 929.21 | 947. | 1.9% |
| 219-4 | 137 | 594 | 12062 | 388.73 | 456.6 | 12.8% |
| 930-1 | 141 | 2453 | 14480 | 78.41 | 77.5 | −1.2% |
| 930-1 (shaved) | 141 | 2453 | 8930 | 127.14 | 128.3 | 0.9% |
| 205-2 | 134 | 4046 | 14521 | 47.41 | 48.9 | 3.0% |

Table 2.1: Comparison between measured and theoretical magnetoresistance periods. The geometries of the samples were obtained via scanning electron microscopy and used to compute the periods theoretically; see the text for additional details.

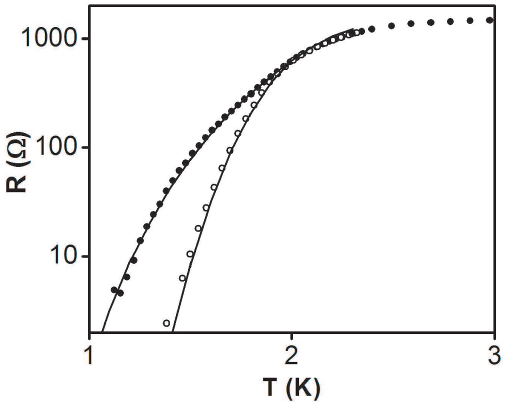

Figure 2.13: Sample 219-4: Resistance vs. temperature measurements in zero magnetic field (open circles) and at a magnetic field of 228 $\mu$T (solid circles) corresponding to a maximum change in magnetoresistance. The lines are theoretical fits, based on the short-wire (Josephson) limit of the LAMH theory, using the following fitting parameters: $J_{c1} = 639\,\text{nA}$, $J_{c2} = 330\,\text{nA}$, $T_{c1} = 2.98\,\text{K}$, and $T_{c2} = 2.00\,\text{K}$ (with corresponding coherence lengths $\xi_1(0) = 20\,\text{nm}$ and $\xi_2(0) = 26\,\text{nm}$).

limit, but with the junction critical current being a function of temperature given by LAMH theory as

$$I_c(T) = I_c(0)(1 - T/T_c)^{3/2}. \tag{2.48}$$

A summary of fits to the data for this sample, using the Josephson junction limit, is shown in Fig. 2.7. On the other hand, for longer wires it is essential to take into account the multiple metastable states, as is the case for sample 930-1, which has wires of intermediate length. A summary of numerical fits for this sample is shown in Fig. 2.14. In all cases, only the two low total-current magnetoresistance curves were fitted. By using the extracted fit parameters, the high total-current magnetoresistance curves were calculated, with their fit to the data serving as a self-consistency check. As can be seen from the fits, our model is consistent with the data over a wide range of temperatures and resistances. We remark, however, that the coherence length required to fit the data is somewhat larger than expected for MoGe.

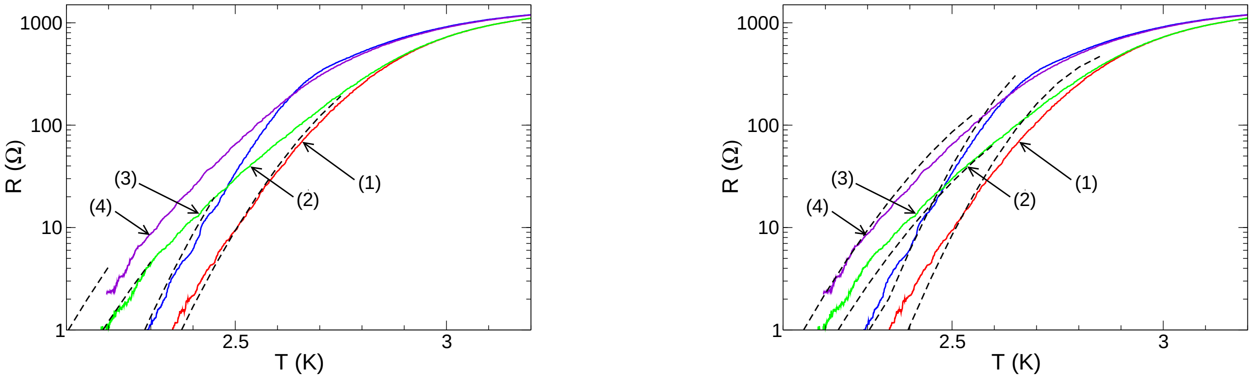

(LHS) $R_1 = 2883\,\Omega$, $R_2 = 2941.7\,\Omega$, $\xi_{01} = 17.3\,\mathrm{nA}$, $\xi_{02} = 8.7\,\mathrm{nA}$, $T_{\mathrm{c}1} = 3.147\,\mathrm{K}$, $T_{\mathrm{c}2} = 3.716\,\mathrm{K}$.
(RHS) $R_1 = 2912\,\Omega$, $R_2 = 2912\,\Omega$, $\xi_{01} = 10\,\mathrm{nA}$, $\xi_{02} = 9\,\mathrm{nA}$, $T_{\mathrm{c}1} = 3\,\mathrm{K}$, $T_{\mathrm{c}2} = 3.65\,\mathrm{K}$.

Figure 2.14: Sample 930-1: Resistance vs. temperature curves. Experimental data (full lines) and theoretical fits to the extended LAMH model in the intermediate regime (dashed lines). Theoretical curves terminate when the short-wire regime is reached, i.e., $5\xi(T) \sim b$. (1) Zero magnetic field and low total current. (2) Magnetic field set to maximize the magnetoresistance and low total current. (3) Zero magnetic field and 80 nA total current. (4) Magnetic field set to maximize the resistance and 80 nA total current. The fit on the left was optimized numerically, and the one on the right was obtained by hand, showing that a more realistic value of $\xi_{01}$ is remains reasonably consistent.

## 2.6 Multi-wire devices

In this section we give an example of how to extend the theory presented so far to the case of devices comprising more than two wires. In our example, we consider an array of $n$ identical short wires (i.e. wires in the Josephson junction limit) spaced at regular intervals. We continue to work at a fixed total current and to ignore charging effects. The end-to-end phase accumulations along the wires are related to each other as

$$\begin{aligned} \theta_2 &= \theta_1 + 2\delta, \\ \theta_3 &= \theta_1 + 4\delta, \\ &\vdots \\ \theta_n &= \theta_1 + 2(n-1)\delta, \end{aligned} \tag{2.49}$$

i.e., $\theta_n - \theta_1 = 2(n-1)\delta$ (for $n = 2, \ldots, N$), where $\delta$ is the phase accumulation in one of the leads between each pair of adjacent wires. The Gibbs free energy of the multi-wire subsystem is given by

$$G(I, \theta_1) = -\frac{h}{2e}\left(I_{\mathrm{c}} \sum_{m=1}^{n} \cos\big(\theta_1 + 2(m-1)\delta\big) + I\theta_1\right), \tag{2.50}$$

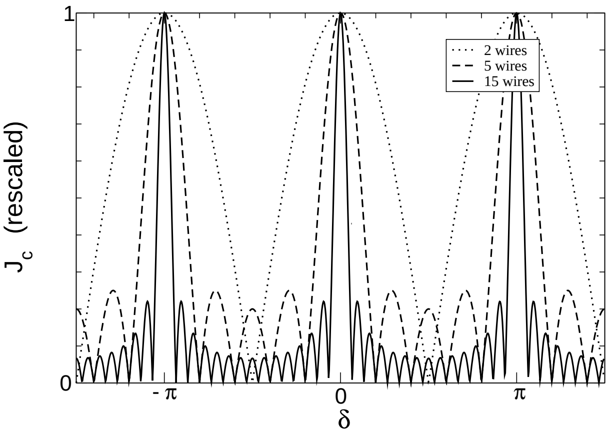

Figure 2.15: Effective single junction critical current for a multi-junction array, as a function of $\delta$. The critical current has been rescaled so that $J_c(\delta = 0) = 1$. Note the similarity with a multi-slit interference pattern.

where $I$ is the total current and we are assuming that the wires have identical critical currents. As for the two-junction case, this junction array, is equivalent to a single effective junction. Figure 2.15 shows the critical current of this effective junction as a function of $\delta$ for devices comprising 2, 5, and 15 wires. The magnetoresistance of such a device then follows from IZ-AH theory, i.e., Eq. (2.31).

## 2.7 Cross currents and applications

In addition to creating phase gradients by applying a magnetic field, phase gradients may be created directly by passing a "cross-current," i.e. the current in one of the leads that is passed perpendicular to the wires. This setup was studied by Jaklevic, Lambe, and Silver in their original paper on SQUIDs [46]. In this section, we demonstrate a molecular-scale version of the Jaklevic et al. phase-sensing experiment, in which DNA-templated superconducting nanowires are used instead of Josephson junctions to make a nanowire version of a superconducting quantum interference device (i.e. an N-SQUID). Micro- and nano-scale realizations of SQUIDs have been fabricated, e.g., in the shunted Nb nanojunctions and a sub-micron hole [47], and more recently using nanotubes [48]. They have also been used to study a range of quantum coherent settings, such as phase qubits [49] and magnetization tunneling [50, 51].

To enable the passing of a cross-current, we have modified on of the leads by cutting it, using a focused ion beam (FIB) mill, into a horseshoe shape as depicted in Fig. 2.16. Thus we define a narrow strip through which a cross-current ($I_X$) can be applied. Independently, a bias current ($I_B$) can be applied through the wires, via which the lead-to-lead resistance is measured [52]. We note that the width of the cross current strip $w = 633\,\text{nm}$ is much smaller than the estimated zero temperature magnetic field penetration depth

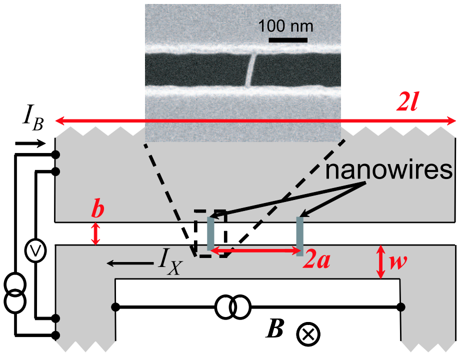

Figure 2.16: Schematic of the DNA-templated two-nanowire device for cross-current measurements. The bias-current $I_{\mathrm{B}}$ is applied through the nanowires, and the cross-current $I_{\mathrm{X}}$ is applied through the $MoGe$ horseshoe lead, passing the contact points of the wires. The magnetic field $B$ is applied perpendicular to the plane of the leads and wires. One of the two metal-coated DNA molecules is shown on the SEM micrograph.

$\lambda_{\perp} = 46\,\mu$m. The sputtered thickness $d$ of the film is about $d = 10.5\,$nm. Thus the analyses of the results will be carried out under the assumption that the cross current flows uniformly in the cross-current strip. Also, the width of the big lead, $2l = 17.33\,\mu$m is smaller than $\lambda_{\perp}$, and thus any external magnetic field will penetrate both leads without significant attenuation. Furthermore, the effects of the magnetic field generated by the cross current are not significant. The length of the wires was $b = 100\,$nm, and the distance between them, which determines the spatial resolution of the device, $2a = 6.13\,\mu$m. We note that devices with a much smaller separation between the wires (e.g. sample 205-4 in Table 2.1 has $2a = 266\,$nm) and thus with a better spatial resolution, can be fabricated if desired..

Our main accomplishments are as follows. (1) By measuring the period of the resistance oscillations driven by an externally injected supercurrent we have obtained a direct, local measure of the superfluid density and its dependence on temperature in the vortex-free regime. Our results cannot be consistently described by the phenomenological Gorter-Casimir and Ginzburg-Landau theories. However, we do find good agreement with Miller's dirty limit of the microscopic BCS theory [53], which was previously examined for MoGe via a distinct method by the Lemberger group [54]. (2) We have also observed and investigated the amplification of the current-induced phase gradient that occurs when pinned vortices are present in the cross-current-carrying lead. This amplification is brought about by the Lorentz force acting on randomly pinned vortices, which results in their reversible displacement. In macroscopic settings, this physical phenomenon is the origin of the Campbell law, i.e. the dependence of magnetic field penetration depth on the concentration of vortices [55, 56, 57, 58]. Our measurements provide verification of the physics behind the Campbell law, but now at the microscale, as well as the capability of obtaining the Labusch parameter, i.e. the average stiffness of the vortex pinning potential.

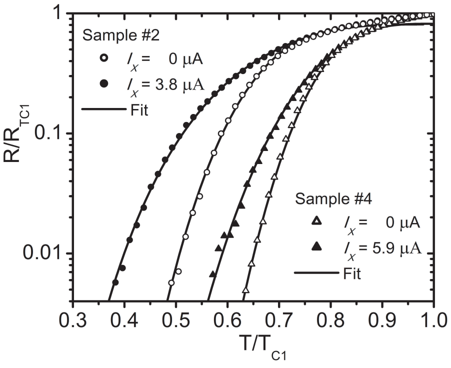

Figure 2.17: Resistance vs. temperature data for samples #2 (circles) and #4 (triangles). The open shapes correspond to zero cross-current measurements and the closed shapes correspond to a cross-current that gives resistance close to a maximum (3.8 $\mu$A for sample #2 and 5.9 $\mu$A for sample #4). The fits are obtained with the following fit parameters:
sample #2 – $R_\mathrm{N} = 800\,\Omega$, $I_\mathrm{c1}(0) = 376\,\mathrm{nA}$, $I_\mathrm{c2}(0) = 151\,\mathrm{nA}$, $T_\mathrm{c1} = 2.45\,\mathrm{K}$, $T_\mathrm{c2} = 1.86\,\mathrm{K}$; and
sample #4 – $R_\mathrm{N} = 700\,\Omega$, $I_\mathrm{c1}(0) = 1066\,\mathrm{nA}$, $I_\mathrm{c2}(0) = 317\,\mathrm{nA}$, $T_\mathrm{c1} = 3.04\,\mathrm{K}$, $T_\mathrm{c2} = 2.55\,\mathrm{K}$

### 2.7.1 Cross current measurements with no magnetic field

At $I_\mathrm{X} = 0$ we observe a broad resistive transition in the wires, as the temperature is decreased. Moreover, as $I_\mathrm{X}$ is increased, this transition periodically broadens and narrows back to its $I_\mathrm{X} = 0$ breadth. In Fig. 2.17 we show this transition for two samples, each measured at two distinct values of $I_\mathrm{X}$ that correspond almost exactly to the minimum and maximum observed breadths. This effect is very similar to the one observed as the magnetic field is varied as described in sections 2.2 and 2.3. Except in this case the phase gradients are caused by the injected supercurrent as opposed to screening currents induced by the magnetic field. The temperature dependence of the resistance, as before, follows the theory of thermally activated phase slips (TAPS) [29, 6, 7], extended to the two-wire case, see section 2.4. This extended two-wire-TAPS theory involves a modified free-energy barrier for phase slips which accounts for the inter-wire coupling mediated through the leads. In the short-wire limit [6], for which the phase slips must occur simultaneously in both wires, the two-wire device has the current-phase relation of a single Josephson junction with an effective critical current

$$I_\mathrm{eff} = \frac{\sqrt{6}}{2}\frac{\hbar}{2e}\sqrt{(I_\mathrm{c1}+I_\mathrm{c2})^2\cos^2\frac{\delta}{2} + (I_\mathrm{c1}-I_\mathrm{c2})^2\sin^2\frac{\delta}{2}}, \tag{2.51}$$

---

[6] The short-wire limit applies when the current-phase relation for each wire must be single valued. Our estimations show that the processes in which single valuedness is violated are thermodynamically not significant, so even if they are included in the calculation the fits to the $R(T)$ curves will not change significantly. Furthermore, the period, which is the main focus of our manuscript, is independent of whether the wires are operating in the short wire limit or not.

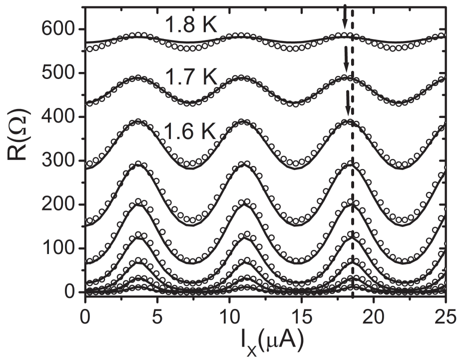

Figure 2.18: Resistance vs. cross-current data for sample #2 at temperatures ranging from 1.0 K to 1.8 K in 0.1 K increments. The solid lines are fits using the same wire parameters as the fit for the $R-T$ data in Fig. 2.17 and for the period vs. $T$ data in Fig. 2.19. The dashed vertical line corresponds to the position of the peak at 1 K, and is an aid to see the decrease in period at higher temperatures. The arrows point to peaks, and demonstrates the change in the period of oscillation at with temperature.

tuned by the phase gain between the ends of the two wires $\delta$ (see Fig. 2.16). For the case of cross-current experiment, $\delta = \int_{-a}^{a} \nabla\phi \cdot dr$ where the integral runs between the wire ends via the horseshoe lead. Moreover, $I_{\mathrm{c}1}$ and $I_{\mathrm{c}2}$ are the critical currents for the wires, given by $I_{\mathrm{c}1,2} = I_{\mathrm{c}1,2}(0)[1 - T/T_{\mathrm{c}1,2}]^{3/2}$ [59]. We obtain the device resistance $R$ from the damped Josephson junction formula [3, 5] (Eq. (9) in Ref. [5]), where we have used the normal-state resistance $R_{\mathrm{N}}$ of the two parallel wires for the effective shunt resistance of the junction. Choosing $\delta = 0$ and $\delta = \pi$ we fit the lower and upper curves in Fig. 2.17.

As shown in Fig. 2.18, the resistance oscillates as a function of the cross-current $I_{\mathrm{X}}$, having a period on the order of $7\,\mu$A and an amplitude that is strongly temperature dependent and maximal at temperatures near the middle of the resistive transition. As the arrows in Fig. 2.18 indicate, the period of the resistance oscillation is temperature-dependent, in contrast with the case of magnetic-field-induced oscillations, which appear to be temperature independent.

The period of the resistance oscillation is determined by the condition that the phase gain $\delta$ be $2\pi\, n$, where $n$ is an integer [7]. For the case of a uniform cross current in a thin-film strip of width $w$ and thickness $d$, $\nabla\phi$ is related to $I_{\mathrm{X}}$ through the superfluid density $n_{\mathrm{s}}$: $\nabla\phi = \delta/2a = (I_{\mathrm{X}}/n_{\mathrm{s}})(2m/wde\hbar)$, where $m$ and $e$ are the electronic mass and charge. Thus, by measuring the period of the resistance oscillation as a function of the temperature $T$, we obtain the superfluid density in the strip carrying the cross-current, through the

---

[7] We estimate that the sensitivity of the present setup in measuring the phase difference is roughly 0.3 % of a single period (which is $2\pi$) per Hz$^{1/2}$. The sensitivity can be further improved by optimizing the current bias used for the resistance measurements. In the present experiments we used quite low bias current of $\sim 10$ nA.

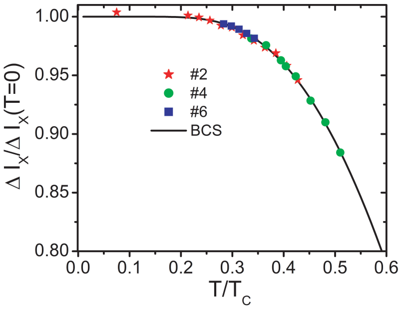

Figure 2.19: Cross-current period in the resistance oscillation vs. temperature data for all three samples. The lowest temperature measurement for sample #2 was measuring using switching current vs. cross current. The line shows the BCS relation for superfluid fraction as a function of temperature for a dirty superconductor (Eq. 2.53). The data for the three samples have been linearly re-scaled to obtain the best fit. The lowest temperature point for sample #2 was obtained from cross-current vs. switching current data. The scaling parameters used were the period at $T = 0\,\mathrm{K}$, and the $T_\mathrm{c}$ of the thin film strip, and are as follows: sample #2 7.44 $\mu$A, 5.23 K; sample #4 11.43 $\mu$A, 5.94 K; and sample #6 7.28 $\mu$A, 5.56 K.

relation:

$$\Delta I_\mathrm{X}(T) = \left(\frac{\pi w d}{a}\frac{\hbar e}{2m}\right) n_\mathrm{s} = \Delta I_\mathrm{X}(0)\frac{n_\mathrm{s}(T)}{n_\mathrm{s}(0)}. \tag{2.52}$$

The normalized period of the resistance oscillation (hence, the normalized superfulid density), as a function of temperature, is shown in Fig. 2.19. To make the fits we have used Miller's result, applicable to the dirty superconductor case [53],

$$n_\mathrm{s}(T) = n_\mathrm{s}(0)\frac{\Delta(T/T_\mathrm{c})}{\Delta(0)}\tanh\left[\frac{\Delta(T/T_\mathrm{c})}{2k_\mathrm{B}T}\right], \tag{2.53}$$

where $T_\mathrm{c}$ is the critical temperature, $n_\mathrm{s}(0)$ is the zero-temperature superfluid density, and $\Delta(T/T_\mathrm{c})$ is the universal BCS relation [34]. The fit by Miller's formula, shown in Fig. 2.19, was performed by allowing $n_s(0)$ (and hence, $\Delta I_\mathrm{X}(0)$) as well as $T_c$ to be adjustable scaling parameters. It gives superior agreement than the alternative theories, such as that of Gorter-Casimir and Ginzburg-Landau, which can be made to fit well but with $T_c$ well outside the expected range as compared to a direct measurement. The values of $T_\mathrm{c}$ obtained from the fit to Miller's formula, 5.2-5.9 K, agree with those measured for the films, in the range of 5.6-5.8 K. Combining the fitting parameters extracted from Fig. 2.17 [namely, $I_{\mathrm{c}1}$, $T_{\mathrm{c}1}$, $I_{\mathrm{c}2}$, $T_{\mathrm{c}2}$] and Fig. 2.19 [namely, the film $T_\mathrm{c}$ and $\Delta I_\mathrm{X}(0)$], we produce the theoretical curves in Fig. 2.18 without any additional adjustable parameters. The fits agree well with the data [8].

---

[8] We note that the disorder and the electron-electron interaction effects, responsible for the suppression of $T_c$ in the the film leads, are known to be even stronger in the nanowires. See, e.g., J. M. Graybeal et al., Phys. Rev. Lett. **59**, 2697 (1987) and

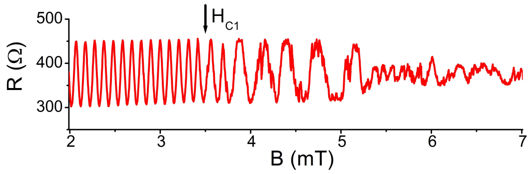

Figure 2.20: Resistance vs. magnetic field at temperature $T = 1.4\,\mathrm{K}$. As the magnetic field is increased, the resistance oscillates, due to the phase gradients generated by screening currents in the leads.

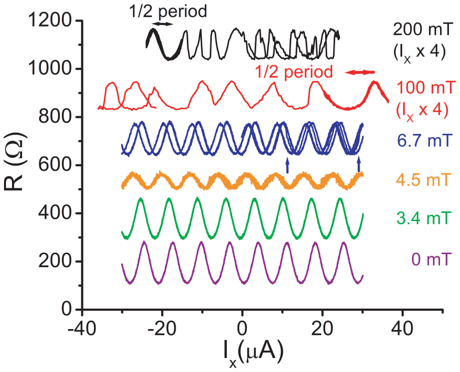

Figure 2.21: Resistance vs. cross-current measured at various values of the field at 1 K. For clarity, the curves have been offset vertically. The 100 mT and 200 mT curves have been horizontally magnified by a factor of 4. By measuring the resistance over a small range of cross-currents several times, if no detectable vortex jumps occur it is possible to measure at least half a period of oscillation, as indicated by the horizontal arrows.

### 2.7.2 Vorticial regime

Having shown that our device is capable of sensing resistance oscillations due to phase gradients created by external supercurrents, we now turn our attention to the application of magnetic fields $\gtrsim H_{\mathrm{c1}}$, which induce vortices in the thin-film leads and thus create additional phase gradients. All the measurements presented in what follows were performed on sample #2, which has the following geometry: cross-current strip width $w = 633\,\mathrm{nm}$, uncut lead width $2l = 17330\,\mathrm{nm}$, and wire separation $2a = 6133\,\mathrm{nm}$ (Fig. 2.16). Figure 2.20 shows the resistance as a function of magnetic field at $I_{\mathrm{X}} = 0$ and $T = 1.4\,\mathrm{K}$. The observed fast oscillations at low fields, i.e. before vortices penetrate the leads, are due to Meissner screening currents (see section 2.3), the dominant contribution to the oscillation period coming from the uncut lead [as its shortest dimension ($2l$) is larger (than $w$) by approximately a factor of 30]. From Eq. 2.21, we predict that the magnetic field needed to produce a $2\pi$ phase gain between wires (separated by $2a$) and, thus, a complete oscillation, due to screening currents in the uncut lead (of width $2l$) is given by $\Delta B_{\mathrm{th}} = (\pi^2/8G)(\Phi_0/2al) = 102.5\,\mu\mathrm{T}$, where $G$ is the Catalan number $\approx 0.916$. This agrees with the measured period $\Delta B_{\mathrm{exp}} = 101.8\,\mu\mathrm{T}$. At $\sim 3.5\,\mathrm{mT}$, the period of resistance oscillations abruptly changes, a change that we associate with the magnetic field $H_{\mathrm{c1}}$ above which vortices enter the uncut lead. The penetration of vortices into mesoscopic samples was studied previously, see for example [43, 60, 61], but to the best of our knowledge the effect of vortices on the magnetic field penetration depth was not studied. We observe that as the vortex density in the lead increases, the period of the resistance oscillations also increases, because the vortices are better able to compensate the Meissner screening currents. However, as the field is increased, the vortices frequently rearrange, making it impossible to observe resistance oscillations at 1.4 K for fields much above $H_{\mathrm{c1}}$.

Figure 2.21 shows the resistance as a function of cross-current at several values of applied magnetic field. At low fields, when vortices are absent, the cross-current induced oscillations are phase shifted with respect to one another for distinct magnetic fields but with no detectable difference in the oscillation period (see curves labeled 0 mT and 3.4 mT). This shift is due to the additional phase gradient caused by the Meissner currents associated with the applied magnetic field. At fields slightly above $H_{\mathrm{c1}}$, it is possible to see one of two types of resistance traces. Sometimes, we observe noisy oscillations with a smaller than expected amplitude (4.5 mT). We believe that this is due to one or more vortices that are rapidly wandering near one or both of the wires, i.e. a version of motional narrowing. At other times, we observe the same type of oscillation as observed below $H_{\mathrm{c1}}$, but with occasional jumps (6.7 mT) that become more frequent when the field is larger. At fields above $H_{\mathrm{c1}}$ for the cross-current carrying lead (i.e. the lead with the larger $H_{\mathrm{c1}}$),

---

Y. Oreg and A. M. Finkel'stein, Phys. Rev. Lett. **83**, 191 (1999). Thus, as expected, the $T_c$ we obtain for our nanowires is smaller than that of the film leads.

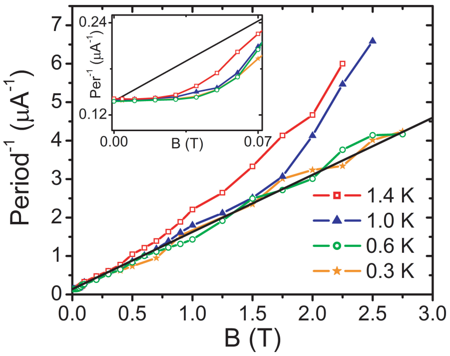

Figure 2.22: Inverse of the oscillation period from Fig. 2.21 vs. field, for four temperatures. The black line is generated from the Campbell formula with $\lambda_\perp = 46\,\mu\text{m}$ and $k = 370\,\text{N/m}^2$. The inset is a magnification of the low-field data, showing that the period is essentially field independent when vortices are absent (i.e. for fields $< H_{c1} \sim 0.02\,\text{T}$).

the period begins to decrease, as shown by the highlighted segments for the 100 mT and 200 mT traces in Fig. 2.21. As vortex jumps are prevalent at these fields, and our goal is to measure the period for a given vortex configuration, we determine the period by measuring it within "quiet regions" (i.e. current intervals with no jumps). Examples of such regions are indicated in Fig. 2.21 by horizontal arrows for the 100 mT and 200 mT traces.

We have investigated the resistance oscillation period of sample #2, as a function of magnetic field at four temperatures by making several scans of $I_\text{X}$ in "quiet regions," where it was possible to observe at least one peak and one valley several times before a vortex jump occurred. At temperatures below $\sim$ 700 mK, at which the device has an undetectable zero-bias resistance, we obtained the period from large bias-current resistance measurements (i.e. beyond the linear response regime). At each magnetic field and temperature, several measurements of the period were recorded and averaged. Smoothed curves of the inverse period, obtained via a moving average, are shown as functions of magnetic field in Fig. 2.22. We observe a roughly linear increase of the inverse period; compared to its zero-field value, the period at $B = 3$ T is some thirty times smaller. Such behavior is analogous to the linear dependence of the perpendicular penetration depth $\lambda_\perp$ on applied magnetic field (in the regime in which the vortex density is proportional to the field), i.e. the Campbell formula [55, 56, 57], adapted for thin films: $\lambda_{\text{C},\perp} = (1/d)\left(\lambda^2 + \Phi_0 B/\mu_0 k(T)\right)$. Here, $k(T)$ is the vortex pinning force constant (i.e. the Labusch parameter [58]). Campbell's picture of the origin of this law is that vortices are independently trapped near parabolic minima of a random pinning potential, and are slightly displaced from these minima in response to the Magnus force originating with a supercurrent. Insofar as the vortex density is proportional to the magnetic field, so is contribution of the vortices to the penetration depth. In the present setting, the phase fields from the vortices, displaced due to $I_{\mathrm{X}}$, enhance the phase gradients resulting from the cross-current, thus resulting in a shorter period for resistance oscillations with $I_{\mathrm{X}}$. We can therefore tie the Campbell prediction to the measured period by assuming the usual relation $n_{\mathrm{s}} = m/\mu_0 e^2 d\lambda_{\mathrm{C},\perp}$. From this expression and Eq. (2.52), we expect that the inverse period should increase linearly with magnetic field for our thin-film leads, $\Delta I_{\mathrm{X}}^{-1} = (2a/wd)(\mu_0\lambda^2/\Phi_0 + B/k(T))$. We estimate that $k \approx 370\mathrm{N/m}^2$ , compared to that of other materials, e.g., $> 100\mathrm{N/m}^2$ in Ref. [55] and $\sim 10^5\mathrm{N/m}^2$ in Ref. [62]. Furthermore, the inferred value of $\lambda_\perp(B = 0)$ is consistent with estmate from bulk penetration depth and film thickness. If we take the London penetration depth to be $\lambda \approx 0.5\mu$m, this gives thickness $d \approx 5.4\,\mathrm{nm}$, compared to 10.5 nm sputtered thickness. This is consistent with the expectation that the film is oxidized, thus the thickness of the superconductor is expected to be smaller than the sputtered thickness. As the data in Fig. 2.22 show, the inverse period does indeed increase linearly, except at higher temperatures and fields. In these regimes, inter-vortex interactions become important, and, as a result, $k$ can be effectively reduced. Furthermore, vortices explore a bigger area at higher temperatures and are less strongly pinned. For fields below $H_{c1} \sim 0.02\,\mathrm{T}$, at which no vortices are present in the lead carrying the cross-current, the period does not depend on the field, consistent with the Campbell scenario. The deviation from linear behavior at fields slightly above $H_{c1}$ is due to small number of vortices tunneling into the strip, and thus the average over uniformly distributed vortices does not hold.

### 2.7.3 Estimate of period due to magnetic fields generated by the cross current

In this subsection we estimate the contribution to the cross-current period from the magnetic fields generated by the cross-current. There are two main contributions due to this magnetic field. The first is due to the flux through the contour defined by the superconducting wires and the leads, and the second is due to the screening currents generated in the non-cross-current carrying lead. We demonstrate that for device geometry studied experimentally both of these contributions are small, and cannot explain the observed period.

For simplicity, we assume that the cross current is carried by an infinitely long strip of width $d$, instead of by a horseshoe shaped lead, see Fig. 2.23. In making this assumption, we over-estimate the strength of the magnetic field being generated by the cross current. Using the relation $\nabla \times B = \mu_0 J$, we find that the field generated by the cross-current is

$$B(z) = -\frac{\mu_0 I}{2\pi d} \log\left(\frac{z}{z+d}\right), \tag{2.54}$$

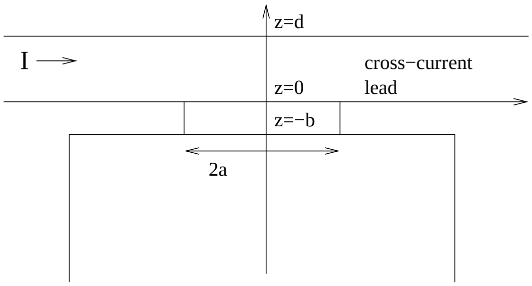

Figure 2.23: Geometry used to compute the effects of generated magnetic field

where $B(z)$ points out of the plane of the device, $z$ is the distance to the edge of the cross-current carrying lead, and $I$ is the total value of the cross current.

Integrating this magnetic field over the are of the fundamental contour, we find that the flux through the fundamental contour, measured in units of flux quanta, is

$$\frac{\Phi}{\Phi_0} \approx \frac{2ea\mu_0 I}{\pi h d} b \log(d/b), \tag{2.55}$$

where we have assumed that $d \gg b$. For the case of # 2, we find that the cross-current period due to this contribution is 4 mA as compared to the 7 $\mu$A due to the phase gradients created by the cross-current. Therefore, the additional contributions to the period caused by the generated flux passing through the fundamental contour are quite small.

Next, we estimate the screening-current density, and the associated contribution to the period caused by these screening currents, in the non-horseshoe lead induced by the generated magnetic field. As this lead is much narrower than the penetration depth, we ignore the feedback on the magnetic field due to the screening-currents. Following the same general steps as sec. 2.3.2, we obtain a series expansion for the phase field. Unfortunately, due to the logarithm in the expression for the magnetic field, this series cannot be easily summed, and therefore we sum it numerically. For the case of sample # 2, we find that the period caused by phase variations associated with these screening currents is 0.3 mA which is again only a small correction to the main contribution due to the phase variations in the cross-current carrying lead. Finally, for the case of sample # 2, we estimate the ratio of the current density of the screening-current on the edge of the lead to the cross-current is 0.01, supporting our hypothesis that we can ignore the feedback on the magnetic field due to the screening currents.

## 2.8 Concluding remarks

The behavior of mesoscale NQUIDs composed of two superconducing leads connected by a pair of superconducting nanowires has been investigated. Magnetoresistance measurements [38] have revealed strong oscillations in the resistance as a function of magnetic field, and these were found to have anomalously short periods. The period has been shown to originate in the gradients in the phase of the superconducting order parameter associated with screening currents generated by the applied magnetic field. The periods for five distinct devices were calculated, based on their geometry, and were found to fit very well with the experimental results

The amplitude of the magnetoresistance has been estimated via extensions, to the setting of parallel superconducting wires, of the IZ-AH theory of intrinsic resistive fluctuations in a current-biased Josephson junction for the case of short wires and the LAMH theory of intrinsic resistive fluctuations in superconducting wires for pairs of long wires. In both cases, to make the extensions, it was necessary to take into account the inter-wire coupling mediated through the leads. For sufficiently long wires, it was found that multiple metastable states, corresponding to different winding numbers of the phase of the order parameter around the AB contour, can exist and need to be considered. Accurate fits have been made to the resistance vs. temperature data at various magnetic fields and for several devices by suitably tuning the critical temperatures, zero-temperature coherence lengths, and normal-state resistances of the nanowires.

As these device are sensitive to the spatial variations in the phase of the order parameter in the leads, they may have applications as superconducting phase gradiometers. Such applications may include the sensing of the presence in the leads of vortices or of supercurrents flowing perpendicular to lead edges. We also note that our setup can be used to shed light on settings in which local fluctuations of the superfluid density play a pivotal role, such as those associated with the tail states predicted for superconductors with magnetic impurities (see e.g. [63]) and those in the junction of two two-dimensional superconducting films (see e.g. [64]).

# Chapter 3

# Superflow through arrays of nanosized apertures: disorder, fluctuations, avalanches, criticality, and other stories

Superflow in multiply-connected geometries demonstrates rich collective phenomena both in the non-dissipative (i.e. Josephson) and the dissipative (i.e. irreversible phase-slippage) regimes. In this chapter, and inspired by recent experiments [65], we construct and analyze a model describing both non-dissipative and dissipative superflow of a superfluid between two reservoirs through an array of nanosized apertures. The main ingredient of our model are the interactions between superflows through the various apertures, these interactions being mediated by the superflows in the bulk reservoirs. In addition, for the case of the dissipative regime, we add aperture-specific (i.e. quenched) disorder to describe the variations in the critical velocity in the various apertures.

In the non-dissipative we find that, due to the inter-aperture couplings, small arrays of apertures act as a single effective Josephson link having a coupling strength proportional to the number of apertures. More complex behavior is expected in larger arrays, which are studied via a renormalization-group approach.

In the dissipative regime, phase slips occurring in individual apertures are the source of dissipation. The interactions amongst the apertures tends to synchronize these phase-slips, whereas the disorder intrinsic to each aperture tends to desynchronize them. We find that competition between these tendencies leads to a disorder-driven continuous phase transition, at which a phase-slip avalanche of macroscopic size first occurs. We describe the critical properties of our model using the Martin-Siggia-Rose formalism, and find that due to the long range of the interactions, the upper critical dimension for this phase transition is three. We compute the critical exponents associated with the transition within mean-field approximation as well as corrections using an expansion around the upper critical dimension.

Recent experiments [66, 67, 68, 65] on the superflow of $^4$He between two reservoirs coupled via an array of nanosized apertures, depicted in Fig. 3.1, found that the system passes through several regimes of temperature, as the temperature is progressively lowered below the critical temperature $T_\lambda$ of the bulk system's transition to the superfluid state. Just below $T_\lambda$, and for sufficiently small supercurrents, the array was observed to function as a single effective Josephson junction having an essentially sinusoidal current-phase relation. For lower temperatures, below roughly a few millikelvin below $T_\lambda$, it was observed that the single-aperture dynamics becomes irreversible. This is due to the dissipative phase-slips that occur whenever the superflow velocity in an aperture reaches a critical value [69, 31, 70, 6]. At the high-temperature end of this regime, there is a narrow interval of temperatures, of width roughly 10 mK, within which all apertures appear to phase-slip simultaneously, and which Sato et al. [65] refer to as the *synchronous regime*. For lower temperatures, down to roughly 160 mK below $T_\lambda$, it appears that simultaneity in phase-slippage is lost; Sato et al. refer to this as the *asynchronous regime*.

The single-aperture dynamics is controlled by the ratio of the temperature-dependent healing length to the aperture diameter. For the aperture geometries used in the recent experiments, this ratio can be tuned to be either very large or very small by varying the temperature. We shall consider two limits, (1) the high-temperature limit, in which the healing length exceeds the aperture size and the dynamics is reversible, and the current-phase relation is sinusoidal; (2) the low-temperature limit, in which the aperture size exceeds the healing length, the dynamics is dissipative, and the current-phase relation is saw-tooth-like (linear, with sharp, periodic drops). In the low temperature regime, the sharp drops of the supercurrent occur whenever the supercurrent exceeds an aperture-dependent critical current, and the superflow in the aperture suffers a phase slip. In both regimes, the long-range nature of inter-aperture interaction mediated by the bulk superfluids plays an essential role.

For the case of $^4He$ it is known that a single aperture operating in the Josephson regime always has weak Josephson coupling as compared to thermal fluctuations ($E_J < k_B T$) [71]. We find that in the high-temperature regime, due to the long range of the interactions, the effective Josephson coupling between the reservoirs is proportional to the number of apertures, at least for sufficiently small arrays, supporting the conclusions of Ref. [72]. However, the effective coupling is suppressed by a factor arising from thermal fluctuations.

In the low-temperature regime, when dissipation sets in, the dynamics becomes more complex, due to the disorder associated with the aperture-to-aperture variability of the critical currents. Specifically, the inter-aperture interactions may lead to an avalanching behavior, in which a phase-slip in one aperture triggers phase-slips in one or more of its neighbors. We show that this avalanching phenomenon is analogous to ones observed in disparate physical systems, such as sliding tectonic plates [73], random-field magnets [74], and solids with disorder-pinned charge-density waves (CDWs) [75, 76], that feature competition between quenched disorder and interactions. We shall demonstrate a particular kinship to the soft-spin version of the

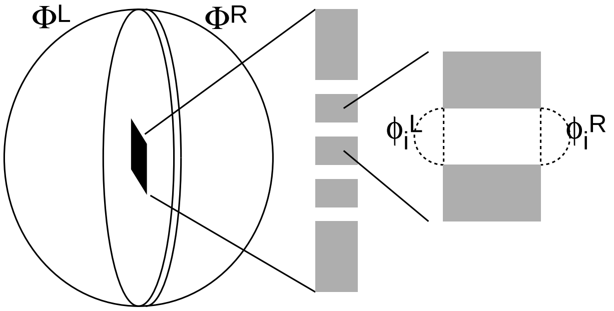

Figure 3.1: Schematic of the model system. Left: the location of the aperture array on the membrane is indicated by the black region, and the phases of the bulk superfluids far away from the nano-aperture array are labeled $\Phi^{\mathrm{L}}$ and $\Phi^{\mathrm{R}}$. Center: slice through the membrane, with apertures being represented by breaks in the membrane (white). Right: boundary conditions on hemispheres at the openings of the $i^{\mathrm{th}}$ aperture.

random-field Ising model (RFIM) [77]. We shall find that the interplay of the disorder and the interactions amongst the apertures leads to a phase transition in the dissipative dynamics. In the disorder-dominated phase, avalanches of phase-slips always terminate before reaching a scale comparable to the array size. On the other hand, the interaction-dominated phase is characterized by the presence of a system-wide avalanche involving a macroscopic fraction of apertures in the array. At the mean field level, this transition is similar to the one observed in the RFIM with nearest neighbor interactions. However, due the long range of the interactions, the upper critical dimension is lowered from 6 to 3 and, consequently, the fluctuation corrections to the mean-field results differ from one another.

The remainder of the chapter is arranged as follows: in the introductory part, section 3.1, we describe in detail our model of the inter-aperture interactions, the various temperature regimes of the single-aperture dynamics, and how both Josephson and phase-slip dynamics can be incorporated in the model. The remainder of the discussion is split into two parts. In section 3.2 we analyze the properties of our model in the Josephson regime of single aperture dynamics. In section 3.3 we present the main results of our work concerning the dissipative regime. There, we study the properties of the model at low temperatures by employing numerical analysis (subsec. 3.3.1), a mean-field approximation (subsec. 3.3.2), and an expansion around the upper critical dimension (subsec. 3.3.3). Finally, we discuss the implications of our models for the experiments (subsec. 3.3.10) and summarize our results (subsec. 3.3.11).

This work was done in collaboration with Roman Barankov and Paul M. Goldbart.

## 3.1 Introduction

The geometry of the system we wish to describe consists of two large reservoirs of superfluid, separated by a rigid barrier. Embedded in this barrier is an array of apertures, as shown in Fig. 3.1. We shall specialize to the case of an $N \times N$ array of apertures, each aperture having length $d$ and radius $r_0$, centered at the sites of a square lattice of lattice parameter $\ell$. It is straightforward to extend our analysis to other array geometries. It is convenient to regard the superfluid system as comprising three components: two are bulk components [i.e., the left (L) and right (R) reservoirs]; the third consists of the superfluid inside the apertures. We shall describe the state of the bulk helium in terms of the phase fields of the superfluid order-parameter. In doing this we are neglecting effects of amplitude excitations of the order parameter, including vortices, within the bulk. In contrast, within the apertures we shall retain both amplitude and phase degrees of freedom. We imagine controlling the system by specifying the phases $\Phi^{\mathrm{L/R}}$ on surfaces in the bulk superfluids far from the array of nanoapertures (see Fig. 3.1). We believe that this level of description allows us to capture the following important elements: (a) apertures that exhibit Josephson dynamics in the high temperature regime and dissipative dynamics due to narrow-wire-like meta stable states, these states being connected by phases slips, in the low temperature regime; and (b) interactions mediated through the bulk superfluid in the two reservoirs, which couple pairs of apertures to one another and also couple the apertures to the control phases $\Phi^{\mathrm{L/R}}$.

We can consider two possible ways to drive the system: either by fixing the total current through the aperture array or the chemical potential difference $\Delta\mu$ across it. We shall focus on the second strategy, which amounts to fixing the rate of change of the control phase difference $\Phi^{\mathrm{L}} - \Phi^{\mathrm{R}}$ via the Josephson-Anderson relation

$$\Phi^{\mathrm{L}} - \Phi^{\mathrm{R}} = \frac{\Delta\mu}{\hbar}\, t, \tag{3.1}$$

where $t$ is the time that has passed from the moment when $\Delta\mu$ was first applied. Fixing $\Delta\mu$ corresponds to the typical experimental setup in experiments on superfluid helium [78]. If we wish to fix the total current, as is typical for experiments on superconductors, we can perform a Legendre transform to change the independent variable from the control phase difference to the total current [30].

We separate the description of the bulk superfluid from the superfluid inside the apertures by specifying the phases in the vicinity of the aperture openings. That is for $i^{\mathrm{th}}$ aperture we specify the phases in the vicinity of the left and right openings to be $\phi_i^{\mathrm{L}}$ and $\phi_i^{\mathrm{R}}$ respectively. The total energy,

$$H^{\mathrm{tot}}[\Phi^{\mathrm{L}}, \Phi^{\mathrm{R}}, \{\phi_i^{\mathrm{L}}, \phi_i^{\mathrm{R}}\}] = H^{\mathrm{L}}[\Phi^{\mathrm{L}}, \{\phi_i^{\mathrm{L}}\}] + H^{\mathrm{R}}[\Phi^{\mathrm{R}}, \{\phi_i^{\mathrm{R}}\}] + \sum_{\mathrm{apertures}} H_i[\phi_i^{\mathrm{L}} - \phi_i^{\mathrm{R}}], \tag{3.2}$$

correspond to the sum of the energy of the superfluid in the left ($H^{\mathrm{L}}$) and right ($H^{\mathrm{R}}$) reservoirs as well as inside the apertures ($H_i$). We have traced out all the internal degrees of freedom both in the bulk and aperture Hamiltonians. The partition function for the entire system of reservoirs and apertures is given by

$$Z[\Phi^{\mathrm{L}}, \Phi^{\mathrm{R}}] \equiv Z[\Phi^{\mathrm{L}} - \Phi^{\mathrm{R}}] = \int D[\{\phi_i^{\mathrm{L}}, \phi_i^{\mathrm{R}}\}]\, Z^{\mathrm{L}}[\Phi^{\mathrm{L}}, \{\phi_i^{\mathrm{L}}\}]\, Z^{\mathrm{R}}[\Phi^{\mathrm{R}}, \{\phi_i^{\mathrm{R}}\}] \prod_{\mathrm{apertures}} e^{-\beta H_i[\phi_i^{\mathrm{L}} - \phi_i^{\mathrm{R}}]}, \tag{3.3}$$

where the partition functions $Z^{\mathrm{L/R}}$ for the left and right bulk superfluid will be defined in the following subsection.

After obtaining the effective bulk energy and partition function in subsec. 3.1.1, we consider in more detail the single aperture dynamics. In subsec. 3.1.2, we focus on the Josephson regime. For the case of superfluid helium, due to the small value of the healing length this regime has only recently become experimentally accessible [66]. As we discuss in more detail, there is an additional complication for the case of $^4$He, as was pointed out in Ref. [71]. Due to the scaling with temperature of the superfluid stiffness and coherence length, the Josephson coupling turns out always to be very weak as compared to thermal fluctuations. To compensate, exquisite microfabrication of multi-aperture arrays, in which the apertures work in concert as an effective single strong Josephson junction, is required [72]. In subsec. 3.1.3, we construct a simple model that captures the irreversibility of the dynamics in the phase-slippage regime.

### 3.1.1 Bulk energy

In this subsection we describe the origin of the effective inter-aperture interaction energy $H^{\mathrm{L/R}}$. As a starting point, we describe the left/right bulk superfluid helium reservoirs by the phase-only energy density

$$\widetilde{H}^{\mathrm{L/R}} = \frac{K_s}{2} \int_{\mathrm{L/R}} d^3r \left|\boldsymbol{\nabla}\chi^{\mathrm{L/R}}(\mathbf{r})\right|^2, \tag{3.4}$$

where the fields $\chi^{\mathrm{L/R}}$ represent the phase of the superfluid order parameter in the left/right reservoir, $K_s \equiv \hbar^2 n_s/m$ is the superfluid stiffness, in which $n_s(T) \approx \kappa\, n_0(1 - T/T_\lambda)^{2/3}$ is the superfluid number density ($n_0 \approx 2.2 \times 10^{22}\,\mathrm{cm}^{-3}$ is the density of $^4$He, $\kappa \approx 2.38$ is a proportionality constant, $T_\lambda \approx 2.18\,\mathrm{K}$) and $m$ is the mass of a $^4$He atom.

Consider the partition function for the left bulk superfluid

$$Z^{\mathrm{L}}[\Phi^{\mathrm{L}}, \{\phi_i^{\mathrm{L}}\}] = \int D[\chi^{\mathrm{L}}(\cdot)]\, e^{-\beta \tilde{H}[\chi^{\mathrm{L}}]}, \tag{3.5}$$

subject to the following constraints:

1. the phase at infinity (to the left) is $\Phi^{\mathrm{L}}$;
2. no current flows through the membrane surface between the apertures, i.e. $n \cdot \nabla \chi^{\mathrm{L}} = 0$ on the membrane surface, where $n$ is the unit normal vector to the membrane;
3. for each aperture $i$, the phase on a hemisphere of radius $r_0$ centered at the opening of the $i^{\mathrm{th}}$ aperture is specified to be $\phi_i^{\mathrm{L}}$.

The choice of the geometrical surface for the last of the boundary conditions is made for convenience, as it simplifies the resulting mixed boundary value problem whilst enforcing the physical condition of continuity of the phase in the vicinity of the aperture opening. To extend our picture to various reservoir geometries, as we shall do in subsec. 3.3.10, it is necessary to add appropriate additional boundary conditions describing the walls of the reservoir.

Our goal is to reduce the model to one involving only the phase-differences across the apertures and the control phases. We proceed by tracing out the internal degrees of freedom of the bulk superfluid $\chi^{\mathrm{L/R}}$. As the bulk Hamiltonian is quadratic, we can accomplish this simply by minimizing the energy, Eq. (3.4), in the reservoirs. This gives us the correct answer for the energy, up to an irrelevant additive factor describing fluctuations. This is carried out explicitly for an example of a single aperture in appendix D. By minimizing the energy in the bulk, Eq. (3.4), we find that $\chi^{\mathrm{L(R)}}(\mathbf{r})$ obeys the Laplace equation, $\nabla^2 \chi^{\mathrm{L(R)}}(\mathbf{r}) = 0$, subject to the boundary conditions specified in the previous paragraph.

To solve the resulting mixed boundary value Laplace problem we appeal to its electrostatics analogy, in which the phase $\chi$ and the superfluid stiffness $K_s$ respectively play the roles of the electrostatic scalar potential $\varphi$ and the permittivity $\epsilon_0$. We continue to concentrate on the left bulk superfluid, and ask the question: what is the energy of the analogous electrostatic field? Consider reflecting the left bulk with respect to the plane formed by the left edge of the aperture containing membrane to extend the problem from the left half-space to the entire space. Upon performing this reflection, we obtain a new set of boundary conditions:

1. the phase at infinity (to the left and to the right) is $\Phi^{\mathrm{L}}$;
2. no current flows through the reflection plane;

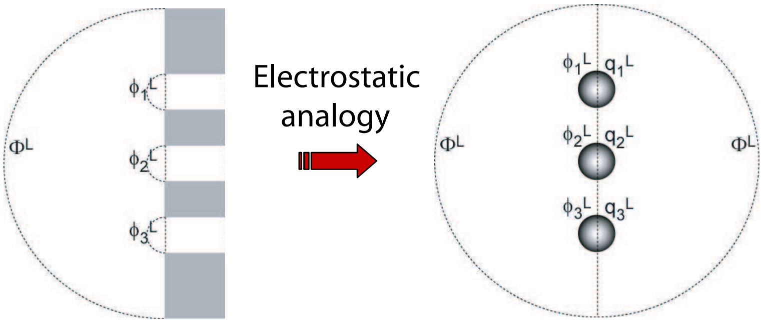

Figure 3.2: Left: schematic of the mixed boundary value problem for the superflows in the left reservoir. The solid block represents the membrane and the breaks in it represent the apertures. The surface labeled $\Phi^{\mathrm{L}}$ represents the boundary condition on the phase of the order parameter far away from the aperture array. The hemi-spherical surfaces labeled $\phi_1$, $\phi_2$, and $\phi_3$ represent the boundary condition on the phase of the order parameter on these imaginary surfaces located at the aperture openings. Right: schematic for the analogous electrostatics boundary value problem. In the picture on the right, the picture on the left has been duplicated and one copy reflected across the plane formed by the left edge of the aperture containing membrane. The hemispherical surfaces of constant phase at the aperture openings on the left have been replaced by equipotential spheres (spherical capacitors) on the right. Similarly, the boundary condition at infinity to the left has been replicated on the right.

3. for each aperture $i$, the phase on a sphere of radius $r_0$, formed from the original hemisphere and its reflection is specified to be $\phi_i^{\mathrm{L}}$.

These boundary condition specify an electrostatics problem to compute the energy of the electric field produced by an array of conductive spheres (spherical capacitors) held at fixed potentials, see Fig. 3.2. Condition (2.) is automatically satisfied due to the symmetry of the problem. To compute the energy, in terms of the boundary data, we apply the divergence theorem to Eq. (3.4) to obtain the energy in terms of a surface integral:

$$\widetilde{H}^{\mathrm{L}} = \frac{K_s}{2}\int_{\partial\,\mathrm{L}} d\mathbf{S}\cdot\chi^{\mathrm{L}}\boldsymbol{\nabla}\chi^{\mathrm{L}} - \frac{K_s}{2}\int_{\mathrm{L}} d^3r\,\chi^{\mathrm{L}}\,\nabla^2\chi^{\mathrm{L}}, \tag{3.6}$$

where the volume (i.e. the last) term vanishes upon minimization (computing the variation of $\widetilde{H}^{\mathrm{L}}$ with respect to $\chi^{\mathrm{L}}$, we find that the minimum-energy configuration $\chi^{\mathrm{L}}$ obeys $\nabla^2\chi^{\mathrm{L}} = 0$). To simplify the evaluation of the surface integral we make use of the fact that the energy is invariant under global shifts of the potential. Thus, we lower all potentials by $\Phi^{\mathrm{L}}$, which eliminates the contribution from the (left and right) surfaces at infinity. What remains are the contributions from the surfaces of the spherical capacitors, which give the effective energy

$$H^{\mathrm{L}} = \frac{1}{2}\sum_{\text{apertures}}(\phi_i^{\mathrm{L}} - \Phi^{\mathrm{L}})\,q_i, \tag{3.7}$$

which is a well known relation in electrostatics. Here, for each aperture $i$, the phase $\chi^{\mathrm{L}}$ takes the constant value $\phi_i^{\mathrm{L}}$ (shifted to $\phi_i^{\mathrm{L}} - \Phi^{\mathrm{L}}$) on the associated spherical surface, and the remaining surface integrals have been replaced (via the analogue of Gauss's law) by the supercurrent out of the surface which is the analogue of the charge enclosed $q_i$. For aperture $i$ this "charge" is $q_i \equiv K_s \int d\mathbf{S} \cdot \boldsymbol{\nabla}\chi^{\mathrm{L}}$, where the integral is taken over the spherical surface. What remains is to determine the charges $q_i$. To do this, we consider the $i^{\mathrm{th}}$ sphere: in the limit $\ell \gg r_0$, where $\ell$ is the distance between the closest apertures (i.e. ignoring di- and higher-order charge-multipoles), the potential on its surface obeys

$$K_s\left(\phi_i^{\mathrm{L}} - \Phi^{\mathrm{L}}\right) = \sum_j C_{ij}^{-1} q_j, \tag{3.8a}$$

$$C_{ij}^{-1} \equiv \frac{\delta_{ij}}{4\pi\, r_0} + \frac{1-\delta_{ij}}{4\pi\, |r_{ij}|}, \tag{3.8b}$$

where $|r_{ij}|$ is the distance between the $i^{\mathrm{th}}$ and $j^{\mathrm{th}}$ aperture (sphere) centers, and $C_{ij}$ is the analogue of the *capacitance matrix*. By solving Eq. (3.8a) for the $q_i$'s and eliminating them from Eq. (3.7) (and dividing by two, as we want the energy of the left bulk only), we arrive at the energy of the superfluid in the left reservoir.

$$H^{\mathrm{L}} = \frac{K_s}{4} \sum_{ij} (\phi_i^{\mathrm{L}} - \Phi^{\mathrm{L}})\, C_{ij}\, (\phi_j^{\mathrm{L}} - \Phi^{\mathrm{L}}). \tag{3.9}$$

In general the structure of the $C_{ij}$ matrix is as follows: the diagonal elements $C_{ii} \sim 4\pi r_0$ are positive, while the off diagonal elements are negative, with the property $\sum_j C_{ij} > 0$. For an infinite regular array of apertures, $C_{ij}$ may be obtained by Fourier transforming $C_{ij}^{-1}$, inverting, and anti-Fourier transforming. Upon performing this procedure, we find that the $C_{ij}$ matrix has the following asymptotes

$$C_{ij} \sim \begin{cases} r_0^2/|r_{ij}|, & |r_{ij}| \ll \ell^2/r_0 \\ \ell^4/|r_{ij}|^3, & |r_{ij}| \gg \ell^2/r_0 \end{cases} . \tag{3.10}$$

The inter-aperture coupling falls off as $1/r$ for aperture that are close together, and as $1/r^3$ for apertures that are far apart. The $1/r^3$ long range nature of the interaction is key for determining the properties of large aperture arrays. This form of dependence of the inter-aperture coupling on the distance between the apertures seems to be generally true, based in numerical investigations, as long as the square root of the total number of apertures satisfies $N \gg \ell/r_0$. The infinitely large array limit has an the additional property that $\sum_j C_{ij} = 0$. This property implies the decoupling from the control phase in the bulk, which is sensible as the problem becomes one-dimensional.

### 3.1.2 Single-aperture dynamics in the Josephson regime

Having obtained the effective energy for the bulk superfluids, we complete the description by specifying the effective energy of the superfluid in the apertures. In the present subsection we shall concentrate on the temperature regime in which apertures act as Josephson junctions. In this regime the current-phase relation for a single aperture is single-valued, and the single aperture energy is given by

$$H_i = -E_J \cos(\phi_i^{\mathrm{L}} - \phi^{\mathrm{R}}). \tag{3.11}$$

The Josephson effect is an important consequence of macroscopic quantum phenomena. In the setting of superconductors, it was first proposed by Brian Josephson in 1962 [79], and was observed soon thereafter [80, 81]. More recently, the Josephson effect has also been observed between two weakly coupled BEC [82], as well as in superfluid $^3$He [83, 84, 78] and $^4$He [66, 68] weak links.

Being able to observe any sort of Josephson effect in $^4$He is a serious concern because the Josephson coupling strength across a single aperture is always smaller than $k_{\mathrm{B}}T$ [71]. This may be demonstrated by the following scaling analysis due to Zimmermann [71, 72], which shows that the maximum Josephson coupling for a given aperture is independent of its size, and is very small. Consider an aperture having radius $r_0$ and length (membrane thickness) $d$. Here, we shall focus on the experimentally relevant situation of apertures having $d \sim 2r_0$. Following Ref. [72], the Josephson coupling strength $2E_J$ is roughly proportional to the largest kinetic energy achievable within the aperture, i.e.

$$2E_J \approx \frac{n_{\mathrm{s}}\hbar^2}{2m_4} \int |\nabla\phi|^2 d^3x, \tag{3.12}$$

where $n_s$ is the superfluid density, $m_4$ is the mass of a $^4$He atom, $\phi$ is the phase of the order parameter, and the integral runs over the volume of an aperture. The maximum kinetic energy is achieved when the phase difference across the aperture is $\pi$, for which $\nabla\phi \sim \pi/d$. To maximize $E_J$ we lower the temperature so as to maximize the superfluid fraction. However, in order for the aperture to function in the Josephson regime, we must stop lowering the temperature at the point where the temperature-dependent healing length is comparable to the aperture diameter. This point defines the temperature $T_m$, via the relation $\xi(T_m) = 2r_0$. Below $T_m$ the aperture stops acting as a Josephson junction. Therefore, the maximal Josephson coupling occurs at the temperature $T_m$, where it obtains the value $E_J \approx \frac{n_{\mathrm{s}}(T_m)\hbar^2}{2m}\xi(T_m)$. Using the scaling relations near $T_\lambda$, i.e. $n_s \approx n_0'(1 - T/T_\lambda)^{2/3}$ and $\xi(T) \approx \xi_0(1 - T/T_\lambda)^{-2/3}$, we find that $E_J \sim 0.6\,\mathrm{K}$ is independent of $T_m$ and therefore it is also independent of the aperture size.

Due to the fact that $\xi_0 \sim 2 \times 10^{-10}\,\mathrm{m}$, which is much smaller than the smallest aperture that can be made, in order for an aperture to operate in the Josephson regime the temperature must be very near the transition temperature, $T_\lambda = 2.18\,\mathrm{K}$. As $E_J < k_B T$, the Josephson effect is not expected to survive for the case of a single aperture [34].

### 3.1.3 Single-aperture dynamics in the phase slippage regime

For single apertures operating in the dissipative regime, observations of single-phase slip events were first reported in Refs. [85, 83]. The cross-over between the Josephson and the dissipative regimes has been studied experimentally in Ref. [68]. It was found that as the temperature is lowered, and thus the temperature-dependent healing length decreased, the sinusoidal current-phase relation becomes distorted into the shape of a breaking wave. This reflects the development of metastable current-carrying states that first appear when the healing length becomes commensurate with the aperture size. The switching between these metastable states occurs through phase-slip processes, which arise from vortex lines crossing the aperture [31].

To account for phase-slippage processes within an aperture we shall use a modified phase-only model that accounts for the vanishing of the amplitude associated with vortex lines by keeping track of the number of phase slips that have occurred. Therefore, we take the energy of the superfluid inside the $i^{\mathrm{th}}$ aperture to be

$$H_i = \frac{K_s}{2} J \left(\phi_i^{\mathrm{L}} - \phi_i^{\mathrm{R}} - 2\pi n_i\right)^2 , \tag{3.13}$$

in which $J(\equiv \pi\, r_0^2/d)$ accounts for the geometry of the aperture, where $d$ is of the order of the membrane thickness. The integer $n_i$ counts the net number of phase slips that would occur in the $i^{\mathrm{th}}$ aperture if the system were to progress to its present state from a reference state in which the phases were uniform throughout the system.

We complete the description of our model by specifying the single-aperture dynamics, and thus the mechanism by which energy is dissipated in the apertures. The superfluid velocity $v_i$ in a aperture of thickness $d$ is defined by the phases at the aperture openings: $v_i = \hbar \nabla \phi_i / m \approx \hbar \left(2\phi_i^{\mathrm{L}} - 2\pi n_i\right)/dm$. Correspondingly, the current through the aperture is given by

$$I_i = \frac{K_s J}{\hbar} \left(2\phi_i^{\mathrm{L}} - 2\pi n_i\right) . \tag{3.14}$$

When the velocity through the $i^{\mathrm{th}}$ aperture exceeds its critical value $v_{c,i}$ (or, equivalently, $\phi_i^{\mathrm{L}} - \pi n_i$ exceeds $\phi_{c,i}$), a vortex line nucleates and moves across the aperture, which decreases the phase-difference along a path from the far left, through the $i^{\mathrm{th}}$ aperture, to the far right by $2\pi$, whilst the phase-difference along a path through any other aperture remains unaffected. In our model, we implement this kind of phase-slip event by sending $n_i$ to $n_i + 1$ (assuming all flow is to the left).

The Berkeley group's experiments are primarily conducted in the temperature regime in which $T$ is close to $T_\lambda$ [65]. In this regime, the intrinsic critical velocity is proportional to the superfluid stiffness [85, 70, 6]:

$$v_c(T) \simeq \hbar/m\xi(T) \propto K_s(T), \tag{3.15}$$

where, as before, $\xi(T) \simeq \xi_0(1-T/T_\lambda)^{-2/3}$ is the temperature-dependent superfluid healing length. Extrinsic effects are known to reduce critical velocities from their intrinsic values. We hypothesize that in the Berkeley group's experiments these extrinsic effects originate in atomic-scale roughness of the aperture walls, and play a pivotal role in generating critical-velocity variability amongst the apertures. This variability is expected to be temperature dependent, because only roughness on length-scales longer than $\xi(T)$ can substantially perturb the order parameter and thus influence the critical velocities. Hence, at higher temperatures the impact of surface roughness is expected to be weaker and, correspondingly, the distribution of critical velocities is expected to be narrower. Under this hypothesis, lowering the temperature has the important effective consequence of increasing the effective disorder [1].

### 3.1.4 Summary of the model

To summarize, we describe the three components of the system by the total energy

$$H = H^{\mathrm{L}} + H^{\mathrm{R}} + \sum_i H_i, \tag{3.16}$$

where $H^{\mathrm{L/R}}$, given by the Eq. (3.16), describes the superflows in the left/right bulk superfluid and $H_i$ describes the superflow in the $i^{\mathrm{th}}$ aperture and has different functional form in the low-temperature regime Eq. (3.11) and high-temperature regime Eq. (3.13). We connect the description of the bulk superfluids to that of the superfluids within the apertures by specifying the phases at the interfaces. That is, in the vicinity of the aperture openings we specify the phases to be $\phi_i^{\mathrm{L/R}}$ (Fig. 3.1). Having specified $\phi_i^{\mathrm{L/R}}$ and $\Phi^{\mathrm{L/R}}$, we can express $H^{\mathrm{L/R}}$ through a set of effective couplings between the phases in the vicinities of the various apertures and the control phases. For convenience, we set $\Phi^{\mathrm{R}} = -\Phi^{\mathrm{L}}$ by a suitable choice of gauge, and focus on states in which the left and right hand sides of the system are symmetric, so that $\phi_i^{\mathrm{R}} = -\phi_i^{\mathrm{L}}$. In this case, we need only specify the (L) phases for a full description of the system, which is what we shall do

---

[1] Similar ideas have been suggested by Y. Sato and co-workers (private communication (2006)).

from now on.

## 3.2 Analysis of array dynamics in the Josephson regime

In this section, we demonstrate that multiple apertures can cooperate to make the Josephson effect in $^4$He observable. The main result of this section is that for small arrays of apertures the total effective Josephson coupling $E_J^{\mathrm{tot}}$ is given by

$$E_J^{\mathrm{tot}} = N^2 \widetilde{E}_J, \tag{3.17}$$

where $\widetilde{E}_J$ is the effective single-aperture coupling and $N^2$ is the total number of apertures. Our result agrees with that of Ref. [72], in that the total coupling is proportional to the number of apertures. However, in contrast to the conclusions of Ref. [72], we find that the phases in the vicinity of the aperture openings always suffer strong thermal fluctuations and are not locked together. As a result, Eq. (3.17) features an effective single aperture coupling that accounts for the thermal fluctuations $\widetilde{E}_J$ instead of the bare coupling $E_J$. Finally, for large arrays, due to correlated fluctuations, the total coupling grows slower than the array size.

We proceed by: (1) identifying a model for the energetics of the superflows through the apertures and the bulk superfluid reservoirs, making the approximation that the superfluid in the vicinity of the aperture array comes into equilibrium much more quickly than the phase difference between the bulk superfluids evolves in time; (2) integrating out the fluctuations in the bulk superfluids; and (3) obtaining the effective coupling between the bulk superfluids by tracing over the configurations of the phases in the vicinity of the aperture openings using both analytical and numerical approaches.

We begin by assuming that the bulk reservoirs are large and three dimensional, and therefore there is a well-defined phase difference between them. Furthermore, we shall assume that this phase difference evolves slowly in time, such that the superfluid in the vicinity of the apertures is always in thermal equilibrium, subject to the constraint that deep within the bulk the phase approaches $\Phi^{\mathrm{L/R}}$ in the left/right reservoir. The goal is to obtain the effective free energy of the superfluid in the apertures and in the bulk reservoirs as a function of $\Delta\Phi \equiv \Phi^{\mathrm{L}} - \Phi^{\mathrm{R}}$, and thus to extract the total Josephson coupling.

Following Eq. (3.3), the partition function for a given $\Delta\Phi$ is

$$Z[\Delta\Phi] = e^{-\beta S_{\text{eff}}[\Delta\Phi]}, \tag{3.18}$$

$$S_{\text{eff}}[\Delta\Phi] = \frac{K_s}{2}\sum_{ij}(\phi_i^{\text{L}} - \Phi^{\text{L}})C_{ij}(\phi_j^{\text{L}} - \Phi^{\text{L}}) - E_J\sum_i \cos(2\phi_i^{\text{L}}). \tag{3.19}$$

Before continuing with a detailed analysis of the model, we pause to demonstrate that, within this model, the fluctuations of the phase across any individual aperture are large (compared to $2\pi$). The phase $\phi_i$ across the $i^{\text{th}}$ aperture is constrained from fluctuating by both the $E_J$ (Josephson) term and by its coupling to the other apertures and to the phase deep in the bulk via the $C_{ij}$ term. The fluctuations across a given aperture will be weakest when the two terms constraining it are largest. Assuming that we have already tuned the temperature so as to maximize $E_J$ while remaining in the Josephson regime of single aperture dynamics, we concentrate on tuning the $C_{ij}$ term. Largest constraint by the $C_{ij}$ term is achieved for the case of a large array, with all the $\phi_j$'s except the one of interest frozen so that they cannot fluctuate. Locking all the other phases to zero (or a multiple of $\pi$ to ensure that both the Josephson term and the inter-aperture coupling term have the same minimum), we find that the energy associated with fluctuations of the phase across $i^{\text{th}}$ aperture is

$$\frac{K_s}{2}C_{ii}\phi_i^2 + E_J\cos\phi_i, \tag{3.20}$$

where the first term is approximately $2\pi K_s r_0 \phi_i^2$ and the second term is approximately $\sim K_s \pi r_0/d\cos(\phi_i)$. For the geometry of interest, $2r_0 \sim d$, we see that the presence of the other apertures in the array only changes the total energy for fluctuations of $\phi_i \to \pm 2\pi$ by a small factor. However, from the form of Eq. (3.20) we see that the aperture is constrained to fluctuate around the point $\phi_i = 0$. We believe that this observation is the key to understanding the observation of the Josephson effect in aperture array. Furthermore, due to the long range order present in superfluid, relaxing the condition that all the other apertures are frozen does not significantly affect this conclusion.

Next, we integrate over the $\phi_i$'s, to obtain an effective action (and the associated partition function) for the phases at infinity. This is hard to do directly, due to the non-linear cosine term. A useful approach is to replace the cosine potential by the Villian potential. The prescription for doing this is to perform the following replacement:

$$e^{\beta E_J\cos(x)} \to \sum_{\eta=-\infty}^{\infty} e^{-\beta\frac{E_V}{2}(x-2\pi\eta)^2}, \tag{3.21}$$

which produces another periodic potential with similar amplitude. This mapping is only approximate, however, physical results should remain unchanged provided that we correctly scale the the Villian potential relative to the cosine potential (i.e. conserve the amplitude of the energy difference between the maximum and minimum of the potential), which we do using the following (implicit) transformation:

$$2\beta E_J = \frac{\text{EllipticTheta}[3, 0, e^{-2\pi^2\beta E_V}]}{\text{EllipticTheta}[2, 0, e^{-2\pi^2\beta E_V}]}. \tag{3.22}$$

Upon transforming to the Villian potential, we obtain:

$$Z = \int D[\Phi^{\mathrm{L}}] D[\phi_i^{\mathrm{L}}] \sum_{\{\eta_i\}} \exp\left[-\beta\frac{K_s}{2}\left(\sum_{ij}(\phi_i^{\mathrm{L}} - \Phi^{\mathrm{L}})C_{ij}(\phi_j^{\mathrm{L}} - \Phi^{\mathrm{L}}) + \frac{E_V}{2}\sum_i (2\phi_i^{\mathrm{L}} - 2\pi\eta_i)^2\right)\right], \tag{3.23}$$

where $\{\eta_i\}$ stands for all possible combinations of the Villian "charges." We can now perform the integral over the $\phi_i^{\mathrm{L}}$'s, to obtain an effective partition function with the Villain charges and $\Delta\Phi$ as the remaining degrees of freedom:

$$Z = \int D[\Phi^{\mathrm{L}}] \sum_{\{\eta_i\}} e^{-\beta H_{\mathrm{eff}}(\Phi^{\mathrm{L}}, \{\eta_i\})} \tag{3.24}$$

$$H_{\mathrm{eff}}(\Phi^{\mathrm{L}}, \{\eta_i\}) = \left[-\frac{1}{4}\sum_{ij}\left(\Phi^{\mathrm{L}}\frac{K_s}{2}\sum_k C_{ki} + 2\pi E_V\eta_i\right)\left(\frac{K_s}{4}C_{ij} + \frac{E_V}{2}\delta_{ij}\right)^{-1}\left(\Phi^{\mathrm{L}}\frac{K_s}{2}\sum_m C_{mj} + 2\pi E_V\eta_j\right)\right. \tag{3.25}$$

$$\left. + \frac{K_s}{4}(\Phi^{\mathrm{L}})^2\sum_{ij} C_{ij} + \frac{E_V}{2}\sum_i (2\pi\eta_i)^2\right]. \tag{3.26}$$

To make further progress, we make the small, well spaced array approximation, i.e. we ignore the off-diagonal elements of the $C_{ij}^{-1}$ matrix, and approximate the diagonal ones by $C_{ii}^{-1} \approx 1/4\pi r_0$. The effective action under this assumption becomes

$$S_{\mathrm{eff}}(\Phi) = -\frac{1}{\beta}\log Z[\Phi] = N^2 E_J\left[\frac{E_V K_s}{K_s + 2E_V C_{ij}^{-1}}\right]\cos(\Phi), \tag{3.27}$$

where $E_J[.]$ is transformation (3.22) from $E_V$ to $E_J$, and $N^2$ is the total number of apertures. This is clearly just $N^2$ times the action for a single aperture. Here, $\widetilde{E}_J \equiv E_J\left[\frac{E_V K_s}{K_s + 2E_V C_{ij}^{-1}}\right]$ plays the role of an effective coupling, which takes into account the "fringe" fields, i.e. the hydrodynamic flows around the aperture. Therefore, it is easy to see that whenever $N^2$ is large enough, the total coupling can exceed the strength of thermal fluctuations, leading to the Josephson effect using the mechanism described in Ref. [72]. However,

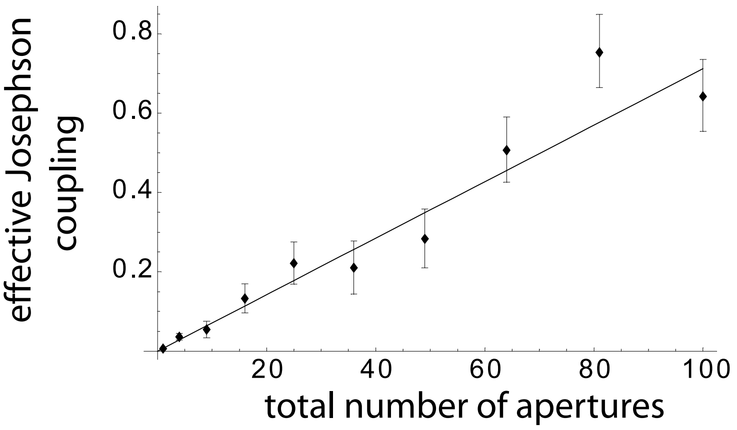

Figure 3.3: (double) the effective Josephson coupling strength, i.e. $F[\Delta\Phi = \pi] - F[\Delta\Phi = 0]$, as a function of the number of apertures. The straight line is not a fit, but the expected coupling from the linear law.

it is important to note that there may still be large fluctuations across the various apertures. We have verified this result numerically by computing the difference in the free energy $F[\Delta\Phi = \pi] - F[\Delta\Phi = 0]$. The numerical evaluation is performed in two steps. First, we compute the ratio of the partition functions $Z[\Delta\Phi = \pi]/Z[\Delta\Phi = 0]$. This ratio can be expressed as an expectation value

$$Z[\Delta\Phi = \pi]/Z[\Delta\Phi = 0] = \frac{\sum_{\{\eta_i\}} e^{-\beta H_{\text{eff}}(\Phi=\pi),\{\eta_i\}}}{\sum_{\{\eta_i\}} e^{-\beta H_{\text{eff}}(\Phi=0),\{\eta_i\}}} = \langle e^{-\beta(H_{\text{eff}}(\Phi^{\text{L}}=\pi,\{\eta_i\})-H_{\text{eff}}(\Phi^{\text{L}}=0,\{\eta_i\}))}\rangle_{\Phi^{\text{L}}=0}, \tag{3.28}$$

where the expectation value is computed with respect to the probability distribution $e^{-\beta H_{\text{eff}}(\Phi^{\text{L}}=0,\{\eta_i\})}$ using the Metropolis algorithm. Second, we find the free energy difference via

$$F[\Delta\Phi = \pi] - F[\Delta\Phi = 0] = -k_B T \log \frac{Z[\Delta\Phi = \pi]}{Z[\Delta\Phi = 0]}. \tag{3.29}$$

This free energy difference appears to be proportional to the number of apertures in the array, for a wide range of temperatures and array geometries, see Fig. 3.3.

Therefore, in the limit of independent apertures we recover the result of Ref. [72], but we simultaneously find large fluctuations in the aperture dynamics. If the apertures are not independent, i.e. $C_{ij}^{-1}$ has off-diagonal elements, then the fluctuations on the various apertures will be coupled to each other rather than the phase deep in the bulk. This fact can be easily observed for an infinitely large array, where, due to translational invariance, $\sum_j C_{ij} = 0$, and therefore the coupling between the bulk phases must scale slower than the array size.

## 3.3 Analysis of the array dynamics in the phase-slippage regime

As we demonstrate later, the quenched disorder in the critical velocities of various apertures dominates over the disorder associated with thermal noise. Thus, in this section we begin by concentrating on the quasi-static dynamics of phase-slippage in the aperture array and assume that the impact of thermal noise on the phase-slippage is negligible.

We work at constant (negative) difference $\Delta\mu$ in the chemical potential between the reservoirs, so that the control parameter $\Phi^{\mathrm{L}}$ evolves linearly in time, according to the Josephson-Anderson relation:

$$\Phi^{\mathrm{L}} = -\Phi^{\mathrm{R}} = -\frac{\Delta\mu}{2\hbar}\,t. \tag{3.30}$$

As $\Phi^{\mathrm{L}} - \Phi^{\mathrm{R}}$ grows, so do the superfluid velocities through the various apertures, punctuated at regular intervals by velocity drops associated with phase-slip processes. As, beyond a brief transient interval, the total energy of the state is periodic in $\Phi^{L}$ with period $\pi$, the total current through the array must be a periodic function of time with period given by the Josephson frequency $\omega_{\mathrm{J}} = \Delta\mu/\hbar$. Due to the randomness in the critical velocities of the apertures, the velocities in the various apertures do not reach their critical values simultaneously. Thus, apertures having smaller critical velocities (i.e. weaker apertures) slip first.

We note that immediately after a phase slip in the $i^{\mathrm{th}}$ aperture the velocity through it is decreased by $\Delta v \equiv 2\pi\hbar/md$ (i.e. the quantum of superfluid velocity for an aperture having fixed phases at the openings), i.e. $v_i \to v_i - \Delta v$. However, after a very short time (on the order of time it takes sound to cross the array), the system equilibrates the superflow in the bulk reservoirs and through the various apertures. Therefore, after this relaxation process is complete, the net drop in the superfluid velocity through the $i^{\mathrm{th}}$ aperture is always less than $\Delta v$. To determine the configuration of the superfluid after a phase slip, we must increment $n_i$ to $n_i + 1$ in the description of the energy of the $i^{\mathrm{th}}$ aperture Eq. (3.13) (assuming all flow is to the left) and find the new set of values for all of the $\phi_i^{\mathrm{L}}$'s by minimizing the total energy, Eq. (3.16). This minimization results in a decrease of the supervelocity in the $i^{\mathrm{th}}$ aperture but an increase in the supervelocity in all of the other apertures, which pushes them closer to their own critical velocities.

If the distribution of critical velocities is sufficiently narrow, the array may—as we demonstrate shortly—suffer a system-wide avalanche (SWA). By an SWA we mean that when the weaker apertures (i.e. those having smaller critical velocities) slip, superflow through the neighboring apertures that have yet to slip increases, due to the inter-aperture interaction, and this drives them right up to their own $v_{\mathrm{c},i}$, thus causing a cascade of phase slips in which an appreciable fraction of the apertures in the array slip. Experimentally, SWAs would be reflected in a periodic series of sharp drops in the total current through the array of apertures,

$$I_{\mathrm{tot}} = \sum_{\mathrm{apertures}\, i} I_i, \tag{3.31}$$

as a function of time, where the current through a single aperture is given by Eq. (3.14). Time-traces of the total currents in the SWA and the disordered regimes are contrasted in Fig. 3.4.

We have used both numerics and a mean-field theory to analyze the "quasi-static" dynamics of the superflow. In addition, we have computed corrections to the mean-field theory in an expansion around the upper critical dimension 3 in powers of $\epsilon = d - 3$. For arrays having a small numbers of apertures, the quasi-static state of (mechanical) equilibrium may be determined numerically at each step, allowing for phase-slips whenever the flow velocity in an aperture exceeds its critical value, as the control parameter $\Phi^{\mathrm{L}}$ evolves parametrically. As a consequence of the long-range nature of the inter-aperture couplings $C_{ij}$, the array dynamics is well approximated by mean-field theory. Via this mean-field theory, we find a self-consistent equation for the average value $\langle \phi_i^{\mathrm{L}} \rangle$, in which the effective inter-aperture coupling enters through the parameter $B \equiv -\langle \sum_{j \neq i} C_{ij} \rangle$ and the effective self-interaction enters through $C \equiv \langle C_{ii} \rangle$, where $\langle \dots \rangle$ stand for an average over the apertures of the array. This self-consistent equation can have multiple solutions for certain values of $\Phi^{\mathrm{L}}$, which corresponds to the SWA regime, provided the disorder is sufficiently weak.

We begin, in subsec. 3.3.1, by describing a numerical procedure that defines the prescription for computing the (out of equilibrium) trajectories of the $\phi_i$'s as the control phase $\Phi^{\mathrm{L}}$ is slowly advanced. Next, in subsec. 3.3.2, we construct a mean-field theory of the model. In subsec. 3.3.3, we construct the renormalization group flows and the $\epsilon$-expansion, and discuss the implications for experiments in subsec. 3.3.10.

### 3.3.1 Numerical procedure

The numerics take as input: the effective aperture strength $J \equiv \pi r_0^2/d$, where $r_0$ is the aperture radius and $d$ the aperture thickness, and the (non-inverted) matrix $C_{ij}^{-1}$ [see Eq. (3.8b)], which itself depends on $r_0$, the inter-aperture spacing $l$, and the number of apertures in the array, $N \times N$. Before the numerical procedure begins, we choose a realization of the quenched disorder, i.e. a set of critical velocities $v_{\mathrm{c},i}$ for the various apertures drawn from the distribution of critical velocities. At each time-step, the control phase $\Phi^{\mathrm{L}}$ is incremented, and the new $\phi_i^{\mathrm{L}}$'s are obtained by minimizing the effective total energy $H$, Eq. (3.16). If the superflow through any aperture is found to now exceed its critical velocity, that aperture suffers a phase-slip (i.e. its value of $n_i$ is incremented by plus unity); next, the various $\phi_i^{\mathrm{L}}$'s are recomputed using the new set of $n_i$'s, and the program goes back to recheck if any other aperture now exceeds its critical velocity. This

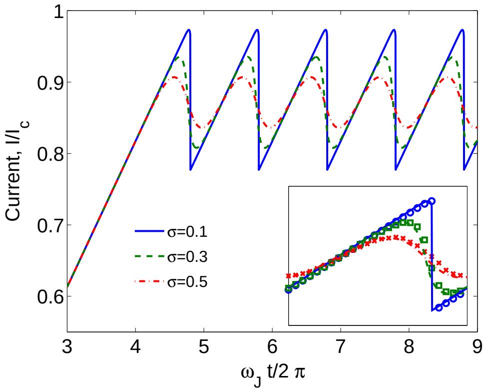

Figure 3.4: Total current through an array of apertures as a function of time, computed in mean-field theory, at various disorder strengths. The Gaussian distributions of critical phase-twists $\phi_{c,i}$ have widths $\sigma$ and means $\phi_c = 3\pi$. As the disorder strength is increased, the amplitude of the current oscillations decreases. The sharp drops in the current, which correspond to system-wide avalanches, disappear for $\sigma \gtrsim 0.2$. ($B = 0.10\,\mu$m; $C = 0.19\,\mu$m; $J = 0.01\,\mu$m; corresponding to $65 \times 65$ periodic array with $\ell = 3\,\mu$m, $r_0 = 15\,$nm, and $d = 50\,$nm.) Inset: Comparison between mean-field (solid lines) and exact calculation (dots).

continues until no new phase-slips are found to occur, at which point, we record the observables (i.e. the total current through the array, Eq. (3.31), and the avalanche size) at the given time, and then the control phase difference is incremented and the procedure is repeated.

### 3.3.2 Mean-field theory describing phase-slip dynamics

We now construct a mean-field theory. To do this, we assert that the control phase-difference is monotonically increasing in time, so that phase differences $\phi_i^{\mathrm{L}} - \phi_i^{\mathrm{R}} = 2\phi_i^{\mathrm{L}}$ are always increasing and the superflow in the apertures undergoes only $n_i$-increasing phase slips. We proceed by selecting an arbitrary aperture $i$ and minimizing the effective total energy $H$ with respect to $\phi_i^{\mathrm{L}}$ we obtain:

$$0 = \frac{\partial H}{\partial \phi_i^{\mathrm{L}}} = K_s \left( \sum_j C_{ij}(\phi_j^{\mathrm{L}} - \Phi^{\mathrm{L}}) + 2J(2\phi_i^{\mathrm{L}} - 2\pi n_i) \right). \tag{3.32}$$

Replacing the $\phi_{j(\neq i)}^{\mathrm{L}}$'s by the mean-field value $\langle \phi^{\mathrm{L}} \rangle$ we obtain the mean-field equation for the phase at the $i^{\mathrm{th}}$ aperture:

$$\phi_i^{\mathrm{L}}(C + 4J) - B\langle \phi^{\mathrm{L}} \rangle = A\Phi^{\mathrm{L}} + 4\pi J\, n_i, \tag{3.33}$$

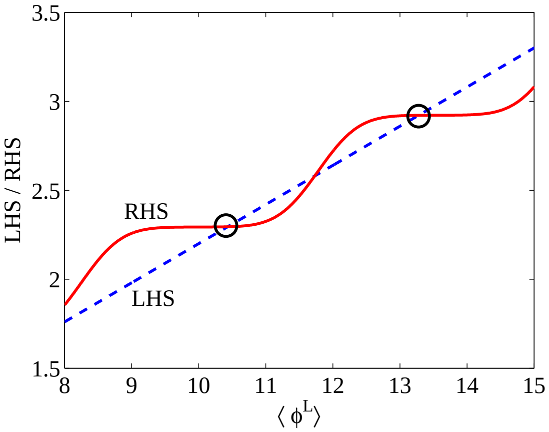

Figure 3.5: Left- and right-hand sides of the averaged form of Eq. (3.33). The circles indicate the two main solutions: as the control-phase is increased, the RHS curve moves up and to the left, such that there is a discontinuous jump from one solution to the other corresponding to an avalanche.

where $B \equiv \langle B_i \rangle = -\langle \sum_{j \neq i} C_{ij} \rangle$, $C \equiv \langle C_{ii} \rangle$, $A \equiv C - B$, and $\langle \dots \rangle$ stand for averages over sites $i = 1, \dots, N^2$. (The necessary inversion of $C_{ij}^{-1}$ can be accomplished either analytically, by transforming to Fourier space, or numerically.) By averaging the left- and right-hand sides of Eq. (3.33) over sites we arrive at a self-consistency condition on $\langle \phi^{\mathrm{L}} \rangle$:

$$\langle \phi^{\mathrm{L}} \rangle = \frac{A\Phi^{\mathrm{L}} + 4\pi J \langle n \rangle}{A + 4J}. \tag{3.34}$$

Next, by assuming self-averaging with respect to the disorder in the critical velocities, we may replace the average over sites by an average over disorder. By using Eq. (3.33), together with the distribution of critical half-phase twists $Q(\phi_c)$, we obtain an expression for $\langle n \rangle$ which itself depends on $\Phi^{\mathrm{L}}$ and $\langle \phi^{\mathrm{L}} \rangle$:

$$\langle n \rangle(\langle \phi^{\mathrm{L}} \rangle) = \sum_{k=0}^{\infty} k \int_0^{\infty} d\phi_c \, Q(\phi_c) \left[ \Theta\left( \phi_c - \frac{A\Phi^{\mathrm{L}} + B\langle \phi^{\mathrm{L}} \rangle - \pi k \, C}{C + 4J} \right) - \Theta\left( \phi_c - \frac{A\Phi^{\mathrm{L}} + B\langle \phi^{\mathrm{L}} \rangle - \pi(k-1)C}{C + 4J} \right) \right], \tag{3.35}$$

where $\phi_c$ is related to the critical velocity $v_c$ via $\phi_c \equiv dmv_c/\hbar$, where $d$ is the aperture length and $m$ is the mass of a ${}^4$He atom. Equation (3.34) can be solved graphically, by plotting the left- and right-hand sides as functions of $\langle \phi^{\mathrm{L}} \rangle$; see Fig. 3.5. It is evident from this graphical approach that whenever the maximum slope of the right-hand side, $4\pi J \partial \langle n \rangle / \partial \langle \phi^{\mathrm{L}} \rangle$ *fails* to exceed the slope of the left-hand side, $(A + 4J)\langle \phi^{\mathrm{L}} \rangle$, the self-consistency condition yields a unique solution for the average phase $\langle \phi^{\mathrm{L}} \rangle$, and that this phase evolves continuously with the (increasing) control phase $\Phi^{\mathrm{L}}$. This corresponds to the non-avalanching regime. By contrast, whenever the maximum slope of the right-hand side *does* exceed the slope of the left-hand side,

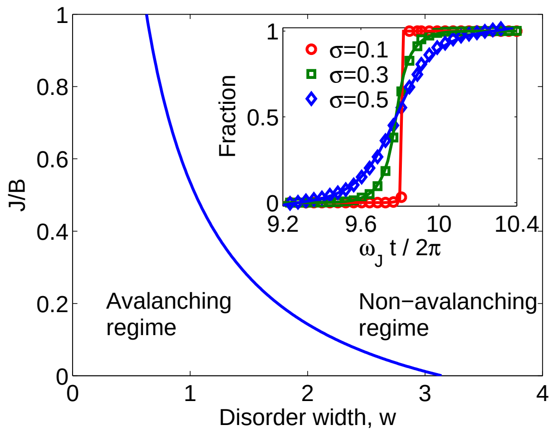

Figure 3.6: Phase diagram, showing avalanching and non-avalanching regimes of the phase-slip dynamics, as a function of the effective aperture strength $J/B$ and the disorder strength $w$. The diagram was computed via our mean field theory, in the large-array limit (i.e. $C \simeq B$), with a uniform critical phase twist (or, equivalently, the critical velocity) distribution of width $w$, see Eq. (3.36). *Inset:* The fraction of apertures that have phase slipped, as a function of the control-parameter $\omega_J t = (\Phi^L - \Phi^R)$. Comparison between numerics for a $65 \times 65$ array of apertures (points) and our mean-field theory (lines) with Gaussian distribution of critical phase twists. The transition from avalanching to non-avalanching regime is evident, as the width $\sigma$ of the Gaussian is increased.

the self-consistency condition no longer yields a unique solution for $\langle \phi^{\mathrm{L}} \rangle$. Instead, as the control-phase is increased, the continuous evolution of $\langle \phi^{\mathrm{L}} \rangle$ is punctuated by jumps, which occur when pairs of solutions merge and disappear. These jumps reflect avalanching behavior, and we refer to this as the avalanching regime.

To test the results of the mean-field theory, we have compared its current-vs.-time traces with those obtained from an exact numerical investigation performed on a finite lattice of nano-apertures. The lattice was chosen to be translationally invariant by selecting the distance function between between two apertures to be the shortest distance on the torus [2]. The current-vs.-time curves, computed for various widths of the disorder distribution, are shown in the inset of Fig. 3.4. In the numerics, avalanches occur only when the distribution of critical velocities is narrower than the critical value of disorder width $\sigma_c$ as obtained from mean-field theory.

We can use our mean-field theory to construct a phase diagram that demarcates the SWA and the disordered regimes, for any choice of disorder distribution $Q(\phi_c)$ of critical phase twists. For the case of a normal distribution of width $\sigma$, a simple inequality determines the SWA regime:

$$\sigma \leq \sigma_{\mathrm{c}} \equiv \frac{2\sqrt{2\pi} J B}{(C - B + 4J)(C + 4J)}, \tag{3.36}$$

---

[2] The distance function is not periodic, in the sense that we did replicate the array of apertures in a periodic arrangement.

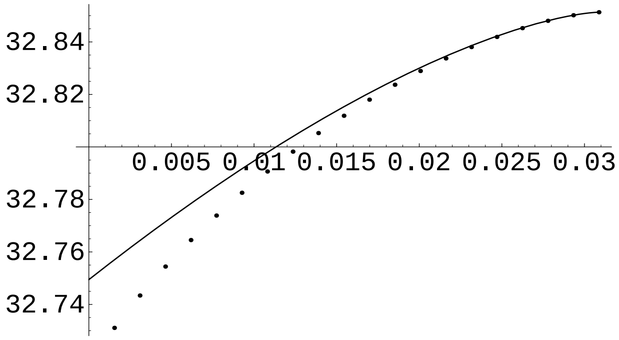

Figure 3.7: $\Phi_c(\sigma)$ line terminating at the critical point $\sigma = \sigma_c$, comparing exact solution of the mean-field equation (dots) to the power law (solid line). $A = 0.16$, $B = 0.02$, $J = 0.1$, $\phi_c^0 = 3\pi$.

where $\sigma_c$ is the critical width of the distribution; such a phase boundary is exemplified in Fig. 3.6. At a critical strength of the disorder, the discontinuity in the mean-field super-current vs. time plot caused by a SWA event vanishes.

The two main results of our mean-field theory are summarized in Fig. 3.8. The dashed curve in the right pane shows the amplitude of the *current oscillation* $I_{\text{slip}}$ (i.e. half the distance between smallest and largest current during a single period, left pane Fig. 3.8) vs. the disorder strength. As the disorder becomes stronger, the phase-slips in the various apertures become less synchronous, and the oscillations in the current gradually disappear. The solid curve shows $I_{\text{drop}}$, (half) the *current-drop* caused by SWA (i.e. half the height of the vertical drop in current, left pane Fig. 3.8) vs. the disorder strength. The current-drop plays the role of an order parameter for a second-order phase transition that is tuned by the strength of the disorder. As the disorder becomes stronger, the order parameter decreases, becoming zero at a critical disorder strength ($\sigma_c \approx 0.2$), corresponding to a transition from the SWA to the disordered regime.

We can also construct a phase diagram in the control phase-vs.-disorder (i.e. $\Phi$ vs. $\sigma$) plane; see Fig. 3.7. On this diagram the points indicates the values of $\Phi^{\text{L}}$ for a given $\sigma$ at which SWAs occur. Note, that the graph is periodic in $2\Phi^{\text{L}}$, with period $2\pi$, corresponding to all apertures phase-slipping exactly once. The line of (first-order) phase-transitions terminates at the (second order) critical end point $\sigma = \sigma_c$. We shall analyze the model two regimes: (1) in the vicinity of this line and (2) in the vicinity of the critical end point at $\sigma_c$. We begin by obtaining the various scaling relations within our mean-field theory. These results, which we list here, are a direct adaptation of those obtained in Ref. [77]. The detailed derivations are given in Appendix E.

Away from the SWA, the un-normalized avalanche size distribution, $D(S)$, within mean-field theory, has the form

$$D(S) \approx \frac{1}{S^{3/2}\sqrt{2\pi}} e^{-St^2/2}, \tag{3.37}$$

where $S$ is the size of the avalanche and $t$ is the average number of apertures triggered by the phase-slip in initial aperture minus one. Exactly at the critical end-point or on the first-order line we have $t = 0$, and there the avalanche size distribution follows a $-3/2$ power law, i.e. the probability to find an avalanche of size $S$ is $D(S) = S^{-3/2}$.

We shall first concentrate on the vicinity of the critical point at $\sigma_c$. For $\sigma < \sigma_c$, the size of SWAs as a fraction of the total number of apertures scales as $|r|^{1/2}$, where $r = (\sigma - \sigma_\mathrm{c})/\sigma_\mathrm{c}$ is the distance to the critical point. Furthermore, the first-order line $\Phi_c(\sigma)$ depicted in Fig. 3.7 has the shape given by

$$\Phi_c(\sigma) - \Phi_c(\sigma_c) = -\frac{8BJ\sqrt{\pi}}{3A(C+4J)}|r|^{3/2}. \tag{3.38}$$

Finally, at the critical end-point the average phase twist at the apertures (which plays the role of the average magnetization) has a universal scaling form:

$$\langle\phi\rangle - \langle\phi\rangle_c \sim r^{1/2} y\left(\frac{\Phi - \Phi_c}{r^{3/2}}\right), \tag{3.39}$$

where $y(s)$ is the real root of

$$y^3 + 6y - \frac{3A(C+4J)}{\sqrt{2\pi}BJ}s = 0. \tag{3.40}$$

On the other hand in the vicinity of the first-order line, the average phase twist at the apertures has the following simple scaling relation

$$\langle\phi\rangle - \langle\phi\rangle_c \sim (\Phi - \Phi_c)^{1/2}. \tag{3.41}$$

### 3.3.3 Renormalization group analysis via $\epsilon$-expansion

In this section, we would like to find corrections to the mean-field-theory results. We use the approach developed by Narayan and Fisher [86, 87] to study the motion of charge density waves (CDWs) in the presence of a random pinning potential. Their approach is based on the Martin-Siggia-Rose (MSR) dynamical field theory formalism [88], and allows one to perform averages over disorder in the pinning potential by

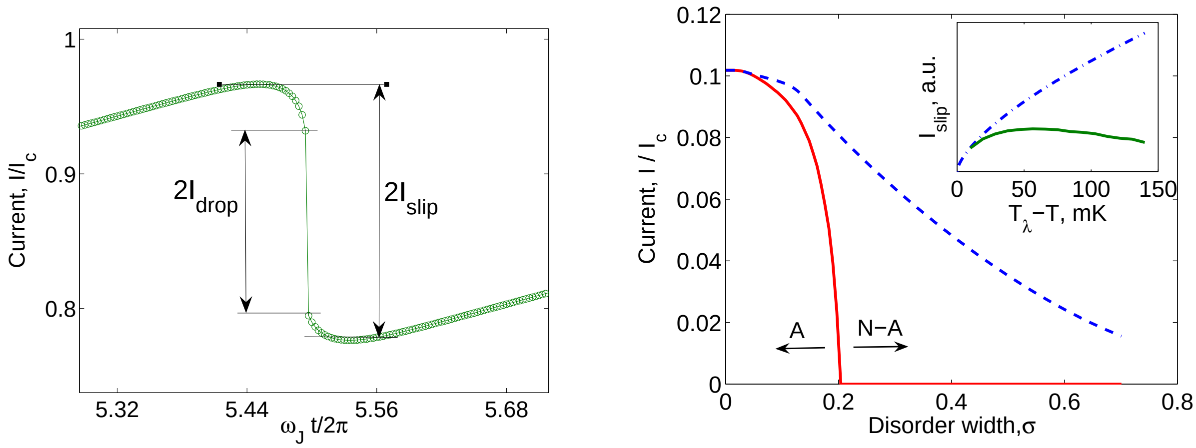

Figure 3.8: Left: Total current vs. time plot illustrating (i) $I_{\rm slip}$ the amplitude of the oscillations of the current, and (ii) $I_{\rm drop}$ the amplitude of the drop in current due to an SWA. Right: $I_{\rm slip}$ (dashed line), and $I_{\rm drop}$ (solid line), as functions of the disorder strength. A and N-A indicate the SWA and disordered regimes, respectively. *Inset:* Solid line: amplitude of the oscillation of the current, as a function of temperature, using the 'effective disorder' model described in the text Eq. (3.77). Dashed line: ideal amplitude, for the case of perfectly synchronous phase-slippage, corresponding to the absence of disorder- and edge-driven inhomogeneity.

converting the equations of motion for the CDW into a field theory. The Narayan-Fisher approach was successfully used to study the properties of the random field Ising model (RFIM) by Sethna and Dahmen co-workers [89, 90]. The RFIM turns out to be closely related, at least formally, to the problem of interacting phase-slips that we wish to study. In fact, up to minor differences in notation, we find that at the mean-field level the problems are equivalent in that the have identical critical exponents. Therefore, to make progress in our problem beyond the level of mean-field-theory we start with the analysis of the RFIM, as presented in Dahmen's thesis [77], and adapt it to our case. The most significant change is the replacement of the nearest-neighbor interaction, studied by Dahmen [77], by the long range interaction that appropriately characterize our problem.

In this section, we first give a brief introduction to the problem of pinning charge density waves. Next, we give a more in-depth survey of the RFIM, concentrating on the 'soft-spin' version of the model. In the soft-spin version, the two-state Ising spins are replaced by continuously-varying degrees of freedom moving in a double well potential that simulate the two discrete Ising states. We identify a connection between this soft-spin version of the RFIM and our model of interacting phase-slips. We continue by following Ref. [77] to outline the Narayan-Fisher approach to the MSR formalism, obtain a saddle-point expansion about the mean-field solution and, finally, the renormalization-group equations. We find that for the problem of interacting phase-slips with long-range interactions, the upper critical dimension is *three* (in contrast with the value of *six* for the nearest-neighbor case considered for the RFIM). Next, we identify the various fixed points and obtain the corresponding critical exponents.

### 3.3.4 Pinning of charge density waves

In many, especially lower-dimensional, systems, due the interaction between electrons and phonons, the discrete lattice translational invariance may be spontaneously broken giving rise to a CDW, i.e., a periodic modulation of the electron density accompanied by lattice deformations. This mechanism is known as the Pierel's instability. In some CDW systems the modulation of the electron density is commensurate with the underlying lattice, which typically leads to the locking of the modulation to the lattice. Others, however, are incommensurate with the underlying lattice and thus, in principle, are energetically free to slide through the lattice. Narayan-Fisher concentrate on the incommensurate CDWs, and study the pinning of this sliding motion by impurities within the lattice. They describe the CDW by a collection of phases of the periodic lattice distortion associated with the CDW specified at the sites of a lattice $\phi_i$. The dynamics of these phases are modeled via the equation of motion

$$\frac{\partial \phi_j}{\partial t} = -\frac{\partial H}{\partial \phi_j} = \sum_i J_{ij}(\phi_i - \phi_j) - \frac{dV_j}{d\phi_j} + F, \tag{3.42}$$

where $J_{ij}$ describes the interaction between phases at site $i$ and $j$ (that are generally taken to be nearest-neighbor), $V_j$ is the *random* pinning potential for the $j^{\text{th}}$ site (for the case of CDWs, $V_j$ is a random but periodic in $\phi_j$ potential, having a random amplitude and phase-shift on the various sites of the lattice), and $F$ is a driving force (due, e.g., to an external electric field) that pushes the CDW forward (i.e. to higher values of $\phi_i$). When the externally-applied force is sufficiently large, the CDW suffers the so-called depinning transition and starts sliding. The form of the equation of motion describing CDWs is very general and, in fact, can also be used to describe both the soft-spin version of the RFIM and the present problem of interacting phase-slips. The main differences between the three problems arise from the form and range of the interaction $J_{ij}$ and the form of the pinning potential $V_j$.

### 3.3.5 Soft-spin random field Ising model

The RFIM is a model designed to capture the essential properties of realistic magnets, in particular how the magnetization changes, in a history dependent way, as the externally-applied magnetic field is varied. Like the standard Ising model, the RFIM is composed of interacting spins in an external magnetic field. Each spin $j$ has a magnetic moment $s_j$ that can be in one of two states, $s_j = \pm 1$, and the interaction is assumed to be nearest-neighbor and ferromagnetic (i.e. favoring alignment of spins $i$ and $j$). In addition to the externally-applied magnetic field $F$, associated with each domain is a local random field $f_i$.

Unlike the standard Ising model, in this context we treat the RFIM not as a thermodynamic model but instead as a non-linear dynamics model. Therefore, instead of weighting states using Boltzmann factors, we look at the dynamics of the spins. The dynamics are described by the following rules: One imagines beginning with an external field $F$ so large that all the Ising spins are aligned with it. Next, one imagines slowly change $F$, and whenever the local field $F_j$, where

$$F_j = F + \sum_{i(\neq j)} J_{ij} s_j + f_j, \tag{3.43}$$

acting on a particular Ising spin $s_j$, changes sign, the Ising spin flips so as to remain aligned with the local field. When a spin flips, the neighbors of the spin that has flipped encounter a change in their local field $F_i$. This change in the local field of the neighboring spins can induce one or more of them to flip. If the distribution of the random fields $f_i$ is sufficiently narrow, the initial spin flip may launch a cascade of secondary spin-flips, and this is called an avalanche.

The dynamics of the RFIM cannot be (easily) written in the form of Eq. (3.42) due to the discrete nature of the Ising spins. Therefore, it is convenient to study the soft-spin version of the RFIM, in which the Ising spins $S_j$ are replaced by the continuous variables $\phi_j$. The $\phi_j$'s are subject to move in the potentials

$$V_j = \begin{cases} k/2(\phi_j + 1)^2 - \phi_j f_j; & \text{for } \phi_i < 0, \\ k/2(\phi_j - 1)^2 - \phi_j f_j; & \text{for } \phi_i > 0, \end{cases} \tag{3.44}$$

where, as before, $f_j$ is the random local field. This form of the potential serves two purposes: (1) its two minima simulate the two Ising states, and (2) it captures the effect of the random local field $f_j$ by shifting the relative energy of the two minima. The dynamics of these soft-spins are described by the equation of motion Eq. (3.42), with $V_j$ specified by Eq. (3.44), and $J_{ij} = 1/z$ if $i$ and $j$ are nearest neighbors and $J_{ij} = 0$ otherwise, where $z$ is the coordination number of the lattice (e.g. six for a three-dimensional square lattice).

### 3.3.6 Connection between the random field Ising model and the present model of interacting phase-slips

We begin by considering an equation of motion that would capture the properties of the model of interacting phase-slips. That is, we would like to identify an equation of motion for the phases across the apertures that would reproduce the trajectories that we obtain when the system follows the rules described in subsec. 3.3.1.

In the limit of an adiabatically-slowly varying control-phase $\Phi$, the solution of the equation of motion

$$\frac{\partial \phi_j}{\partial t} = -\frac{\partial H}{\partial \phi_j}, \tag{3.45}$$

where $H$ is the total energy that appears in Eq. (3.16), will, indeed, trace out trajectories identical to those obtained by the rules described in subsec. 3.3.1.

To make a connection with the RFIM, we write down the equation of motion explicitly for the problem of interacting phase-slips:

$$\frac{\partial \phi_j}{\partial t} = \sum_{i(\neq j)} C_{ij}\phi_i + \Phi \sum_j C_{ij} - J\left(\phi_j - \pi \sum_{k=0}^{\infty} \theta(\phi_j - \phi_{c,j} - \pi k)\right), \tag{3.46}$$

where $\theta(\cdot)$ is the unit step function, and $\phi_{c,i}$ is the random, aperture-specific, critical phase-twist, and, crucially, we continue working under the assumption that all the apertures have phase slipped either $n$ or $n+1$ times[3]. Next, we compare this equation of motion to the one obtained for the RFIM:

$$\frac{\partial s_j}{\partial t} = -2\sum_{i(\neq j)} J_{ij}s_i + f_j + F - ks_j + 2k\left(\theta(s_j) - \frac{1}{2}\right). \tag{3.47}$$

The identification between the two equations of motion is made explicit via the following transformations:

$$C_{ij} = -2J_{ij}, \tag{3.48}$$

$$\Phi \sum_j C_{ij} = F, \tag{3.49}$$

$$s_j = \phi_j - \phi_{c,j} \tag{3.50}$$

$$\phi_{c,j} = (2J_{ij} + k\delta_{ij})^{-1} f_i. \tag{3.51}$$

With these transformations, we map the problem of interacting phase-slips on to a version of the RFIM, the only difference being the substitution of long- for short-range interactions.

Having made this identification, we proceed by developing the MSR formalism for a generic equation of motion, and make the restriction to this specific form only when it becomes necessary for the computation of the coefficients in the expansion about the saddle-point.

---

[3] We have ignored the (inconsequential) $\delta$ functions that arise when taking the derivative of the $\theta$ functions in the pining potential.

### 3.3.7 Martin-Siggia-Rose formalism

The basic idea is to convert the description of dynamics based on the equation of motion, Eq. (3.42), into a description involving an integral over histories. This is accomplished via the MSR formalism, which provides a way to write a path integral that, for a given initial conditions and disorder, selects only the single path that obeys the equation of motion. Consider introducing the partition function $Z$ via

$$1 = Z = \int [d\phi][d\hat{\phi}] J[\phi] \exp \Bigg\{ i \sum_i \int dt\, \hat{\phi}_i \left( \frac{\partial \phi_i}{\partial t} + \frac{\partial H}{\partial \phi_i} \Bigg\} \Bigg] , \tag{3.52}$$

where $J[\phi]$ is a functional Jacobian determinant that ensures that the partition function is indeed unity by guaranteeing that all of the $\delta$-functions integrate to unity. The form of $J[\phi]$ depends on the definition of the path integral, in the sense of discretization in time, and we shall adopt the one for which the correct value is $J[\phi] \equiv 1$. Upon performing the path-integral over $\hat{\phi}$, we obtain a $\delta$-function that selects only that path that satisfies the equation of motion. One advantage of the MSR formalism is that one does not have to deal with a random denominator when computing observables; this is because $Z \equiv 1$, independent of the randomness.

### 3.3.8 Saddle-point expansion

Narayan and Fisher continue by introducing the disorder-averaged partition function $\bar{Z}$:

$$1 = \bar{Z} = \int [d\phi][d\hat{\phi}] \left\langle \exp \left[ i \sum_i \int dt\, \hat{\phi}_i \left( \frac{\partial \phi_i}{\partial t} + \frac{\partial H}{\partial \phi_i} \right) \right] \right\rangle \tag{3.53}$$

where $\langle \cdots \rangle$ stands for the disorder average. Next, following Sompolinsky and Zippelius [91], Narayan and Fisher introduce the conjugate fields $\Phi$ and $\hat{\Phi}$. The goal of this transformation is to separate the disorder average and the inter-site interaction through the introduction of an axillary field, which allows us to carry out the disorder averages on different sites independently. Upon the introduction of the conjugate fields, the disorder-averaged partition function becomes

$$\bar{Z} = \int [d\Phi][d\hat{\Phi}] \prod_j \bar{Z}_j[\Phi_j, \hat{\Phi}_j] \exp \left\{ - \int dt\, \hat{\Phi}_i {J^{-1}}_{ij} \Phi_j \right\} , \tag{3.54}$$

where $\bar{Z}_j[\Phi_j, \hat{\Phi}_j]$ is a path integral over the fields $\phi_j$ and $\hat{\phi}_j$ on a single site only

$$\bar{Z}_j[\Phi_j, \hat{\Phi}_j] = \int [d\phi][d\hat{\phi}] \Bigg\langle \exp \Bigg\{ \int dt \Bigg[ \hat{\Phi}_j \phi_j + i \hat{\phi}_j \left( \partial_t \phi_j - \Phi_j + \phi_j + \frac{\partial \widetilde{H}}{\partial \phi_j} \right) \Bigg] \Bigg] \Bigg\} \Bigg\rangle , \tag{3.55}$$

and $\widetilde{H}$ is the energy without the $J_{ij}$ term. If we were to integrate over the conjugate fields, $\Phi$ and $\hat{\Phi}$, we would recover the original partition function, Eq. (3.53). The introduction of the conjugate fields allows us to perform a perturbative expansion not about the trivial point ($\Phi = \hat{\Phi} = 0$), but rather about the mean-field solution, which corresponds to the saddle-point of the action in Eq. (3.54). To find this saddle-point, we vary this action with respect to $\Phi_j$ and $\hat{\Phi_j}$, thus obtaining the following equations for the location ($\Phi_j^0$ and $\hat{\Phi}_j^0$) of the saddle point:

$$-J_{ij}^{-1}\hat{\Phi}_i^0 - i\langle\hat{\phi}_j\rangle_{l,\hat{\Phi}^0,\Phi^0} = 0, \tag{3.56}$$

$$-J_{ij}^{-1}\Phi_i^0 + \langle\phi_i\rangle_{l,\hat{\Phi}^0,\Phi^0} = 0, \tag{3.57}$$

where $\langle\ldots\rangle_l$ stands for the local (i.e. single-site) average over the disorder, computed with $\eta$ and $\hat{\eta}$ fixed at their mean-field values, that is

$$\langle\hat{\phi}_j\rangle_{l,\hat{\Phi}^0,\Phi^0} = i\left.\frac{\partial\bar{Z}_j[\Phi_j,\hat{\Phi}_j]}{\partial\Phi_j}\right|_{\hat{\Phi}^0,\Phi^0}, \tag{3.58}$$

$$\langle\phi_j\rangle_{l,\hat{\Phi}^0,\Phi^0} = \left.\frac{\partial\bar{Z}_j[\Phi_j,\hat{\Phi}_j]}{\partial\hat{\Phi}_j}\right|_{\hat{\Phi}^0,\Phi^0}. \tag{3.59}$$

$$\tag{3.60}$$

By solving Eqs. (3.56, 3.57) we obtain the self-consistent form

$$\hat{\Phi}_j^0 = 0, \tag{3.61}$$

$$\Phi_j^0 = M(t) = \langle\phi_j\rangle_{l,\hat{\Phi}^0,\Phi^0}, \tag{3.62}$$

where $M(t)$ is the disorder-averaged solution of the mean-field equation of motion

$$\partial_t\phi_j = M(t) - \frac{\partial\widetilde{H}}{\partial\phi_j}. \tag{3.63}$$

We are now in a position to perform an expansion about the saddle point. We begin by introducing the (shifted) variables $\eta_j$ and $\hat{\eta}_j$, which measure the deviation from the saddle point solution:

$$\eta_j \equiv \Phi_j - \Phi_j^0, \qquad \hat{\eta}_j \equiv \hat{\Phi}_j - \hat{\Phi}_j^0. \tag{3.64}$$

Next, we express the partition function in terms of these variables:

$$\bar{Z} = \int [d\eta][d\hat{\eta}] \exp S_{\text{eff}}, \tag{3.65}$$

where,

$$S_{\text{eff}} = -\int dt \sum_{i,j} \hat{\eta}_i(t) J_{ij}^{-1} \eta_j(t) \tag{3.66}$$

$$+ \sum_j \sum_{m,n=0}^{\infty} \frac{1}{m!\,n!} \int dt_1 \dots dt_{m+n}\, u_{m,n}(t_1, \dots, t_{m+n})\, \hat{\eta}_j(t_1) \dots \hat{\eta}_j(t_m) \eta_j(t_{m+1}) \dots \eta_j(t_{m+n}), \tag{3.67}$$

and

$$u_{m,n} = \left( \frac{\partial}{\partial \eta_j(t_{m+1})} \cdots \frac{\partial}{\partial \eta_j(t_{m+n})} \right) \left( \frac{\partial}{\partial \hat{\eta}_j(t_1)} \cdots \frac{\partial}{\partial \hat{\eta}_j(t_m)} \right) \left( \log \bar{Z}_j - \hat{\eta}_j(t) \Phi_j^0 \right)_{\hat{\eta}=0, \eta=0}. \tag{3.68}$$

The values of the coefficients $J_{ij}$ and $u_{m,n}$ depend on the specific model. At this point we refocus on the soft-spin RFIM model with long-range interactions, which we have shown to be identical to the interacting phase-slips model. In particular, we set $J(q)$, the Fourier transform of $J_{|i-j|}$, to be $J(q) = 1/|q|$ which corresponds to $J_{|ij|} \sim 1/|r_{ij}|^3$. The various coefficients $u_{m,n}$ can be read of from the short range soft-spin RFIM as they arise from the properties of the single site action, and therefore are independent of $J_{ij}$.

If we keep the (non-zero) vertices of lowest order in $\eta$, labeled $u_{1,1} = w$, $u_{2,0}$ and $u_{1,3} = u$, the effective action $S_{\text{eff}}$ becomes

$$S_{\text{eff}} = -\int dt \int đq\, \hat{\eta}(-q, t) \left[ -a \frac{\partial_t}{\Gamma_0} + |q| - w \right] \eta(q, t) \tag{3.69}$$

$$+ \frac{1}{2} \int dt_1\, dt_2 \int đq\, u_{2,0} \hat{\eta}(-q, t_1) \hat{\eta}(q, t_2) \tag{3.70}$$

$$+ \frac{1}{6} \int dt \int đq_1\, đq_2\, đq_3\; u\, \hat{\eta}(q_1, t) \eta(q_2, t) \eta(q_3, t) \eta(-q_1 - q_2 - q_3, t). \tag{3.71}$$

Here, $đq \equiv d^d q/(2\pi)^d$ and we keep only the terms that will be relevant to the renormalization-group calculation in the next subsection. This expression for $S_{\text{eff}}$ differs from the one occurring in Ref. [77] only inasmuch as the long-range interactions causes the $q^2$ term to be replaced by the $|q|$ term. From the point of view of the analysis of fluctuations this is an important and consequential modification that gives rise to a new set of critical exponents.

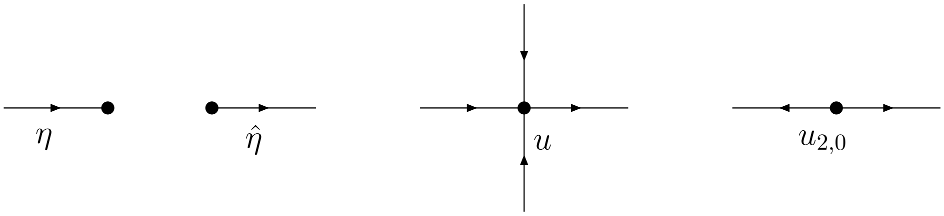

Figure 3.9: Vertices associated with the effective action, Eq. (3.71).

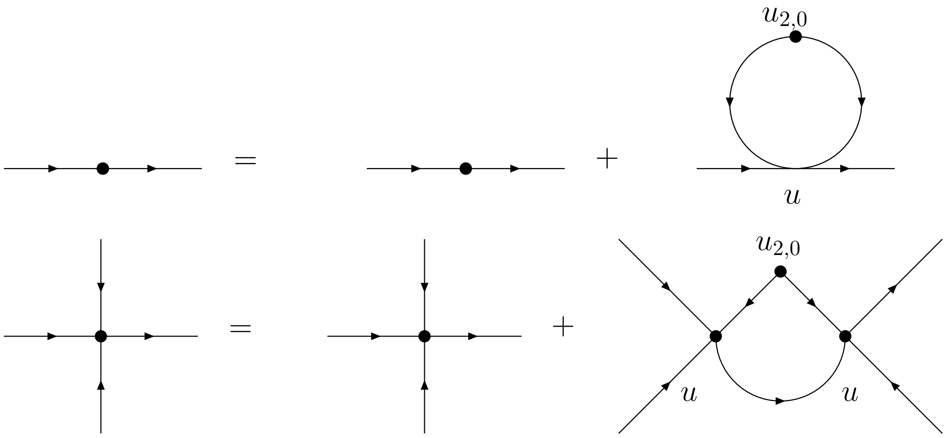

Figure 3.10: Feynman diagrams for the renormalization group at one loop order.

### 3.3.9 Renormalization-group analysis

In this subsection we perform the renormalization-group transformation in two parts: In part (i) we integrate out the fields $\hat{\eta}$ and $\eta$ that have high Fourier components; that is, we trace over the fields $\eta(q,t)$ and $\hat{\eta}(q,t)$ for which $\Lambda/b < q < \Lambda$, where $\Lambda$ is the high-momentum cut-off and $b$ determines the coarse graining. In part (ii) we rescale length by $b^{-1}$ to bring the effective action back to its original form but with rescaled coefficients. Before systematically performing these steps, we pause to identify the dimensions of the various fields and coefficients and obtain the naive scaling relations.

Comparing the first and second term in Eq. (3.71), we find that with no loop corrections $z = 1$. From dimensional analysis we identify the following naive scaling relations:

$$q' = b^{-1}q, \qquad t' = bt, \tag{3.72}$$

$$\hat{\eta}' = b^{C_{\hat{p}}}\hat{\eta}, \qquad \eta' = b^{C_p}\eta, \tag{3.73}$$

where $C_p = d/2 + 1$ and $C_{\hat{p}} = d/2 - 1$. Having identified the scaling relations of the coordinates and the fields, we can compute the naive scaling relation for an arbitrary vertex:

$$u'_{m,n} = b^{(2-(m+n))d/2+n} u_{m,n}. \tag{3.74}$$

From this relation, we see that for $d > 4$ all super-quadratic vertices are irrelevant. Below four dimensions, the first vertex to become relevant is $u_{1,2}$. However, at the critical end-point, $\sigma = \sigma_c$, that we are interested in $u_{1,2} \equiv 0$. Therefore, we must look at the next most relevant non-zero vertex $u_{1,3}$. From Eq. (3.74), we see that $u_{1,3}$ is relevant in less than three dimensions.

Next, we perform the renormalization-group transformation and find the scaling relations to one-loop order. The diagrams involved in tracing out the high momentum modes to this order are shown in Fig. 3.10. At this order, $u_{2,0}$ is found to be fixed, while both $w$ and $u$ are found to flow at both the tree-level and with one-loop corrections (see Fig. 3.10). The details of this calculations closely follow Chapter 7 of Ref. [77] and are provided in Appendix F. The resulting flow equations are

$$v' = v + v \log(b) \left( \epsilon + \frac{3v}{2\pi^2} \right), \tag{3.75}$$

$$w' = b \left( w + \frac{v}{2} \frac{1}{2\pi^2} \left[ \Lambda \left( 1 - \frac{1}{b} \right) + 2w \log b \right] \right), \tag{3.76}$$

where $v = uu_{1,2}$. As described in Appendix F, these flow equations have two fixed points, the Gaussian fixed point located at $v = 0$ and $u = 0$ and the Wilson-Fisher fixed point $v = -\frac{2\pi^2}{3}\epsilon$ and $w = \frac{\epsilon\Lambda}{6}\frac{1}{1-\epsilon/3}$.

The properties of the system near criticality, in particular the critical exponents, may be obtained from the analysis of the linearized flow equations in the vicinity of the fixed points, see Appendix F. For $d > 3$, the Gaussian fixed point has one stable and one unstable eigendirection while the Wilson-Fisher fixed point has two unstable eigendirections. Therefore the Gaussian fixed point controls the flows, and we can read off the correlation length critical exponent $\nu$ from the unstable eigenvalue of the Gaussian fixed point $\nu = 1/y_t = 1$. On the other hand for $d < 3$, the situation is reversed and the Gaussian fixed point has two unstable eigendirections, while the Wilson-Fisher fixed point has one stable and one unstable eigendirection, and the correlation length critical exponent becomes $\nu = 1/y_t = 1 + \epsilon/3$.

### 3.3.10 Implications for experiment

In their experiments [65], the Berkeley group measured the amplitude of the "whistle" (i.e. the amplitude of the current oscillations $I_{\text{slip}}$) as a function of temperature at a fixed chemical potential difference. These experiments found an onset of current oscillations at $T_\lambda$. As the temperature was lowered below $T_\lambda$, $I_{\text{slip}}$

begins by increasing from zero, and then decreases gradually. To obtain the temperature dependence of $I_{\mathrm{slip}}$, we consider the origin of the disorder in the critical velocities, which we have until now been treating as a completely phenomenological parameter. Thus, we extend the model for the critical velocity, Eq. (3.15), to include the effect of disorder by hypothesizing that

$$v_{c,i}(T) \simeq \frac{\hbar}{m\xi(T)} \left(1 + \frac{x_i}{r_0}\right), \tag{3.77}$$

where $x_i$ is a single, temperature-independent length, characterizing surface roughness in the $i^{\mathrm{th}}$ aperture, and we take it to have a Gaussian distribution. For $T_\lambda - T > 10\,\mathrm{mK}$, we can compare the results of our model to those of the experiments. The general features are reproduced: the initial increase in $I_{\mathrm{slip}}$ is associated with an increase in the superfluid fraction; the gradual decrease at lower temperatures is due to the loss of synchronicity amongst the apertures, which is caused by the effective increase in the strength of the disorder. To demonstrate these features, we plot the amplitude of the current oscillations vs. temperature; see the inset in Fig. 3.8, for which we have used a Gaussian distribution of $x_i$'s of standard deviation $\sigma_x = 0.6\,\mathrm{nm}$.

We also note that the general features of the current-*vs.*-time traces, Fig. 3.4, are similar to those of the Type III experiments described in Ref. [65]. In both, as the temperature is lowered (i.e. the disorder is increased), the avalanche gradually disappears, and then so do the oscillations in the current.

### Thermal fluctuations

Thermal fluctuations of the phases can wash out the disorder-driven phase transition if they exceed the width of the disorder distribution, and if they are sufficiently strong they can also wash out the "whistle." The main mechanism by which thermal fluctuations act is by causing random premature phase slips before the critical velocity is reached. Thus, the thermal fluctuations effectively broaden the width of the critical velocity distribution. As suggested by Sato [92], we can model this effect by a stochastic approach in which we choose a new critical velocity for an aperture that has just phase slipped from a distribution specific to that aperture, where the distribution describe both thermal effects and physical properties of the aperture. That is for the $i^{\mathrm{th}}$ aperture, the new critical velocity $\tilde{v}_{c,i}$ is chosen from a distribution centered on $v_{c,i}$ and with width, the thermal width, common to all apertures. Within this approach, the effect of thermal fluctuations is the same as choosing a new distribution of critical velocities for each cycle, and therefore within any cycle thermal fluctuations act analogously to quenched disorder in the critical velocities. Moreover, if the two sources of disorder are Gaussian, their effects can be combined into one "effective" source of width given by $(\sigma_{\mathrm{q}}^2 + \sigma_{\mathrm{t}}^2)^{1/2}$, where q and t correspond to quenched and thermal disorder. Therefore, as before, the criterion for the avalanching regime can be estimated by Eq. (3.36), but now using the effective disorder width.

### Effects of inlet/outlet shape

Systematic inhomogeneity in velocities of superflow through the various apertures may also act to destroy both the avalanching regime and the whistle. One source of such inhomogeneities is the shape of the inlet and outlet that guide the superfluid towards and away from the array of apertures. First, consider the velocity profile for superfluid flowing through a single circular orifice in a thin membrane [31]. In the plane of the membrane, the velocity profile inside the orifice is given by [31]

$$v_s(r) \propto \frac{1}{\sqrt{a^2 - r^2}}, \tag{3.78}$$

where $a$ is the radius of the orifice and $r$ is the distance to the center, and the flow is directed perpendicular to the membrane. Due to the tangential flows along the membrane, the fastest flow occurs at the edges. A similar effect occurs in the flow through a small array of apertures embedded in a large membrane: the fastest flow occurs through the outer apertures. Therefore, the critical velocity is reached first for the outer apertures, resulting in the loss of synchronicity between the outer and inner apertures, and consequently in the loss of avalanching and "whistling."

We investigate the consequences of this effect for experiments of the Berkeley group by plotting the current drop in each cycle $I_{\text{slip}}$ (i.e. the half-difference between the maximum and minimum currents in that cycle) as a function of temperature for the following two different boundary conditions on the capacitance matrix: open and quasi-periodic (see Fig. 3.11). The open boundary condition, in which the inter-aperture distance is measured in the usual geometric way, corresponds to an array of apertures embedded in a large membrane. In the quasi-periodic case we measure the distance by selecting the shortest route on the torus which eliminates tangential flows and results in a velocity profile that is similar to one that may be achieved from optimally shaped inlet and outlet pipes. The velocity profile through the various apertures is constant for the case of quasi-periodic boundary conditions (in the absence of both quenched and thermal disorder), and therefore all the apertures slip together, which corresponds to the maximum current-oscillation amplitude $I_{\text{slip}}$. As the temperature is lowered, the superfluid density increases with a $(T_\lambda - T)^{2/3}$ law, and this accounts for the rise of $I_{\text{slip}}$. On the other hand, for open boundary conditions $I_{\text{slip}}$ deviates from the $(T_\lambda - T)^{2/3}$ law at lower temperatures. This deviation is associated with the edge-induced velocity profile inhomogeneity. As the superfluid velocity increases, so does the difference between the velocity through the outer and inner apertures. Therefore, the loss of synchronicity will be more pronounced for higher critical velocities and, thus, lower temperatures. Finally, adding disorder to the model brings the predicted theoretical result in-line with the experimental measurements.

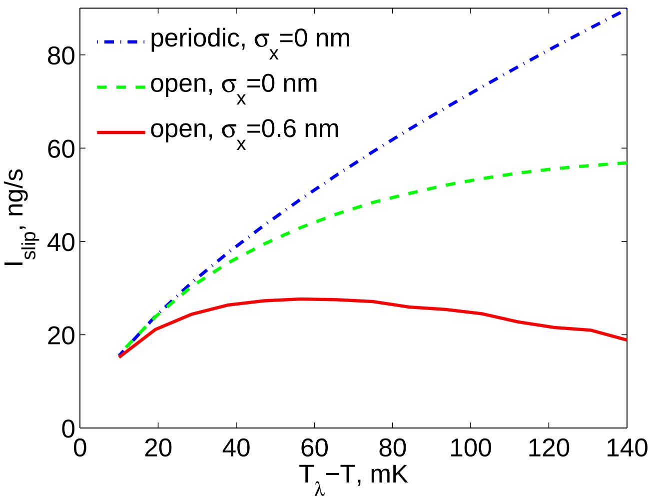

Figure 3.11: Effect of array edges on $I_{\rm slip}$ vs. $T$. Three curves represent $I_{\rm slip}$ with quasi-periodic boundary conditions and no disorder, open boundary conditions with no disorder and with open boundary conditions and $\sigma_x = 0.6\,\rm nm$. Here we used nominal values of parameters corresponding to Berkeley group's experiment: $N \times N = 65 \times 65$, $r_0 = 15\,\rm nm$, $\ell = 3\,\mu\rm m$, $d = 50\,\rm nm$.

In conclusion, edge effects act to suppress $I_{\rm slip}$ at lower temperatures, and are a source of performance degradation for superfluid quantum interference devices based on arrays of nanoapertures. These edge effects are strongest for closely spaced apertures and large arrays. Edge effects can be minimized by a combination of inlets and outlets to collimate the superflow, and thus remove systematic inhomogeneities associated with the edges of the array.

### 3.3.11 Concluding remarks

Motivated by recent experiments performed by the Berkeley group on superflow through arrays of nanoapertures [65], we have developed a model to describe phase-slip dynamics of such systems. The main features of our model are: (i) effective inter-aperture couplings, mediated through the bulk superfluid, and (ii) randomness in the critical velocities of the apertures, the latter being effectively controlled through the temperature.

By developing and analyzing this model, we find that a competition, between site-disorder in the critical velocities and effective inter-aperture coupling, leads to the emergence of rich collective dynamics, including a transition between avalanching and non-avalanching regimes of the phase-slip dynamics. We identify a line of critical disorder-strengths on the disorder—interaction strength phase diagram, at which there is a divergent susceptibility, in the sense that near to this line small changes in the control parameter can lead to large changes in the fraction of phase-slipped apertures.

Our model reproduces the key physical features of the Berkeley group's experiments [65], including a high-temperature synchronous regime, a low-temperature asynchronous regime, and a transition between the two. We therefore feel that our model captures the essential physics explored in these experiments.

It is likely that technologically useful devices, such as ultra-precise gyrometers, can be designed to function not only in the Josephson (i.e. reversible) regime but also in the phase-slippage (i.e. irreversible) regime, provided that a large enough fraction of apertures can be arranged to slip sufficiently simultaneously so as to produce a measurable “whistle” at the Josephson frequency [67]. We remark that, in the setting of multi-link superconducting devices, it has been shown that the irreversible regime can be utilized for magnetic-field and related phase-sensitive measurements [38].

# Chapter 4

# Conclusions

In this thesis we have explore superflows in multiply connected geometries. In particular we have concentrated on geometries with multiple constrictions and on interactions between phase-slips occurring in these constrictions. We find and investigate many interesting physical phenomena in these systems, spanning from non-linear physics and avalanches to superconducting-phase gradiometery.

# Appendix A

# Physical Scales

It is convenient to express the results of the long-wire model, Eqs. (2.41,2.45,2.46), in terms of macroscopic physical parameters. Following Tinkham and Lau [59], we express the condensation energy scale per coherence length of wire as

$$\mathcal{E} = 0.22\, k_{\mathrm{B}} T_{\mathrm{c}} \,(1-t)^{3/2}\, \frac{R_{\mathrm{q}}}{R_{\mathrm{N}}} \frac{b}{\xi(T=0)}, \tag{A.1}$$

where $t \equiv T/T_{\mathrm{c}}$, $R_{\mathrm{N}}$ is the normal-state resistance of the device, and $R_{\mathrm{q}} \equiv h/4e^2 \approx 6.5\,\mathrm{k\Omega}$ is the quantum of resistance. The LAMH prefactor for sequential phase slips then becomes

$$\Omega = \frac{b\sqrt{1-t}}{\xi(T=0)} \left( \frac{8\sqrt{2}\,\mathcal{E}}{3\, k_{\mathrm{B}} T_{\mathrm{c}}} \right)^{1/2} \frac{8 k_{\mathrm{B}} (T_{\mathrm{c}} - T)}{\pi \hbar}, \tag{A.2}$$

and for parallel phase slips it becomes

$$\Omega = \left( \frac{b\sqrt{1-t}}{\xi(T=0)} \right)^{2} \left( \frac{16\sqrt{2}\,\mathcal{E}}{3\, k_{\mathrm{B}} T_{\mathrm{c}}} \right)^{1/2} \frac{8 k_{\mathrm{B}} (T_{\mathrm{c}} - T)}{\pi \hbar}. \tag{A.3}$$

The remaining parameters in the model are $R_N$, $T_{\mathrm{c}}$ and $\xi(T=0)$. The normal-state resistance and the critical temperature may be obtained from the $R$ vs. $T$ curve. The coherence length may be obtained by comparing $\mathcal{E}$ obtained from the critical current at low temperature, via

$$I_{\mathrm{c}} = \frac{2}{3\sqrt{3}} \frac{16\pi\mathcal{E}}{\Phi_0}, \tag{A.4}$$

with $\mathcal{E}$ obtained via Eq. (A.1).

In experiments, it is expected that the two wires are not identical. The long-wire model can be easily extended to this case. The number of parameters to be fitted would then expand to include the normal-state resistance for each wire (only one of which is free, as the pair are constrained by the normal-state resistance of the entire device, which can be extracted from the $R$ vs. $T$ curve), a zero-temperature coherence length for each wire, and critical temperatures for each wire.

# Appendix B

# Ambegaokar-Halperin formula for resistance of a damped Josephson junction

In this appendix we reproduce the result of the Ambegaokar-Halperin Letter [5], but correcting typographical errors. Eq. (9) of reference [5] should read

$$\nu = \frac{\bar{V}}{I_c R} = \frac{4\pi\left(e^{\pi\gamma x} - 1\right)}{\gamma\left(\int_0^{2\pi} d\theta \int_0^{\theta} d\theta' \, \frac{f(\theta)}{f(\theta')} + e^{\pi\gamma x} \int_0^{2\pi} d\theta \int_0^{2\pi} d\theta' \, \frac{f(\theta)}{f(\theta')}\right)}, \tag{B.1}$$

where,

$$f(\theta) = e^{\frac{1}{2}\gamma(x\theta + \cos\theta)}, \tag{B.2}$$

$\nu$ is related to the resistance of the shunted junction through $R = \nu I_c R_{\mathrm{N}}/I$, $x$ and $\gamma$ are defined in Eq. 2.31b.

# Appendix C

# LA-MH theory for a single bridge

In this appendix we reproduce useful formulas from LA [6], and rewrite them in a way that is convenient for further calculations, especially for numerical implementation. As in the case of single-wire LAMH theory, one starts with the Ginzburg-Landau free energy

$$F = \int_{-b/2}^{b/2} \left( \alpha|\psi|^2 + \frac{\beta}{2}|\psi|^4 + \frac{\hbar^2}{2m}|\nabla_z \psi|^2 \right) dz. \tag{C.1}$$

The relationships between the parameters of the Ginzburg-Landau free energy ($\alpha$ and $\beta$), the coherence length $\xi$, the condensation energy per coherence length $\mathcal{E}$, the critical field $H_{\mathrm{c}}$, and the cross-sectional area of the wire $\sigma$ are given by $\frac{\alpha^2}{\beta} = \frac{H_c^2 \sigma}{8\pi} = \mathcal{E}/\xi$ and $\xi^2 = \frac{\hbar^2}{2m|\alpha|}$. Following McCumber [30], it is convenient to work in terms of the dimensionless units obtained using the transformations: $|\psi|^2 \to \frac{\alpha}{\beta}|\psi|^2$, $z \to \sqrt{\frac{2m|\alpha|}{\hbar^2}}z$, and $b \to b/\xi = \sqrt{\frac{2m|\alpha|}{\hbar^2}}b$. In terms of these units, the free energy becomes

$$F = 2\mathcal{E} \int_{-b/2}^{b/2} \left( \frac{1}{2}(1 - |\psi|^2)^2 + |\nabla_z \psi|^2 \right) dz. \tag{C.2}$$

The Ginzburg-Landau equation is obtained by varying the free energy:

$$\delta F = 0 \ \Rightarrow \ -\psi + |\psi|^2\psi - \nabla^2\psi = 0. \tag{C.3}$$

By writing $\psi = fe^{i\phi}$ and taking the real and imaginary parts of the Ginzburg-Landau equation one obtains

$$-f + f^3 + (\phi')^2 f = f'', \tag{C.4}$$

$$2\phi' f' + \phi'' f = 0. \tag{C.5}$$

From Eq. (C.5), one finds the current-conservation law:

$$f^2 \phi' = J, \tag{C.6}$$

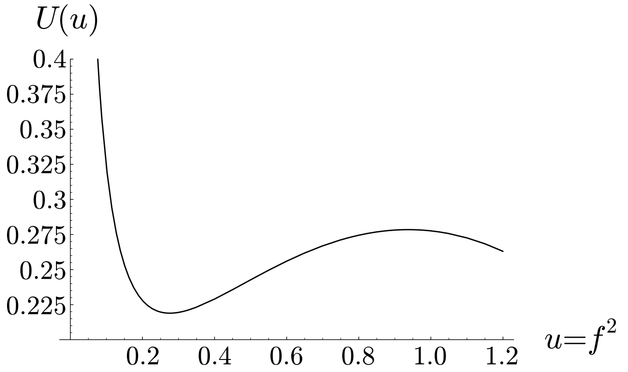

Figure C.1: "Mechanical potential" $U[u = f^2]$ at an intermediate value of the dimensionless current, plotted as a function of amplitude squared to make comparison with Fig. 2.11 more convenient.

where $J$ is identified with the dimensionless current $\frac{1}{2i}(\psi^*\nabla\psi - \psi\nabla\psi^*)$. The physical current (in stat-amps) is given by $I = JcH_c^2\sigma\xi/\Phi_0$. Expressing $\phi'$ in terms of J, Eq. (C.4) becomes

$$f'' = -f + f^3 + \frac{J^2}{f^3} = -\frac{d}{df}U(f), \tag{C.7}$$

where the effective potential $U(f)$ is given by

$$U(f) = \frac{J^2}{2f^2} + \frac{f^2}{2} - \frac{f^4}{4}. \tag{C.8}$$

Following LA, Eq. (C.8) can usefully be regarded as the equation of motion for a particle with position $f(z)$, where $z$ plays the role of time, moving in the potential $U(f)$ [6]. Before proceeding to find the solution of this equation, we pause to consider the type of trajectories that are possible. Later, it will be demonstrated that at the edge of the wire $f(\pm b) \geq 1$, so the particle starts to the right of the hump; see Fig. C.1. If the total energy of the particle is less than the height of the hump, the particle will be reflected by the hump. If, however, the particle starts with more energy than the height of the hump, it will pass over the hump and be reflected by the part of $U(f)$ dominated by $J^2/2f^2$.

The equation of motion can be solved via the first integral (i.e. multiplying both sides by $f$ and integrating with respect to $f$):

$$E = \frac{(f')^2}{2} + U(f) \;\Rightarrow\; f' = \sqrt{2(E - U(f))}, \tag{C.9}$$

where $E$ is a constant of integration (i.e. the energy of the particle in the mechanical analogy), which gives

$$z = \int_{f_0}^{f} \frac{df}{\sqrt{2(E - U(f))}} = \int_{f_0}^{f} \frac{f\,df}{\sqrt{2f^2E - J^2 - f^4 + f^6/2}}. \tag{C.10}$$

It is convenient to apply “initial” conditions at the middle of the wire, where $f(z=0) = f_0$, and to integrate towards the edges. We require that the particle come back to its starting point after a “time” $b$, i.e. at the edges of the wire the amplitude of the order parameter must match the boundary condition. Therefore, the middle of the wire must be the turning-point for the particle, i.e., at $z = 0$ we have $E = U(f_0)$.

What follows next is a series of manipulations via which one can express solution for $f(z)$ in terms of special functions.

Step 1: substitution: $f^2 \to u$

$$z = \frac{1}{2}\int_{u_0}^{u} \frac{du}{\sqrt{2Eu - J^2 - u^2 + u^3/2}} \tag{C.11}$$

Step 2: substitution: $u \to u_0 + \epsilon$

$$2z = \int_0^{u-u_0} \frac{d\epsilon}{\left[\epsilon(\underbrace{\left(\frac{J^2}{u_0} - u_0 + u_0^2\right)}_{\alpha} + \underbrace{\left(\frac{3}{2}u_0 - 1\right)}_{\beta}\epsilon + \epsilon^2/2)\right]^{1/2}} \tag{C.12}$$

$$2z = \int_0^{u-u_0} \frac{d\epsilon}{(\epsilon(\epsilon + \beta\epsilon + \epsilon^2/2))^{1/2}} \tag{C.13}$$

$$= \int_0^{u-u_0} \frac{\sqrt{2}d\epsilon}{(\epsilon(\epsilon + \underbrace{\beta + \sqrt{\beta^2 - 2\alpha}}_{-u_1})(\epsilon + \underbrace{\beta - \sqrt{\beta^2 - 2\alpha}}_{-u_2}))^{1/2}} \tag{C.14}$$

$$= \int_0^{u-u_0} \frac{\sqrt{2}d\epsilon}{(\epsilon(\epsilon - u_1)(\epsilon - u_2))^{1/2}} \tag{C.15}$$

Step 3: substitution: $\epsilon \to u_1 z^2$

$$2z = \frac{2\sqrt{2}}{\sqrt{u_2}}\int_0^{\sqrt{\frac{u-u_0}{u_1}}} \frac{d\omega}{((\omega^2 - 1)(\frac{u_1}{u_2}\omega^2 - 1))^{1/2}} \tag{C.16}$$

$$= \frac{2\sqrt{2}}{\sqrt{u_2}}\text{EllipticF}\big[\text{ArcSin}\big[\sqrt{\frac{u - u_0}{u_1}}\big], \frac{u_1}{u_2}\big] \tag{C.17}$$

The following definitions have been used:

$$\alpha[u_0] \equiv J^2/u_0 - u_0 + u_0^2, \qquad \beta[u_0] \equiv \frac{3}{2}u_0 - 1, \tag{C.18}$$

$$u_1[\alpha, \beta] \equiv -\beta - \sqrt{\beta^2 - 2\alpha}, \qquad u_2[\alpha, \beta] \equiv -\beta + \sqrt{\beta^2 - 2\alpha}. \tag{C.19}$$

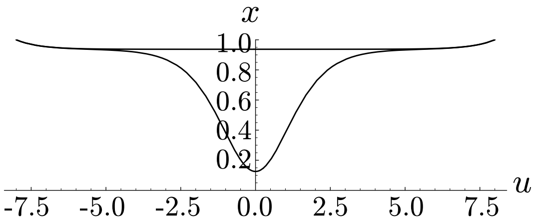

Figure C.2: Squared amplitude $u$ of the order parameter as a function of position along the wire for the two types of solution: metastable and saddle point.

By inverting relation (C.17) one obtains an explicit equation for the amplitude of the order parameter as a function of position along the wire (see Fig. C.2):

$$f^2(z) = u_0 + u_1 \sin^2\left[\text{JacobiAmplitude}\left[z\sqrt{\frac{u_2}{2}}, \frac{u_1}{u_2}\right]\right] \tag{C.20a}$$

$$= u_0 + u_1 \text{JacobiSn}^2\left[z\sqrt{\frac{u_2}{2}}, \frac{u_1}{u_2}\right]. \tag{C.20b}$$

The end-to-end phase difference along the wire may be found by using the current-conservation law. Thus, one obtains

$$\theta = \int_{-b/2}^{b/2} \frac{J}{f^2(z)} dz = 2J \int_0^{b/2} \frac{dz}{u_0 + u_1 \text{JacobiSn}^2\left[z\sqrt{\frac{u_2}{2}}, \frac{u_1}{u_2}\right]}. \tag{C.21}$$

The Helmholtz free energy can be found by substituting the expressions for $f(z)$ and $\phi'(z)$ into the expression for the free energy. One then obtains

$$F = 4\mathcal{E} \int_0^{b/2} \left(\frac{1}{2} - 2f^2 + f^4 + \frac{J^2}{u_0} + u_0 - \frac{u_0^2}{2}\right) dz, \tag{C.22}$$

where $E$ has been expressed in terms of $u_0$. Equations (C.21,C.22) provide expressions for $\theta$ and $F$ that hold regardless of the length of the wire and, therefore, may be used as a starting point for computing the Gibbs free-energy of the various metastable states subject to the total-current and phase constraints.

# Appendix D

# Josephson effect in a single aperture

We would like to consider the Josephson effect in a single $^4$He aperture. The setup is as follows.

- Two reservoirs of superfluid helium are joined by a single aperture.
- The aperture diameter and length are sufficiently small that its free energy may be described by the Josephson relation.
- The pressure difference is applied across the aperture, giving rise to a chemical potential difference that tends to drive a supercurrent.
- We assume that the at each point in time, the system is in thermodynamic equilibrium. This assumption is true when the relaxation time between different modes in the superfluid is much faster than the inverse Josephson frequency. This relaxation time may be estimated from the ratio of the reservoir size to the speed of sound.
- The flow of supercurrent through the aperture is insufficient to fix the chemical potential imbalance

The question we would like to address is what role do the thermal fluctuations in the superfluid play? What happens when $k_{\mathrm{B}}T$ is on the order of Josephson energy for the Junction $E_J$? Do thermal fluctuations destroy the Josephson effect?

We assume that there is a well-defined phase difference between the left and right reservoirs. When a chemical potential difference is applied between the reservoirs, the relative phase between them winds according to the Josephson-Anderson relation:

$$\dot{\varphi}(t) = -\frac{1}{\hbar}\Delta\mu(t). \tag{D.1}$$

Where is this phase difference specified? The only possible location to set the phase difference is far away from the aperture, where, due to long range order in 3D superfluid, it makes sense to specify values of phase differences. Without loss of generality, to simplify the calculations we consider two spherical reservoirs of radius $R$, connected by an aperture of radius $r_0$ (it is, of course, not possible to embed this setup into three dimensional space, but the qualitative behavior is identical to the more realistic setup described in Chapter 3). The phase of the order parameter in the left and right spheres, $\varphi_{\mathrm{L}}(r)$ and $\varphi_{\mathrm{R}}(r)$, will be set on the outer walls, as follows:

$$\varphi_{\mathrm{L}}(r=R, \mathbf{\Omega}) = \varphi_0^{\mathrm{L}}, \qquad \varphi_{\mathrm{R}}(r=R, \mathbf{\Omega}) = \varphi_0^{\mathrm{R}}. \tag{D.2}$$

To determine if the Josephson effect persists in spite of thermal fluctuations, we shall fix the phases $\varphi_0^{\mathrm{L}}$ and $\varphi_0^{\mathrm{R}}$ deep in the bulk superfluids, and look for a Josephson supercurrent through the aperture.

## D.1 Partition function

Next, we need to obtain the partition function describing the superfluid in the reservoirs as well as in the aperture. Here, we will take a different approach than in the main text to coupling the superfluid in the two reservoirs through the aperture. Similar to the main text, we assume that the energy of the superfluid in the aperture can be described by a single variable — the phase difference across it. However, instead of joining the description of the superfluid in the bulk and in the aperture on a surface enclosing the aperture opening we take a different strategy. On each side of the aperture we compute the weighted average of the phase of the bulk superfluid, with the weighting function $T(r)$ that is concentrated near the aperture openings. Next, we set the phase across the aperture to be the difference of these weighted averages. (Alternatively, we could consider a point aperture and introduce some ultraviolet cut-off of in the $k$ sums, but what we do amounts to the same thing, with the cut-off scale being set by the inverse of the aperture radius $r_0$. It is important to note that this trick only works for non-extended Josephson junctions, i.e. when $\xi \gtrsim r_0$.)

Using the energy functional for the bulk superfluids from the main text, and the averaging procedure for connecting the aperture to the bulk superfluids, we obtain the partition function

$$Z = \int\limits_{\varphi_{\mathrm{L}}(R)=\varphi_0^{\mathrm{L}},\ \varphi_{\mathrm{R}}(R)=\varphi_0^{\mathrm{R}}} D[\varphi_{\mathrm{L}}, \varphi_{\mathrm{R}}, \phi, \zeta] \quad e^{-\beta\left[\int_0^R (\nabla\varphi_{\mathrm{L}})^2 + (\nabla\varphi_{\mathrm{R}})^2\, d^3r + i\zeta\left(\phi - \int_0^R T(r)(\varphi_{\mathrm{L}}(r) - \varphi_{\mathrm{R}}(r))\, d^3r\right) - J\cos\phi\right]}, \tag{D.3}$$

where $T(r)$ is the normalized tempering function that describes how to weigh the average value of $\varphi(r)$ in the vicinity of the aperture, and $\zeta$ is a Lagrange multiplier used to enforce the condition that the phase across the aperture $\phi$ matches the difference of the weighted averages $\int_0^R T(r)(\varphi_{\mathrm{L}}(r) - \varphi_{\mathrm{R}}(r))\, d^3r$. It is convenient to transform to normal modes of the reservoir. As only the isotropic ($l = 0$ modes) can couple through the junction (all the other modes do not survive the averaging by the isotropic wighting function), we may ignore all the other modes. Furthermore, we take the opportunity to enforce the boundary condition, and write:

$$\varphi_{\mathrm{L/R}}(r) = \varphi_0^{\mathrm{L/R}} + \frac{1}{\sqrt{2\pi R}} \sum_{k=\pi n/R} A_k^{\mathrm{L/R}} \frac{\sin(kr)}{r} \qquad (n = 1, 2, \ldots). \tag{D.4}$$

These form an orthonormal basis set, except for the $k = 0$ mode which is orthogonal but not normal, as can be easily verified:

$$\frac{1}{2\pi R} \int_0^R 4\pi r^2 \, dr \frac{\sin(kr)}{r} \frac{\sin(k'r)}{r} = \delta_{k,k'}. \tag{D.5}$$

Furthermore, we can show that modes are not coupled by the kinetic energy term

$$\frac{1}{2\pi R} \int_0^R 4\pi r^2 \, dr \left(\partial_r \frac{\sin(kr)}{r}\right) \left(\partial_r \frac{\sin(k'r)}{r}\right) = k^2 \delta_{k,k'}. \tag{D.6}$$

Finally, we make a convenient choice of the tempering function and take the inner product. We believe that the exact form of the tempering function is unimportant, so it is convenient to choose:

$$T(r) = \frac{e^{-r/r_0}}{r} \left(\int_0^R 4\pi r^2 \frac{e^{-r/r_0}}{r} \, dr\right)^{-1}. \tag{D.7}$$

The inner product of $T(r)$ and one of the basis functions is given by:

$$\int_0^R \frac{4\pi r^2}{\sqrt{2\pi R}} \frac{\sin(kr)}{r} T(r) \, dr = \frac{2}{\sqrt{2\pi R}} \frac{k}{1 + k^2 r_0^2} \tag{D.8}$$

Using the basis set Eq. (D.4), we express the partition function as

$$Z = \int D[A_k^{\mathrm{L}}, A_k^{\mathrm{R}}, \phi, \zeta] \exp -\beta \left[\sum_{k>0} k^2 ({A_k^{\mathrm{L}}}^2 + {A_k^{\mathrm{R}}}^2) + i\zeta \left\{\phi - \left(\varphi_0^{\mathrm{L}} - \varphi_0^{\mathrm{R}} + \frac{2}{\sqrt{2\pi R}} \sum_{k>0} (A_k^{\mathrm{L}} - A_k^{\mathrm{R}}) \frac{k}{1 + k^2 r_0^2}\right)\right\} - J\cos\phi\right], \tag{D.9}$$

Performing the Gaussian integrals over the $A_k$ and $B_k$ modes, we obtain

$$Z = \int D[\phi, \zeta] e^{-\beta\left[\zeta^2 \sum_{k>0} \frac{1}{\pi R}\left(\frac{1}{1+k^2 r0^2}\right)^2 + i\zeta(\phi - (\varphi_0^{\mathrm{L}} - \varphi_0^{\mathrm{R}})) - J\cos\phi\right]}; \tag{D.10}$$

The mode summation may be easily evaluated for $r_0 \ll R$:

$$\sum_{k>0} \frac{1}{\pi R} \left( \frac{1}{1+k^2 r0^2} \right)^2 = \frac{1}{4\pi r_0} + O\left(\frac{r_0}{R}\right)^2 . \tag{D.11}$$

Finally, by performing the integral over the constraint we find the effective partition function for the phase difference across the junction:

$$Z[\phi_0^{\mathrm{L}} - \phi_0^{\mathrm{R}}] = \int D[\phi] e^{-\beta\left[\pi r_0\left[\phi - (\varphi_0^{\mathrm{L}} - \varphi_0^{\mathrm{R}})\right]^2 - J\cos\phi\right]} \tag{D.12}$$

## D.2 Electrostatic approach to partition function

Instead of using the above averaging procedure for joining the description of the superfluid inside the aperture to the description in the bulk, we can follow the procedure outlined in the main text. To summarize: as the theory for the bulk superfluid is quadratic, thermal fluctuations result in a additive constant to the effective action as compared to its classical value. Therefore, we may compute the effective action by evaluating the classical action and ignore the additive constant. Appealing to the electrostatic analogy, the energy of the aperture due to coupling to the phase at infinity (i.e. due to self-capacitance) will be given by

$$U = 2\int_0^R (\nabla\varphi)^2\, d^3r = 2\int_{r_0}^R 4\pi r^2 \frac{r_0^2}{r^4}\left(\frac{\phi}{2} - \frac{\varphi_0}{2}\right)^2 dr = 2\pi r_0(\phi - \varphi_0)^2, \tag{D.13}$$

where the phase difference has been split between the left and right sides. This form of the action is the same as the one that appears in the expression for the partition function Eq. (D.12) above up to a factor of 2, which arises due to different choices of how to couple the description of the superfluid in the aperture to the description of the superfluid in the bulk.

## D.3 Supercurrent

The supercurrent through the junction may be computed via

$$I = \frac{\int D[\phi] J \sin\phi\, e^{-\beta\left[\pi r_0\left[\phi - (\varphi_0^{\mathrm{L}} - \varphi_0^{\mathrm{R}})\right]^2 - J\cos\phi\right]}}{\int D[\phi] e^{-\beta\left[\pi r_0\left[\phi - (\varphi_0^{\mathrm{L}} - \varphi_0^{\mathrm{R}})\right]^2 - J\cos\phi\right]}} \tag{D.14}$$

If $r_0\beta \ll 1$, the current through the junction will be very strongly suppressed. This is the high temperature limit. For the case of small $J$ we may compute the current in perturbation theory.

$$I = Je^{-1/4\pi r_0\beta}\sin\phi_0, \tag{D.15}$$

if we are at high temperature, i.e. $8\pi r_0\beta \ll 1$, then the formula is valid for $J < 1/\beta$; at low temperature the range of validity is $J < 8\pi r_0$.

## D.4 Results

In this appendix we obtain two results. First, the mechanism for coupling the descriptions of the bulk superfluid and the superfluid in the aperture does not seem to be very important. Second, as long as the phase difference between the bulk superfluids is well defined, there will be a Josephson current. This current is maintained, even for the case of very weak Josephson coupling, due to the stabilization of the phase across the aperture by coupling to the phase at infinity. However if this coupling is also weak, than strong thermal fluctuations of the phase across the aperture arise leading to the suppression of the Josephson effect.

# Appendix E

# Avalanche size scaling and other critical exponents in mean-field-theory

The goal of this appendix is to provide details of a computation of the distribution $D(S)$ of avalanche sizes $S$. In order to achieve this goal, we adopt Dahmen's [77] calculation of avalanche-size scaling within mean-field theory, which was done in the setting of the Random Field Ising Model, to our model of avalanches in the superflow of helium. We note that at the mean field level, the two models are very similar with identical critical exponents.

Our mean-field model for the dynamics of the phases across various apertures is obtained by disorder-averaging the phase-difference across a single aperture in a self-consistent way. The half-phase difference across the $i^{\text{th}}$ aperture, see Eq. (3.33) in the main text, satisfies the equation

$$\phi_i = \frac{A\Phi + B\langle\phi\rangle + 4\pi J n_i}{C + 4J}, \tag{E.1}$$

This equation must be supplemented by the condition that whenever the phase difference across an aperture exceeds its critical value, $\phi_{\text{c},i}$, it phase-slips. These two conditions lead to the mean-field equation

$$\langle\phi\rangle = \frac{A}{A+4J}\Phi + \frac{4\pi J}{A+4J}\sum_k k \int_{\varphi_k}^{\varphi_{k-1}} d\phi_{\text{c}}\, Q(\phi_{\text{c}}), \tag{E.2}$$

where $\varphi_k = (A\Phi + B\langle\phi\rangle - \pi k C)/(C + 4J)$. We concentrate on the "restricted" case, in which the disorder distribution is sufficiently narrow such that $|n_i - n_j| = \{0, 1\}$; in this setting, at any given $\Phi$ there are two populations of apertures: the ones that have slipped $n$ times, and the ones that have slipped $n+1$ times; the fraction of the latter will be denoted by $f$.

## E.1 Avalanche size distribution

We would like to find the distribution of avalanche sizes, i.e., the probability that an avalanche involves exactly $S$ apertures. To approach this question, we first ask how many apertures are triggered, $n_{\text{trig}}$, if one aperture phase-slips? The phase-slip in the initial aperture causes an increase in $\langle\phi\rangle$, which in turn causes the various $\phi_i$'s to advance. This advance may trigger additional phase slips, as apertures are driven above their critical velocities.

Before the initial event, we can divide the apertures into two groups, denoted by $U_\pm$, $U_+$ containing the $Nf$ apertures that have already slipped and $U_-$ containing the $N(1-f)$ apertures that have yet to slip. From Eq. (E.1) and the definition of $\langle\phi\rangle$ we obtain the equations for $\phi_\pm$ corresponding to $U_\pm$:

$$\phi_-(C+4J) - B\langle\phi\rangle = A\Phi, \tag{E.3}$$

$$\phi_+(C+4J) - B\langle\phi\rangle = A\Phi + 4\pi J, \tag{E.4}$$

$$\langle\phi\rangle = f\phi_+ + (1-f)\phi_-. \tag{E.5}$$

Here, $f$ must be obtained from the distribution of $\phi_\mathrm{c}$'s. In particular we obtain that

$$\langle\phi\rangle = \frac{A\Phi}{A+4J} + \frac{4\pi J f}{A+4J}. \tag{E.6}$$

When the initial aperture slips $f \to f + 1/N$, and this causes $\langle\phi\rangle$ as well as $\phi_\pm$ to advance:

$$\langle\phi\rangle \to \langle\phi\rangle + \frac{4\pi J}{A+4J}\frac{1}{N}, \tag{E.7}$$

$$\phi_\pm \to \phi_\pm + \frac{B}{C+4J}\frac{4\pi J}{A+4J}\frac{1}{N}. \tag{E.8}$$

If there are any apertures that have $\phi_c$ in the interval

$$\left(\phi_-, \phi_- + \frac{B}{C+4J}\frac{4\pi J}{A+4J}\frac{1}{N}\right), \tag{E.9}$$

these apertures will be triggered to phase slip by the initial phase slip. The number of such apertures is

$$n_\mathrm{trig} = N\int_{\phi_-}^{\phi_-+\delta} Q(\phi_\mathrm{c})\,d\phi_\mathrm{c} = \frac{B}{C+4J}\frac{4\pi J}{A+4J}Q(\phi_-), \tag{E.10}$$

where we have assumed that $Q(\phi_\mathrm{c})$ is a slowly varying function.

Consider an avalanche of size $S$. In the process of this avalanche we have that

$$\phi_- \to \phi_- + \frac{B}{C+4J}\frac{4\pi J}{A+4J}\frac{S}{N}. \tag{E.11}$$

To have such an avalanche, there must be exactly $S-1$ secondary apertures within this interval. We shall assume that the distribution of $\phi_c$'s is uniform within this interval, with a density $NQ(\phi_-)$. We can therefore identify this as a Poisson process, the probability being $P_\nu(S-1)$ where $\nu$ is the expected number of events. Thus, we have that

$$\nu = SQ(\phi_-)\frac{B}{C+4J}\frac{4\pi J}{A+4J} = (t+1)S, \tag{E.12}$$

$$P_\nu(S+1) = \frac{\nu^{S-1}e^{-\nu}}{(S-1)!} \approx \frac{1}{\sqrt{2\pi S}}(t+1)^{S-1}e^{-St}, \tag{E.13}$$

where we have used Stirling's approximation (i.e. $n! \approx \sqrt{2\pi n}(n/e)^n$) in the last step. Finally, we notice (as pointed out in Dahmen's thesis [77]) that we are over-counting by a factor of $S$, as this interval may contain two or more smaller avalanches as opposed to one big one. Therefore, the mean-field result for the avalanche size distribution is in fact

$$D(S) \approx \frac{1}{S^{3/2}\sqrt{2\pi}}e^{-st^2/2}, \tag{E.14}$$

where we have expanded for small $t \equiv n_{\text{trig}} - 1$. At criticality $t = 0$, and the distribution attains a $-3/2$ power law. As we move away from criticality, this power law gets cut off for large avalanches at the scale $S \sim 2/t^2$.

## E.2 Mean-field-theory in the vicinity of criticality

We would like to understand the scaling of various quantities, within mean-field-theory, near the critical end-point point and the first-order line. In particular this will tell us how close we have to be to criticality to obtain power-law scaling of the avalanche sizes.

Consider the susceptibility

$$\chi \equiv \frac{d\langle\phi\rangle}{d\Phi}, \tag{E.15}$$

which describes the rate of change of the mean-field in response to the change of the control-phase $\Phi$. By differentiating the mean-field equation, Eq. (E.2), with respect to $\Phi$, we obtain an expression for this susceptibility that can be expanded about a critical point or line:

$$\chi = \frac{A}{A+4J}\left(1 + \frac{4\pi J}{C+4J}Q(x)\right)\left(\frac{1}{-t(x)}\right), \tag{E.16}$$

where $x \equiv (A\Phi + B\langle\phi\rangle)/(C+4J) - \phi_c^0$. In the vicinity of an SWA, small changes in $\Phi$ cause drastic changes in $\langle\phi\rangle$. In particular, when $Phi$ reaches the value at which an SWA occurs, a single phase slip will trigger a macroscopic number of secondary phase slips through a cascade. Thus in the vicinity of an SWA $t(x) \to 0$ and $\chi$ diverges. At fixed $\sigma$, as $\Phi$ is tuned $t(x)$ can approach zero in two ways: either (i) by approaching the critical end-point located at $\sigma = \sigma_c$ or (ii) by approaching the first order line that stretches from $\sigma = 0$ to $\sigma = \sigma_c$. We define $\Phi_c(\sigma)$, as the value of the control-phase at which $t(x) \to 0$.

How can $t(x) \to 0$? This can happen by tuning $\Phi$ or $\sigma$. We can simplify the expression for $\chi$ in the vicinity of criticality by expanding up to second power in $x$ and first in $\sigma$:

$$\chi \simeq -\frac{\frac{A}{B}\frac{C+4J}{A+4J}}{(x-x_c)\partial_x t(x_c) + \frac{1}{2}(x-x_c)^2\partial_x^2 t(x_c) + (\sigma-\sigma_c)\partial_\sigma t(x_c)}, \tag{E.17}$$

$$Q(x) = \frac{e^{-x^2/2\sigma^2}}{\sqrt{2\pi}\sigma}, \tag{E.18}$$

$$t(x_c) = 0 = \frac{B}{C+4J}\frac{4\pi J}{A+4J}Q(x_c) - 1, \tag{E.19}$$

$$\partial_x t(x_c) = \frac{B}{C+4J}\frac{4\pi J}{A+4J}\left(-\frac{x}{\sigma^2}\right)\frac{e^{-x^2/2\sigma^2}}{\sqrt{2\pi}\sigma}, \tag{E.20}$$

$$\partial_x^2 t(x_c) = \frac{B}{C+4J}\frac{4\pi J}{A+4J}\left(-\frac{1}{\sigma^2} + \left(\frac{x}{\sigma^2}\right)^2\right)\frac{e^{-x^2/2\sigma^2}}{\sqrt{2\pi}\sigma}, \tag{E.21}$$

$$\partial_\sigma t(x_c) = \frac{B}{C+4J}\frac{4\pi J}{A+4J}\left(-\frac{1}{\sigma} + \frac{x^2}{\sigma^3}\right)\frac{e^{-x^2/2\sigma^2}}{\sqrt{2\pi}\sigma}. \tag{E.22}$$

Here, we can consider two cases: the system is near the critical end-point (i.e. $\sigma \simeq \sigma_c$ and $x \simeq 0$), or near the first order line (i.e. $\sigma < \sigma_c$ and $x \neq 0$).

### E.2.1 Mean-field-theory in the vicinity of $\sigma_c$

In the case of $\sigma \simeq \sigma_c$, we have $\partial_x t(x) = 0$ and we need to keep terms to second order in $(x - x_c)$:

$$\frac{\partial\langle\phi\rangle}{\partial\Phi} \simeq -\frac{\frac{A}{B}\frac{C+4J}{A+4J}}{(x-x_c)^2/2\sigma_c^2 + r}, \tag{E.23}$$

where $r \equiv (\sigma - \sigma_c)/\sigma_c$. From the definition of $x$, we obtain

$$\frac{dx}{d\Phi} = \frac{A}{C+4J} + \frac{B}{C+4J}\frac{d\langle\phi\rangle}{d\Phi}. \tag{E.24}$$

Expressing $\frac{d\langle\phi\rangle}{d\Phi}$ in terms of $\frac{dx}{d\Phi}$ we obtain an ordinary differential equation for $x(\Phi, \sigma)$, which reads:

$$\frac{dx}{d\Phi}\frac{C+4J}{B} - \frac{A}{B} = -\frac{\frac{A}{B}\frac{C+4J}{A+4J}}{(x-x_c)^2/2\sigma_c^2 + r}. \tag{E.25}$$

Integrating both sides, and keeping terms to third order in $x$, we obtain:

$$\Phi - \Phi_c = \frac{A+4J}{A} r x + \frac{1}{6\sigma_c^2} \frac{A+4J}{A} x^3. \tag{E.26}$$

Substituting $x = r^{1/2}\sigma_c y$, we arrive at

$$y^3 + 6y - \frac{3A(C+4J)}{\sqrt{2\pi}BJ} \frac{\Phi - \Phi_c}{r^{3/2}} = 0, \tag{E.27}$$

$$\langle\phi\rangle - \langle\phi\rangle_c = \left[\sigma r^{1/2}(C+4J) y \left(\frac{\Phi - \Phi_c}{r^{3/2}}\right) - A(\Phi - \Phi_c)\right] / B \sim r^{1/2} y \left(\frac{\Phi - \Phi_c}{r^{3/2}}\right), \tag{E.28}$$

which is the universal functional form of the dependence of the mean-field $\langle\phi\rangle$ (i.e. the analog of the magnetization in the random field Ising model) on the control phase $\Phi$ (i.e. the analog of the applied magnetic field). From this relation, we can obtain the susceptibility as well as corrections to the power law scaling of avalanche sizes away from the critical point.

### E.2.2 Mean-field-theory for $\sigma < \sigma_c$

In the case $\sigma < \sigma_c$, we cannot ignore $\partial_x t(x_c)$ term, which now dominates the scaling. In this regime, near criticality the susceptibility obeys:

$$\frac{\partial\langle\phi\rangle}{\partial\Phi} \simeq \frac{C+4J}{B} \frac{A\sigma^2}{x_c(A+4J)(x-x_c)} = \frac{C+4J}{B} \left(\frac{dx}{d\Phi} - \frac{A}{C+4J}\right), \tag{E.29}$$

where the last equality is copied from Eq. (E.24). Reshuffling, we obtain the ordinary differential equation:

$$\frac{dx}{d\Phi} = \frac{A\sigma^2}{x_c(A+4J)(x-x_c)} + \frac{A}{C+4J}. \tag{E.30}$$

Near criticality, the last term can clearly be dropped, and we find:

$$(x - x_c) = \sqrt{\frac{2A\sigma}{x_c(A+4J)}} (\Phi - \Phi_c)^{1/2}, \tag{E.31}$$

$$\langle\phi\rangle - \langle\phi\rangle_c \sim (\Phi - \Phi_c)^{1/2}. \tag{E.32}$$

### E.2.3 Mean-field equations for the critical line

Finally, we may ask how $\Phi_c(\sigma)$ behaves in the vicinity of $\sigma_c$. By using the condition for criticality $t(x_c) = 0$, we obtain the relation

$$x_c(\sigma) = \sigma\sqrt{-2\log(\sigma/\sigma_c)}. \tag{E.33}$$

By using the definition for $x$ and the mean-field-theory equation, Eq. (E.2), we obtain an equation for the line of SWAs, i.e. $\Phi_c(\sigma)$:

$$\langle\phi\rangle_c(\sigma) = \frac{1}{B}((x_c(\sigma)+\phi_c^0)(C+4J) - A\Phi_c(\sigma)) = \frac{1}{A+4J}\left(A\Phi_c(\sigma) + 2\pi J\left(1 + \mathrm{Erf}\left[\frac{x_c(\sigma)}{\sqrt{2}\sigma}\right]\right)\right). \tag{E.34}$$

This equation, supplemented by Eq. (E.33), can be solved numerically in a straightforward way. Alternatively, we can expand about critical value of disorder to obtain the equation for the first-order line of SWAs:

$$\Phi_c(\sigma) - \Phi_c(\sigma_c) = -\frac{8BJ\sqrt{\pi}}{3A(C+4J)}|r|^{3/2}; \tag{E.35}$$

see Fig. 3.7.

# Appendix F

# The renormalization group transformation of the long-range soft-spin RFIM

The goal of this appendix is to provide the details of the renormalization-group transformation of the long-range soft-spin RFIM effective action given in Eq. (3.71). The renormalization procedure follows the same steps as for the short-range soft-spin RFIM as described in [77], and is performed in two parts: first, the high momentum modes lying in the range $\Lambda/b < q < \Lambda$, where $\Lambda$ is the high-momentum cut-off and $b$ determines the coarse graining, are traced out; second, the lengths are rescaled by $b^{-1}$ to bring the effective action back to its original form but with rescaled coefficients.

We begin by explicitly writing the high momentum cut-off $\Lambda$ in the expression for the effective action Eq. (3.71):

$$S_{\text{eff}} = -\int dt \int_0^\Lambda \text{đ}q\, \hat{\eta}(-q,t) \left[-a\frac{\partial_t}{\Gamma_0} + |q| - w\right] \eta(q,t) \tag{F.1}$$

$$+ \frac{1}{2}\int dt_1\, dt_2 \int_0^\Lambda \text{đ}q\, u_{2,0}\hat{\eta}(-q,t_1)\hat{\eta}(q,t_2) \tag{F.2}$$

$$+ \frac{1}{6}\int dt \int_0^\Lambda \text{đ}q_1\, \text{đ}q_2\, \text{đ}q_3\; u\, \hat{\eta}(q_1,t)\eta(q_2,t)\eta(q_3,t)\eta(-q_1-q_2-q_3,t). \tag{F.3}$$

The cut-off $\Lambda$ starts out representing the discrete nature of the aperture array (or the spins of the RFIM). In the first step of the renormalization-group transformation we must trace over the fields with momenta in the shell $\Lambda/b < q < \Lambda$, where $b$ is some number close to, but bigger than, unity. It is convenient to introduce the notation where we add the subscript "s" (which stands for slow) to fields with $q < \Lambda/b$ and "f" (which stands for fast) to fields with $q > \Lambda/b$. The goal then becomes to compute the effective action which is obtained by tracing over the fast fields

$$\exp\left(-\beta S'_{\text{eff}}[\hat{\eta}_{\text{s}}, \eta_{\text{s}}]\right) = \int D[\hat{\eta}_{\text{f}}, \eta_{\text{f}}] \exp\left(-\beta S_{\text{eff}}[\hat{\eta}_{\text{s}}, \eta_{\text{s}}, \hat{\eta}_{\text{f}}, \eta_{\text{f}}]\right). \tag{F.4}$$

To perform the path integral over the non-quadratic parts of the action we expand the exponential in powers of $u_{2,0}$ and $u$ to one loop order. At this order there are no diagrams that correspond to the the rescaling of $u_{2,0}$. The Feynman diagrams describing the rescaling of $w$ and $u$ are pictured in Fig. 3.10. The corresponding amplitudes of these two diagrams are

$$A_1 = \frac{1}{2} u_{2,0} u I_1 \equiv \frac{1}{2} \int_{\Lambda/b}^{\Lambda} đq \frac{1}{(|q| - w)^2} u_{2,0} u \tag{F.5}$$

for the rescaling of $w$ (top diagram) and

$$A_2 = \frac{1}{2} u_{2,0} u^2 I_2 \equiv \frac{1}{2} \int_{\Lambda/b}^{\Lambda} đq \frac{1}{(|q| - w)^3} u_{2,0} u^2 \tag{F.6}$$

for the rescaling of $u$ (bottom diagram). Therefore, upon integrating over the fast fields we are left with the effective action

$$S_{\text{eff}} = - \int dt \int_0^{\Lambda/b} đq\, \hat{\eta}(-q,t) \left[ -a \frac{\partial_t}{\Gamma_0} + |q| - \left( w + \frac{1}{2} I_1 u_{2,0} u \right) \right] \eta(q,t) \tag{F.7}$$

$$+ \frac{1}{2} \int dt_1\, dt_2 \int_0^{\Lambda/b} đq\, u_{2,0} \hat{\eta}(-q,t_1) \hat{\eta}(q,t_2) \tag{F.8}$$

$$+ \frac{1}{6} \int dt \int_0^{\Lambda/b} đq_1\, đq_2\, đq_3\ (u + 3 I_2 u_{2,0} u^2)\, \hat{\eta}(q_1,t) \eta(q_2,t) \eta(q_3,t) \eta(-q_1-q_2-q_3,t). \tag{F.9}$$

Next we perform the second step of the renormalization-group transformation and rescale the length so as to bring the effective action Eq. (F.9) to the original form Eq. (F.3). After this transformation, we find that the coefficients $w$ and $u$ scale as

$$w' = b\big(w + \frac{u_{2,0} u}{2} I_1\big), \tag{F.10}$$

$$u' = b^{\epsilon}\big(1 + 3 u_{2,0} u I_2\big). \tag{F.11}$$

As $u$ always appears in combination with $u_{2,0}$, it is convenient to change variables from $u$ to $v \equiv u_{2,0} u$. The final step needed to obtain the renormalization-group flow equations is to evaluate the integrals $I_1$ and $I_2$. We concentrate on the case of $d \sim 3$, and evaluate the integrals in $d = 3 - \epsilon$ dimensions as follows:

$$I_1 \approx \frac{1}{2\pi^2} \int_{\Lambda/b}^{\Lambda} dq \left( 1 + 2\frac{w}{q} + \dots \right) = \frac{1}{2\pi^2} \left[ \Lambda \left( 1 - \frac{1}{b} \right) + 2w \log b \right] + O\left( \frac{1}{\Lambda} \right) \tag{F.12}$$

$$I_2 \approx \frac{1}{2\pi^2} \int_{\Lambda/b}^{\Lambda} \frac{dq}{q} \left( 1 + 3\frac{w}{q} + \dots \right) = \frac{1}{2\pi^2} \log(b) + O\left( \frac{1}{\Lambda} \right). \tag{F.13}$$

We thus arrive at the following set of flow equations:

$$v' = v + v\log(b)\left(\epsilon + \frac{3v}{2\pi^2}\right), \tag{F.14}$$

$$w' = b\left(w + \frac{v}{2}\frac{1}{2\pi^2}\left[\Lambda\left(1 - \frac{1}{b}\right) + 2w\log b\right]\right). \tag{F.15}$$

The flow equations, Eqs. (F.14) and (F.15), have two fixed points. The Gaussian fixed point is located at $v = 0$ and $u = 0$ and the Wilson-Fisher fixed point at $v = -\frac{2\pi^2}{3}\epsilon$ and $w = \frac{\epsilon\Lambda}{6}\frac{1}{1-\epsilon/3}$.

To facilitate further analysis, and in particular to compute critical exponents, we linearize the recursion relations in the vicinity of the fixed points. For the Gaussian fixed point we find

$$\begin{pmatrix} \frac{\partial w'}{\partial w} & \frac{\partial w'}{\partial v} \\ \frac{\partial v'}{\partial w} & \frac{\partial v'}{\partial v} \end{pmatrix} = \begin{pmatrix} b & \frac{\Lambda}{4\pi^2}(b-1) \\ 0 & b^{\epsilon} \end{pmatrix}, \tag{F.16}$$

where we have used $1 + \epsilon\log b = 1 + \log(1 + (b^{\epsilon} - 1)) \approx b^{\epsilon}$. Similarly for the Wilson-Fisher fixed point we find

$$\begin{pmatrix} \frac{\partial w'}{\partial w} & \frac{\partial w'}{\partial v} \\ \frac{\partial v'}{\partial w} & \frac{\partial v'}{\partial v} \end{pmatrix} = \begin{pmatrix} b^{1-\epsilon/3} & \frac{\Lambda}{4\pi^2}(b-1) \\ 0 & b^{-\epsilon} \end{pmatrix}. \tag{F.17}$$

For the Gaussian fixed point the eigenvalues of this linearized transformation are $e_w = b^{y_t} = b^1$ and $e_2 = b^{\epsilon}$, and the corresponding eigendirections are $(1, 0)$ and $(-\Lambda(2\pi)^{-2}, 1)$. The eigenvalue $e_w$ is always bigger than unity, and therefore corresponds to an eigendirection that is always unstable. On the other hand, $e_2$ is smaller than unity for $d > 3$ and larger for $d < 3$. Thus for $d > 3$, $e_2$ corresponds to a stable eigendirection, while for $d < 3$ an unstable one.

Similarly, for the Wilson-Fisher fixed point the eigenvalues are $e_w = b^{y_t} = b^{1-\epsilon/3}$ and $e_2 = b^{-\epsilon}$, and the eigendirections coincide with those found for the Gaussian fixed point. Again, the eigenvalue $e_w$ is always bigger than unity, and therefore corresponds to an eigendirection that is always unstable. For the case of the Wilson-Fisher fixed point, however, $e_2$ has the opposite behavior as compared to the Gaussian fixed point. For $d > 3$, $e_2$ is larger than unity and corresponds to an unstable eigendirection, while for $d < 3$ $e_2$ becomes smaller than unity and thus corresponds to a stable eigendirection.

# References

[1] V. L. Ginzburg and L. D. Landau, Zh. Eksp. Teor. Fiz. **20**, 1064 (1950).

[2] J. Bardeen, L. N. Cooper, and J. R. Schrieffer, Phys. Rev. **108**, 1175 (1957).

[3] Y. M. Ivanchenko and L. A. Zil'berman, JETP Lett. **8**, 113 (1968).

[4] Y. M. Ivanchenko and L. A. Zil'berman, JETP **28**, 1272 (1969).

[5] V. Ambegaokar and B. I. Halperin, Phys. Rev. Lett. **22**, 1364 (1969).

[6] J. S. Langer and V. Ambegaokar, Phys. Rev. **164**, 498 (1967).

[7] D. E. McCumber and B. I. Halperin, Phys. Rev. B **1**, 1054 (1970).

[8] W. Meissner and R. Ochsenfeld, Naturwissenschaften **21**, 787 (1933).

[9] F. London and H. London, Proc. R. Soc. London, Ser A **A149**, 71 (1935).

[10] L. P. Gorkov, Zh. Eksp. Teor. Fiz. **34**, 735 (1953), [Sov. Phys. JETP **7**, 505 (1958)].

[11] L. P. Gorkov, Zh. Eksp. Teor. Fiz. **36**, 1918 (1959), [Sov. Phys. JETP **9**, 1364 (1959)].

[12] E. Maxwell, Phys. Rev. **78**, 477 (1950).

[13] C. A. Reynolds, B. Serin, W. H. Wright, and L. B. Nesbitt, Phys. Rev. **78**, 487 (1950).

[14] H. Fröhlich, Phys. Rev. **79**, 845 (1950).

[15] W. H. Keesom and A. P. Keesom, Physica **2**, 557 (1935).

[16] W. H. Keesom and A. P. Keesom, Physica **3**, 359 (1936).

[17] J. F. Allen, R. Peierls, and M. Z. Uddin, Nature **140**, 62 (1937).

[18] P. Kapitza, Nature **141**, 74 (1938).

[19] J. F. Allen and A. D. Misener, Nature **141**, 75 (1938).

[20] J. F. Allen and H. Jones, Nature **141**, 243 (1938).

[21] D. Shoenberg, Nature **171**, 458 (1953).

[22] L. P. Pitaevskii, J. Low Temp. Phys. **87**, 127 (1992).

[23] L. D. Landau, J. Phys. U.S.S.R. **5**, 71 (1941).

[24] E. P. Gross, Nuovo Cimento **20**, 454 (1961).

[25] E. P. Gross, J. Math. Phys. **4**, 195 (1963).

[26] L. P. Pitaevskii, JETP **13**, 451 (1961).

[27] M. P. A. Fisher and W. Zwerger, Phys. Rev. B **32**, 6190 (1985).

[28] A. O. Caldeira and A. J. Leggett, Physica A **121**, 587 (1983).

[29] W. A. Little, Phys. Rev. **156**, 396 (1967).

[30] D. E. McCumber, Phys. Rev. **172**, 427 (1968).

[31] P. W. Anderson, Rev. Mod. Phys. **38**, 298 (1966).

[32] W. A. Little and R. D. Parks, Phys. Rev. Lett. **9**, 9 (1962).

[33] W. A. Little and R. D. Parks, Phys. Rev. **133**, a 97 (1964).

[34] M. Tinkham, *Introduction to Superconductivity*, 2nd ed. (McGraw-Hill, New York, 1996).

[35] K. K. Likharev, Rev. Mod. Phys. **51**, 101 (1979).

[36] A. Bezryadin and B. Pannetier, J. Low Temp. Phys. **98**, 251 (1995).

[37] C. C. Abilio, L. Amico, R. Fazio, and B. Pannetier, J. Low Temp. Phys. **118**, 23 (2000).

[38] D. S. Hopkins, D. Pekker, P. M. Goldbart, and A. Bezryadin, Science **308**, 1762 (2005).

[39] C. A. Brebbia, *Boundary Element Method for Engineers* (Pentech Press, London, 1978).

[40] K. K. Likharev, Sov. Radiophys. **14**, 722 (1973).

[41] J. R. Clem, Bull. Am. Phys. Soc. **43**, 411 (1972).

[42] G. M. Maksimova, Phys. Solid State **40**, 1610 (1998).

[43] G. Stan, S. B. Field, and J. M. Martinis, Physical Review Letters **92**, 097003 (2004).

[44] I. S. Gradstein and I. M. Ryzhik, *Table of Integrals, Series, and Products* (Academic Press, New York, 1965).

[45] Zinn-Justin, *Quantum Field Theory and Critical Phenomena*, 3rd ed. (Oxford University Press, New York, 2002).

[46] R. C. Jaklevic, J. Lambe, A. H. Silver, and J. E. Mercereau, Phys. Rev. Lett. **12**, 159 (1964).

[47] S. K. H. Lam and D. L. Tilbrook, Appl. Phys. Lett. **82**, 1078 (2003).

[48] J.-P. Cleuziou, W. Wernsdorfer, V. Bouchiat, T. Ondarcuhu, and M. Monthioux, Nature Nanotech. **1**, 53 (2006).

[49] I. Chiorescu, Y. Nakamura, C. J. P. M. Harmans, and J. E. Mooij, Science **299**, 1869 (2003).

[50] W. Wernsdorfer *et al.*, Phys. Rev. Lett. **79**, 4014 (1997).

[51] W. Wernsdorfer and R. Sessoli, Science **284**, 133 (1999).

[52] D. S. Hopkins, *Measurements of superconducting phase gradients by a nanowire quantum interference device templated by DNA molecules*, PhD thesis, University of Illinois at Urbana Champaign, 2007.

[53] J. Bardeen, Rev. Mod. Phys. **34**, 667 (1962).

[54] S. J. Turneaure, T. R. Lemberger, and J. M. Graybeal, Phys. Rev. Lett. **84**, 987 (2000).

[55] R. Prozorov *et al.*, Phys. Rev. B **67**, 184501 (2003).

[56] A. M. Campbell, J. Phys. C **2**, 1492 (1969).

[57] A. M. Campbell, J. Phys. C **4**, 3186 (1971).

[58] R. Labusch, Phys. Rev. **170**, 470 (1968).

[59] M. Tinkham and C. N. Lau, Applied Physics Letters **80**, 2946 (2002).

[60] B. J. Baelus, A. Kanda, F. M. Peeters, Y. Ootuka, and K. Kadowaki, Physical Review B (Condensed Matter and Materials Physics) **71**, 140502 (2005).

[61] K. Y. Arutyunov and T. T. Hongisto, Physical Review B (Condensed Matter and Materials Physics) **70**, 064514 (2004).

[62] A. A. Pesetski and T. R. Lemberger, Phys. Rev. B **62**, 11826 (2000).

[63] A. Lamacraft and B. D. Simons, Phys. Rev. Lett. **85**, 4783 (2000).

[64] M. Hermele, G. Refael, M. P. A. Fisher, and P. M. Goldbart, Nature Physics **1**, 117 (2005).

[65] Y. Sato, E. Hoskinson, and R. E. Packard, Physical Review B (Condensed Matter and Materials Physics) **74**, 144502 (2006).

[66] K. Sukhatme, Y. Mukharsky, T. Chui, and D. Pearson, Nature **411**, 280 (2001).

[67] E. Hoskinson, R. E. Packard, and T. M. Haard, Nature **433**, 376 (2005).

[68] E. Hoskinson, Y. Sato, I. Hahn, and R. E. Packard, Nature Physics **2**, 23 (2006).

[69] R. P. Feynman, *Progress in Low Temperature Physics* (North-Holland, Amsterdam, 1955), Vol. 1, Chap. 2.

[70] S. V. Iordanskii, Zh. Eksp. Teor. Fiz. **48**, 708 (1965), [*Sov. Phys. JETP* **21** 467-471 (1965)].

[71] W. Zimmermann, in *Proceedings of the Fifth Oregon Conference on Liquid Helium, a Report from the Department of Physics*, p. 118, University of Oregon, 1987.

[72] T. Chui, W. Holmes, and K. Penanen, Phys. Rev. Lett. **90**, 085301 (2003).

[73] R. Burridge and L. Knopoff, Bull. Seismol. Soc. Am. **57**, 341 (1967).

[74] J. P. Sethna *et al.*, Phys. Rev. Lett. **70**, 3347 (1993).

[75] D. S. Fisher, Phys. Reps. **301**, 113 (1998), see for a review.

[76] M. C. Marchetti, cond-mat/0503660 (2005), see also and references therein.

[77] K. Dahmen, *Hysteresis, Avalanches, and Disorder-Induced Critical Scaling: A Renormalization Group Approach*, PhD thesis, Cornell, 1995.

[78] J. C. Davis and R. E. Packard, Rev. Mod. Phys. **74**, 741 (2002).

[79] B. D. Josephson, Phys. Lett. **1**, 251 (1962).

[80] J. M. Rowell, Phys. Rev. Lett. **11**, 200 (1963).

[81] I. Giaever, Phys. Rev. Lett. **14**, 904 (1965).

[82] M. Albiez *et al.*, Physical Review Letters **95**, 010402 (2005).

[83] O. Avenel and E. Varoquaux, Phys. Rev. Lett. **60**, 416 (1988).

[84] S. Backhaus, S. V. Pereverzev, A. Loshak, J. C. Davis, and R. E. Packard, Science **278**, 1435 (1997).

[85] G. B. Hess, Phys. Rev. Lett. **27**, 977 (1971).

[86] O. Narayan and D. S. Fisher, Phys. Rev. Lett. **68**, 3615 (1992).

[87] O. Narayan and D. S. Fisher, Phys. Rev. B **46**, 11520 (1992).

[88] P. C. Martin, E. D. Siggia, and H. A. Rose, Phys. Rev. A **8**, 423 (1973).

[89] K. Dahmen and J. P. Sethna, Phys. Rev. Lett. **71**, 3222 (1993).

[90] K. Dahmen and J. P. Sethna, Phys. Rev. B **53**, 14872 (1996).

[91] H. Sompolinsky and A. Zippelius, Phys. Rev. B **25**, 6860 (1982).

[92] Y. Sato, Model of thermal fluctuations, private communication.

# Author's Biography

David Pekker was born in a typical Soviet scientific family and grew up in Novosibirsk, central Siberia, Russia. In 1991, his family immigrated to the U.S., first settling in St. Paul, Minnesota, and later moving to Austin, Texas. He received his B.S. in Physics and B.A. in Mathematics in 2002 from Rice University, in Houston, Texas. He entered the Ph.D. program in Physics at the University of Illinois at Urbana Champaign in 2002.

**List of publications at the University of Illinois at Urbana-Champaign**

1. D. Pekker, R. Barankov, and P. M. Goldbart "Critical properties of dissipative superflow of helium in multiply-connected geometries," in preparation (2007).
2. D. Pekker, R. Barankov, and P. M. Goldbart "Phase-slip avalanches in the superflow of $^4$He through arrays of nanosized apertures," *Physical Review Letters* , (2007).
3. A. Rogachev, T.-C. Wei, D. Pekker, A.T. Bollinger, P. M. Goldbart, and A. Bezryadin, "Magnetic field enhancement of superconductivity in ultra-narrow wires," *Physical Review Letters* **97**, 137001 (2006).
4. T.-C. Wei, D. Pekker, A. Rogachev, A. Bezryadin, P. M. Goldbart "Enhancing superconductivity: Magnetic impurities and their quenching by magnetic fields," *Europhysics Letters* **75**, 943 (2006).
5. D. Pekker, A. Bezryadin, D. S. Hopkins, and P. M. Goldbart, "Operation of a superconducting nanowire quantum interference device with mesoscopic leads," *Physical Review B* **72**, 104517 (2005).
6. D. Pekker, S. Mukhopadhyay, N. Trivedi, and P. M. Goldbart, "Double-exchange model for noninteracting electron spins coupled to a lattice of classical spins: Phase diagram at zero temperature," *Physical Review B* **72**, 075118 (2005).
7. D. S. Hopkins, D. Pekker, P. M. Goldbart, and A. Bezryadin, "Quantum Interference Device Made by DNA Templating of Superconducting Nanowires," *Science* **308** 1762 (2005).